Journal of Materials Chemistry A

ROYAL SOCIETY OF CHEMISTRY

REVIEW

View Article Online
View Journal | View Issue

Cite this: J. Mater. Chem. A, 2024, 12, 11771

Recent advances in noble metal-free electrocatalysts to achieve efficient alkaline water splitting

Mohammed-Ibrahim Jamesh, [ag] Dingqin Hu,[ag] Jing Wang, [b] Farah Naz,[ag] Jianpei Feng,[ag] Li Yu, [ag] Zhao Cai, [b] Juan Carlos Colmenares, [cf] Duu-Jong Lee,*[d] Paul K. Chu *[e] and Hsien-Yi Hsu *[ag]

Electrochemical water splitting is one of the promising approaches for generating hydrogen. Developing noble metal-free electrocatalysts for the hydrogen evolution reaction (HER) and oxygen evolution reaction (OER) is important to achieve efficient water-splitting. This paper reviews the activity, stability, and durability of recently reported noble metal-free electrocatalysts such as oxides/hydroxides/(oxy) hydroxides/layered double hydroxides, sulfides, selenides, phosphides/phosphates, nitrides, carbon-based electrocatalysts, and alloy/B/V/F/Si based electrocatalysts for the HER and OER in an alkaline environment, including the strategies used to achieve high activity and stability/durability at a current density of ≥1000 mA cm^{-2}. Moreover, this paper discusses the various promising strategies including the fabrication of nanostructured, ultrathin, porous, and nanoporous materials, preparing superaerophobic surfaces, construction of hollow structures, core–shell structures, heterostructures, heterojunctions, or Mott–Schottky heterojunctions, designing facile and/or scalable synthesis routes, creating doping and/or vacancies/defects, fabricating catalysts with high valence state sites, designing medium or high-entropy alloys, and tuning the atomic packing structure, electronic structure, or conductivity to enhance the activity and stability for the HER and/or OER.

Received 30th November 2023
Accepted 27th March 2024

DOI: 10.1039/d3ta07418h

rsc.li/materials-a

1. Introduction

Hydrogen is considered as a promising fuel having low carbon emission and high energy density (142 MJ kg^{-1}). The global hydrogen production market size was estimated at about 120 billion USD in the year 2020, whereas currently, about 95% of the industrial hydrogen production processes such as steam reforming, and coal gasification with extensive greenhouse gas release are not efficient processes, while only about 4% of the H_2 production around the world depends on water electrolysis, and the current research studies are being focused on water electrolysis or other strategies to alleviate the utilization of fossil fuels for the production of hydrogen energy.[1] Electrochemical water splitting is a promising way for sustainable hydrogen production, especially with renewable electricity such as solar or wind sources.[2] Electrochemical water splitting comprises a hydrogen evolution reaction (HER) at the cathode with the involvement of two electrons, and an oxygen evolution reaction (OER) at the anode with the involvement of four electrons in both acid and alkaline environments. Currently, noble electrocatalysts, such as Ir/Ru-based compounds for the OER and Pt for the HER, are considered as promising electrocatalysts for water splitting.[3] Nevertheless, their high cost and scarcity limit their uses. Moreover, the currently used OER electrocatalysts for water splitting in acid environments are scarce and expensive,[3,4] whereas the cost of the water electrolyzer system can be reduced by using noble metal-free electrocatalysts in the alkaline environment.[2b,d,5] To alleviate the gas mixing issues (H_2 and O_2), proton exchange membrane (PEM) water electrolysis and anion exchange membrane (AEM) water electrolysis are considered as promising water electrolyzers for industrial level application, where the AEM water electrolyzer can operate in an alkaline environment but the PEM water electrolyzer may require acid-stable OER

[a]School of Energy and Environment, Department of Materials Science and Engineering, Centre for Functional Photonics (CFP), City University of Hong Kong, Kowloon Tong, Hong Kong, China. E-mail: sam.hyhsu@cityu.edu.hk

[b]Faculty of Materials Science and Chemistry, China University of Geosciences (Wuhan), Wuhan 430074, China

[c]Institute of Physical Chemistry, Polish Academy of Sciences, Kasprzaka 44/52, 01224, Warsaw, Poland

[d]Department of Mechanical Engineering, City University of Hong Kong, Kowloon Tong, Hong Kong, China. E-mail: tuclee@cityu.edu.hk

[e]Department of Physics, Department of Materials Science and Engineering, Department of Biomedical Engineering, City University of Hong Kong, Tat Chee Avenue, Kowloon, Hong Kong, China. E-mail: paul.chu@cityu.edu.hk

[f]Engineering Research Institute (In3), Universidad Cooperativa de Colombia, Medellín 50031, Colombia

[g]Shenzhen Research Institute of City University of Hong Kong, Shenzhen 518057, P. R. China

electrocatalysts to operate in an acid environment, which can elevate the cost.[6] Therefore, various promising strategies such as improving the gas-evolution behavior, enhancing the conductivity, tuning the electronic structure, increasing the electrochemical surface area, surface reconstruction during the HER/OER, preparing core–shell/hetero/hollow structured materials, preparing amorphous materials, fabricating bimetallic/multi-metallic materials, doping metals/heteroatoms, preparing porous/nanostructured/quantum sized materials, and creating oxygen vacancies/defects are used to achieve high-performance noble metal-free electrocatalysts for the HER and/or OER in an alkaline environment.[5,7]

Developing noble-metal-free electrocatalysts with substantially lower overpotential (η) for HER and OER or significantly lower cell voltage for overall water splitting is highly desirable. Fabrication of transition metal boride electrocatalysts with a 3D hollow structure may alter the electronic structure, provide optimal adsorption energy with intermediates, improve the conductivity, expose abundant active sites, provide high mechanical strength, and facilitate gas evolution, all of which could improve the activity and stability of the HER and OER. For the HER in 1 M KOH, NiMoB hollow foam[8] affords an η of -18 mV at -10 mA cm^{-2}, suggesting its outstanding activity. For overall water splitting in 1 M KOH, NiMoB hollow foam//NiMoB hollow foam affords a potential of 1.431 V at 10 mA cm^{-2}, suggesting its good activity. Fabrication of composites containing transition metal selenides and perovskite oxides could enhance the performance of the OER. For the OER in 1 M KOH, LSCO-$MoSe_2$ (ref. 9) affords an η of 39 mV at 10 mA cm^{-2}, suggesting its very high activity, where LSCO is $La_{0.5}Sr_{0.5}CoO_{3-\delta}$ perovskite oxide. Moreover, $Mn_1Ni_1Co_1$-P//$Mn_1Ni_1Co_1$-P,[10] c-NiFe/a-NiFeOOH@NiMo//c-NiFe/a-NiFeOOH@NiMo,[11] and Gr-CNTs-Sn_4P_3//Gr-CNTs-Sn_4P_3 (ref. [12]) exhibit very high activity for overall water splitting in 1 M KOH, while the NiP_2-FeP_2@Cu nanoarray[13] exhibits very high activity for the HER. Thus, several noble metal-free electrocatalysts exhibit substantially much lower η for the HER and OER or significantly much lower cell voltage for overall water splitting.

An electrocatalyst for the HER or OER fabricated at a relatively low cost should operate at low η to deliver a current density for a prolonged period, which is highly desirable for industrial applications. Fabrication of tin-doped nickel sulfide having an ultrathin nanostructure could modify the electronic structure, and facilitate the evolution of gas even at large current densities, and that could boost the performance of the HER and OER. For the OER in 1 M KOH, the Sn-Ni_3S_2 (ref. [14]) affords an η of 267 mV at 100 mA cm^{-2}, and an η of 580 mV at a current density of 1000 mA cm^{-2}, indicating its significantly high activity, while it undergoes negligible decay at a very large current density of 2000 mA cm^{-2} after 10 000 cycles of CV, suggesting its substantially good durability. For the HER in 1 M KOH, it affords an η of -171 mV at -100 mA cm^{-2}, and an η of -570 mV at a current density of -1000 mA cm^{-2}, suggesting its significantly very high activity, while it undergoes negligible decay at a current density of -1000 mA cm^{-2} after 10 000 cycles of CV, suggesting its significantly very high durability. For overall water splitting in 1 M KOH, the Sn-Ni_3S_2//Sn-Ni_3S_2 affords a potential of 1.46 V at 10 mA cm^{-2}, and $\sim$2.65 V at a current density of 1000 mA cm^{-2}, suggesting its significantly very high activity. Integrating N-doped carbon with nanostructured transition metal/metal oxide could redistribute the electrons at the heterojunction interface, afford optimal adsorption energy with intermediates, enhance the conductivity, facilitate the evolution of gas, expose abundant active sites, and that could enhance the performance for the HER and OER. For the OER in 1 M KOH, Ni/MoO_2@CN[15] affords an η of 250 mV at 10 mA cm^{-2}, and an η of 420 mV at a large current density of 1000 mA cm^{-2}, suggesting its significantly very high activity, while it undergoes negligible decay at a large current density of 1000 mA cm^{-2} for 200 h, suggesting its significantly very high stability. For the HER in 1 M KOH, it affords an η of -33 mV at -10 mA cm^{-2}, and an η of -267 mV at a large current density of -1000 mA cm^{-2}, suggesting its significantly very high activity, while it undergoes negligible decay at a large current density of -1000 mA cm^{-2} for 200 h, suggesting its significantly very high stability. For overall water splitting in 1 M KOH, Ni/MoO_2@CN//Ni/MoO_2@CN affords a potential of 1.83 V at 200 mA cm^{-2}, and a potential of 2.02 V at a large current density of 1000 mA cm^{-2}, suggesting its significantly very high activity, while it affords 98.19% retention at 1.7 V for 168 h, suggesting its significantly very high stability. Moreover, C-$Ni_{1-x}O$/3D printed Ni,[16] Fe-Co-CO_3-OH,[17] FeP/Ni_2P,[18] Ni_2P-Fe_2P,[19] and $Co_2N_{0.67}$/$CoMoO_4$ (ref. [20]) for the HER and OER exhibit high activity and stability in 1 M KOH, while MoS_2/Mo_2C[21] for the HER, and CuS-Ni_3S_2/CuNi[22] for the OER exhibit high activity and stability. Thus, several noble metal-free electrocatalysts exhibit low η at high current densities with high stability for the HER and OER.

Besides, the fabrication of noble metal-free electrocatalysts by green-chemistry approaches is highly desirable to achieve efficient, green water electrolysis, and that could alleviate or diminish the use or production of hazardous substances.[23] Designing energy-efficient synthesis routes (especially at room temperature) for the fabrication of noble metal-free electrocatalysts is one of the promising green-chemistry approaches.[23] Chen *et al.*[24] observed that S-FeOOH exhibits enhanced activity and stability for the OER, while it was obtained by immersing cleaned Fe foam for 20 min at room temperature in the solution containing $Fe(NO_3)_3$ and $Na_2S_2O_3$. The redox reactivities of the lattice oxygen and Fe in FeOOH are activated due to S doping. Moreover, Zhao *et al.*[25] observed that NiFe LDH exhibits enhanced activity and stability for the OER, while it was prepared by immersing cleaned, acid-treated Fe foam in $NiSO_4$ solution under ambient conditions. In addition, Liu *et al.*[26] observed that IronCE10s exhibit enhanced activity and stability for the OER, while it was prepared on the cheap iron substrate by applying pulsed potentials for 10 s in

$NiSO_4$ electrolyte at 25 ± 1 °C, where the substrate was used as a counter electrode. The utilization of waste as a source for the fabrication of noble metal-free electrocatalysts is one of the promising green chemistry approaches.[23] Lu *et al.*[27] observed that WO_3@$F_{0.1}$-C exhibits enhanced activity and stability for the OER, while it was obtained by a plasma-induced assembly method, where perfluorooctanoic acid (a pollutant) is used as an F source. Utilization of renewable raw materials for the fabrication of noble-metal-free electrocatalysts is one of the most promising green-chemistry approaches.[23] Huang *et al.*[28] observed that Zn-Fe/Mn@Mn-FeP exhibits enhanced activity and stability for the HER and OER, where the nanostructured phosphide-based electrocatalyst is prepared using relatively low-cost metals such as Fe, Mn, and Zn. Thus, some green chemistry approaches including ambient temperature synthesis, utilization of waste as a source, and using relatively low-cost metals have been used for the fabrication of noble metal-free electrocatalysts for electrochemical water splitting.

Thus, recently, several promising strategies have been used for the fabrication of noble metal-free electrocatalysts to achieve low η at high current densities with high stability for the HER and OER and to achieve substantially much lower η for the HER and OER, while some green chemistry approaches have been applied for the fabrication of noble metal-free electrocatalysts for electrochemical water splitting. However, reviews on the fabrication of various noble metal-free electrocatalysts using several promising strategies along with their catalytic performances for electrochemical water splitting (HER and OER) in alkaline environments have been rarely reported. In this respect, the present paper reviews the activity, stability, and durability of several kinds of recently reported noble metal-free electrocatalysts such as oxides/hydroxides/(oxy)hydroxides/layered double hydroxides, sulfides, selenides, phosphides/phosphates, nitrides, carbon-based electrocatalysts, and alloy/B/V/F/Si based electrocatalysts for the HER and OER in an alkaline environment. In addition, this paper reviews the strategies used to achieve high activity and stability/durability at a current density of ≥1000 mA cm^{-2} of noble metal-free electrocatalysts for the HER and OER in an alkaline environment. Moreover, this paper reviews some green chemistry approaches used for the fabrication of noble metal-free electrocatalysts for electrochemical water splitting. Finally, this review summarizes several promising strategies used for the fabrication of noble metal-free electrocatalysts to achieve enhanced performance for the HER and OER in alkaline environments.

2. Constructing noble metal-free electrocatalysts for the HER and OER in an alkaline electrolyte

2.1. Constructing oxide/hydroxide/(oxy)hydroxide/layered double hydroxide electrocatalysts

2.1.1. Constructing oxide electrocatalysts. Fabrication of nanostructured transition metal oxides could expose abundant active sites, facilitate the evolution of gas, and that could enhance the performance of the HER and OER. Chen *et al.*[29] observed that Co_3O_4 exhibits enhanced activity and stability for the HER and OER. It was prepared on Co foam by sulfuration at 350 °C for 30 min followed by *in situ* electrochemical oxidation for 2 h. It is composed of a cubic Co_3O_4 phase. It possesses microspheres, which are composed of nanosheets. For overall water splitting in 1 M KOH, Co_3O_4//Co_3O_4 affords a potential of 1.483 V at 10 mA cm^{-2}, suggesting its very high activity.

Fabrication of nanostructured transition metal oxide/metal heterojunctions could expose abundant active sites, facilitate the evolution of gas, afford optimal adsorption energy with intermediates, and that could enhance the performance of HER and OER. Guo *et al.*[30] observed that MoO_2/Co exhibits enhanced activity for the HER and OER. It was synthesized on Ni foam by hydrothermal treatment followed by annealing under a H_2/Ar atmosphere. MoO_2/Co exhibits higher activity and lower charge transfer resistance for the HER than the CoMo precursor. It is crystalline containing MoO_2, α-Co, and β-Co phases having heterojunction. It contains Mo, Co, and O, which are homogeneously distributed. It possesses an ultrathin porous nanosheet structure. The density functional theory (DFT) calculations reveal that the Gibbs free energy of hydrogen adsorption (ΔG_{H^*}) of MoO_2/Co (−0.38 eV) is much nearer to the thermoneutral value than pure Co (−1.46 eV), suggesting the optimal hydrogen adsorption/desorption on the MoO_2/Co heterojunction, and that could enhance the activity for the HER. The HER in 1 M KOH affords an η of −48 mV at −10 mA cm^{-2}, suggesting its very high activity. Fabricating nanostructured transition metal doped metal oxides with oxygen vacancies could provide optimal adsorption energy with intermediates, and that could boost the performance of the HER and OER. Xue *et al.*[31] observed that Mn_6-CoO exhibits enhanced activity and stability for the HER and OER. It was obtained on Ni foam by hydrothermal treatment followed by annealing at 350 °C for 2 h under an Ar atmosphere. Mn_6-CoO exhibits higher activity for the HER and OER than CoO, while it exhibits higher electrochemical surface area and lower charge transfer resistance than CoO. Mn_6-CoO is composed of Mn-doped CoO. It possesses a heterophase (amorphous–crystalline). It contains oxygen vacancies (38.2%). It possesses a rambutan-like morphology, which contains numerous small nanoneedles. The DFT calculations reveal that the oxygen vacancies in Mn-CoO can optimize the adsorption-free energy of H* and HOO* intermediates, suggesting enhanced performance for the HER and OER. The HER in 1 M KOH affords an η of −25.6 mV at −10 mA cm^{-2}, suggesting its significantly very high activity. For overall water splitting in 1 M KOH, Mn_6-CoO//Mn_6-CoO affords a potential of 1.52 V at 10 mA cm^{-2}, suggesting its very high activity.

Rani *et al.*[32] studied the fabrication of faceted transition bimetallic oxide ($CuMn_2O_4$) nanoparticles with oxygen vacancies which can enhance the performance, activity, and stability of the HER. It was prepared by the polyol-mediated annealing method (hydrothermal treatment followed by annealing at 600 °C). The reported activity of faceted $CuMn_2O_4$ is higher than that of non-faceted $CuMn_2O_4$ for the HER. The prepared sample showed a cubic spinel $CuMn_2O_4$ phase, and Mn, Cu, and O are homogeneously distributed. It also has oxygen vacancies. HER

active phases can be produced by tuning the calcination parameters such as temperature, gas atmosphere, and time. Wu *et al.*[33] observed that Bi_2O_3-based catalyst exhibits enhanced activity and stability for the HER. It was prepared on Ni foam by hydrothermal treatment followed by heat treatment at 400 °C for 2 h in air followed by heat treatment at 400 °C in an Ar/H_2 atmosphere. It is crystalline containing α-Bi_2O_3, Bi_3Ni, and BiNi alloys, which are homogeneously distributed. It possesses nanosheet morphology. Thus, applying an *in situ* phase engineering strategy for Bi_2O_3 on Ni foam could produce HER active sites (Bi_xNi alloys and oxide phases), and that could enhance the performance of the HER.

Dynamically restructuring Ni_xCr_yO during electrolysis enhanced the porosity for better activity of the OER. Malek *et al.*[34] fabricated Ni_xCr_yO through hydrothermal treatment followed by calcination. The *in situ* and electrochemical investigations disclose that the electrochemically active surface area of Ni_xCr_yO could be increased by the leaching and redistribution of Cr upon electrolysis for a certain time interval, leading to an increase in porosity, and that could enhance the activity for the OER. The OER in 1 M KOH affords an η of 270 mV at 100 mA cm^{-2}, and an η of 320 mV at a high current density of 500 mA cm^{-2}, suggesting its very high activity, while it affords high stability. Fabrication of ultrathin transition bimetallic oxides with abundant oxygen vacancies can afford optimal adsorption energy with intermediates to increase the conductivity, which could also improve the performance of the OER. Yu *et al.*[35] prepared f-$Ni_{0.1}Co_{0.9}O_x$ by the electron beam evaporation method followed by calcination at 160 °C for 30 min using an O_2 atmosphere under UV light irradiation. f-$Ni_{0.1}Co_{0.9}O_x$ exhibits higher activity, higher electrochemical surface area, and lower charge transfer resistance for the OER than f-CoO_x and f-NiO_x. The alloy oxide film (f-$Ni_{0.1}Co_{0.9}O_x$) is optically transparent with a thickness of about 10 nm (ultrathin). It contains Co, Ni, and O, which are homogeneously distributed. It contains oxygen vacancies. Fabrication of a transition metal oxide/metal oxide hetero interface with abundant high valence ions can provide optimal adsorption energy with intermediates, increase the conductivity, and that could enhance the performance of the OER. Zhang *et al.*[36] observed that $Co_{3-x}O_4$/NiO exhibits enhanced activity and stability for the OER. It was prepared by hydrothermal treatment of the prepared $Co_{3-x}O_4$ with nickel acetate followed by calcination in the air atmosphere. $Co_{3-x}O_4$/NiO exhibits higher activity, higher electrochemical surface area, and lower charge transfer resistance for the OER than $Co_{3-x}O_4$ and Co_3O_4. It is crystalline containing $Co_{3-x}O_4$ and NiO. It contains a heterointerface. It contains Co, Ni, and O, which are homogeneously distributed. It contains Ni^{3+}, Ni^{2+}, Co^{3+}, and Co^{2+}. It possesses particle morphology (diameter: about 20 nm). Fabrication of a thin layer of a transition metal oxide on ZnO can modulate the electronic structure, and that could enhance the performance of the OER. Nandanapalli *et al.*[37] observed that Co_3O_4 SS Mesh/ZnO exhibits enhanced activity and stability for the OER (SS Mesh: stainless steel mesh). It was obtained by atomic layer deposition followed by chemical bath deposition followed by annealing followed by electrochemical deposition. Co_3O_4 SS Mesh/ZnO exhibits higher activity for the OER than SS Mesh/ZnO. It is composed of ZnO nanorods on stainless steel mesh, which are covered by a thin layer of cobalt oxide containing a predominant amount of Co_3O_4 along with a minor amount of CoO. It is crystalline. It contains Zn, Co, and O, which are homogeneously distributed. It contains Co^{3+} and Co^{2+}.

Fabrication of nickel–molybdenum oxysulfide with unique morphology as a pre-catalyst is essential, where the electrochemical reduction of the pre-catalyst can produce a highly active robust catalyst containing metallic species for the HER, while the electrochemical oxidation of the pre-catalyst can form a highly active robust catalyst containing high valence species for the OER. Liu *et al.*[38] observed that the HR-NiMoO@Ni exhibits substantially very high activity and stability for the HER, while the OR-NiOOH exhibits significantly very high activity and stability for the OER. The NiMoOS pre-catalyst on Ni foam was synthesized by hydrothermal treatment followed by sulfurization at 350 °C for 2 h. HR-NiMoO@Ni was obtained by applying cathodic CV scans on NiMoOS, whereas OR-NiOOH was obtained by applying anodic CV scans on NiMoOS (CV: cyclic voltammetry). HR-NiMoO@Ni and OR-NiOOH exhibit higher electrochemical surface area and lower charge transfer resistance than NiMoOS. The NiMoOS pre-catalyst is crystalline and is composed of sulfur-doped nickel molybdate ($NiMoO_4$). It contains Mo, Ni, O, and S, which are homogeneously distributed. It possesses nanorod array morphology. HR-NiMoO@Ni is composed of ultrathin cubic Ni metal nanosheets, which are vertically grown on NiMoO nanorods, forming a core–shell structure (core: NiMoO; shell: Ni). It contains abundant defects. OR-NiOOH is composed of quasi-crystalline NiOOH along with a residual amount of S. The atomic ratio of O : Ni : S is 3.9 : 1.7 : 0.1, respectively, suggesting the existence of a trace amount of S. It contains Ni^{3+}. It contains abundant defects. It possesses nanorod array morphology. For the OER in 1 M KOH, it affords an η of 213 mV at 10 mA cm^{-2}, and an η of 358 mV at a current density of 1000 mA cm^{-2}, suggesting its significantly very high activity, while it affords reasonable stability at 1000 A m^{-2} for 100 h, suggesting its significantly very high stability. For the HER in 1 M KOH, HR-NiMoO@Ni affords an η of −96 mV at −10 mA cm^{-2}, and an η of −308 mV at a current density of −1000 mA cm^{-2}, suggesting its substantially very high activity, while it affords reasonable stability at −1000 A m^{-2} for 100 h, suggesting its significantly very high stability. For overall water splitting in 1 M KOH, OR-$NiOOH^{OER}$//HR-$NiMoO@Ni^{HER}$ affords a potential of 1.51 V at 10 mA cm^{-2}, suggesting its very high activity, while it affords reasonable stability at 1000 A m^{-2} for 500 h, suggesting its significantly very high stability.

Designing a facile synthesis route for the fabrication of heterostructured transition metal oxides is essential, which

could modify the electronic structure, provide optimal adsorption energy with intermediates, and that could enhance the performance of the HER and OER. Hu *et al.*[1g] observed that the MH-TMO (mesoporous and heterostructured transition metal oxides) exhibits enhanced activity and stability for the HER and OER than Fe_2O_3, and CuO. It was synthesized on Ni foam by one-step hydrothermal treatment. It is crystalline, containing Fe_2O_3, and CuO. It exhibits a heterostructure. The Fe 2p peak of MH-TMO exhibits a slight negative shift in the high-resolution XPS spectra which confirms the modified electronic structure. It contains oxygen vacancies and mesopores. It exhibits a slightly compressed M–O–M bond, suggesting the electronic interaction between Fe_2O_3 and CuO. It possesses a sandwich structure, where the Fe_2O_3 nanosheets are surrounded on either side by CuO polyhedra. The DFT calculations disclose that the Fe site on the MH-TMO heterostructure affords optimal adsorption energy with intermediates. For the OER in 1 M KOH, it affords an η of ~216 mV at 10 mA cm^{-2}, suggesting its very high activity, while it undergoes negligible decay at 10 mA cm^{-2} for 100 h, suggesting its very high stability. For the HER in 1 M KOH, it affords an η of ~−70 mV at −10 mA cm^{-2}, suggesting its very high activity, while it affords reasonable stability at −10 mA cm^{-2} for 100 h. For overall water splitting in 1 M KOH, MH-TMO//MH-TMO affords a potential of 1.49 V at 10 mA cm^{-2}, suggesting its very high activity, while it undergoes negligible decay at 10 mA cm^{-2} for 100 h, suggesting its very high stability.

Fabrication of ultrafine transition metal oxide particles/nanostructured transition metal hydroxide heterostructures could modify the electronic structure, afford optimal adsorption energy with intermediates, and that could enhance the performance of the HER. Peng *et al.*[39] observed that MoO_3-$Co(OH)_2$@Ag exhibits enhanced activity and stability for the HER. It was prepared on Ag nanowire cloth by a two-step electrodeposition approach. MoO_3-$Co(OH)_2$@Ag exhibits higher activity, higher electrochemical surface area, and lower charge transfer resistance for the HER than MoO_3@Ag and $Co(OH)_2$@Ag. It is composed of a $Co(OH)_2$ nanosheet array on Ag nanowires, which is decorated by ultrafine MoO_3 particles. It is crystalline. It exhibits a heterostructure. In the high-resolution XPS spectra, the Mo 3d peak of MoO_3-$Co(OH)_2$@Ag exhibits a slight negative shift, when compared to that of MoO_3@Ag, suggesting a modified electronic structure due to the electronic interaction between MoO_3 and $Co(OH)_2$. It contains oxygen vacancies. The DFT calculations reveal that the Gibbs free-energy of the adsorbed H* (ΔG_{H*}) value on MoO_3-$Co(OH)_2$ (0.22 eV) is nearer to 0 eV when compared to that of MoO_3 (0.71), and $Co(OH)_2$ (1.99), suggesting optimal hydrogen adsorption/desorption on the MoO_3-$Co(OH)_2$ heterojunction.

Doping of phosphorus in cobalt molybdate could alter the electronic structure, provide optimal adsorption energy with intermediates, and that could enhance the performance of the HER and OER. Wang *et al.*[40] observed that P-$CoMoO_4$ exhibits enhanced activity and stability for the HER and OER. It was synthesized on Ni foam by hydrothermal treatment followed by phosphorization at 400 °C for 2 h under an Ar atmosphere. P-$CoMoO_4$ exhibits higher activity, higher electrochemical surface area, and lower charge transfer resistance for the HER and OER than $CoMoO_4$. It is composed of phosphorus-doped monoclinic β-$CoMoO_4$. It has low crystallinity. It contains Co, Mo, O, and P, which are homogeneously distributed. In the high-resolution XPS spectra, the Co 2p peak of P-$CoMoO_4$ exhibits a slight positive shift, when compared to that of $CoMoO_4$, suggesting a modified electronic structure due to the phosphorus doping. It contains $Mo^{\delta+}$ ($2 < \delta < 4$), Mo^{4+}, Mo^{5+}, and Mo^{6+}, whereas $CoMoO_4$ without P doping contains only Mo^{6+}. It contains PO_4^{3-}. It contains oxygen vacancies. It possesses micro-rod array morphology. It undergoes surface reconstruction during the HER and OER. It is reconstructed into $Co(OH)_2$-$CoMoO_4$/P-$CoMoO_4$ during the HER, while it is converted into CoOOH/P-$CoMoO_4$ during the OER. For the HER in 1 M KOH, it affords an η of −44 mV at −10 mA cm^{-2}, suggesting its very high activity, while it undergoes negligible decay at −50 mA cm^{-2} for 100 h, suggesting its very high stability. For overall water splitting in 1 M KOH, P-$CoMoO_4$//P-$CoMoO_4$ affords a potential of 1.54 V at 10 mA cm^{-2}, suggesting its very high activity.

Fabricating an electrocatalyst on a 3D periodic porous electrode could facilitate the evolution of gas bubbles, reduce bubble coalescence, expose abundant active sites, and that could enhance the activity for the HER and OER even at high current densities. Kou *et al.*[16] reported that the C-$Ni_{1-x}O$/3D printed Ni exhibits very high activity and stability for the HER and OER in 1 M KOH. It was prepared by 3D printing with solvent evaporation followed by heat treatment followed by coating of the catalyst (Fig. 1): at first, a Ni lattice structure was obtained through a direct ink writing technique, where the paste-like ink was composed of Ni particles, polylactic-*co*-glycolic acid (PLGA), dichloromethane (DCM), and ethylene glycol butyl ether (EGBE). Then, the printed parts were subjected to drying in air followed by thermal treatment (300 °C for 1 h and then 600 °C for 1 h in an H_2 atmosphere) followed by heat treatment (900 °C in an Ar atmosphere for 3 h). Later, nickel oxalate was grown on 3D printed Ni (working electrode) by applying 50 V for 10 minutes in 0.3 M oxalic acid as the electrolyte, where Ni foil was used as a counter electrode. Finally, C-$Ni_{1-x}O$/3D printed Ni was obtained by heating the nickel oxalate/3D printed Ni at 400 °C for 40 minutes in the Ar atmosphere. C-$Ni_{1-x}O$/3D printed Ni exhibits higher activity and electrochemical surface area for the HER and OER than C-$Ni_{1-x}O$/Ni foam. C-$Ni_{1-x}O$ on 3D printed Ni with a periodic porous structure exhibits much higher bubble flow and much less bubble coalescence than C-$Ni_{1-x}O$ on 3D Ni foam with a disordered porous structure. It is composed of 3D printed Ni having periodic pore structures, which is decorated by carbon doped nickel oxide, where the 3D porous structure could facilitate the evolution of gas bubbles, diminish bubble coalescence, and expose abundant active sites, which could enhance the activity for the HER and OER even at large current densities. The C-$Ni_{1-x}O$/3D printed Ni affords an η of −245 mV at a current

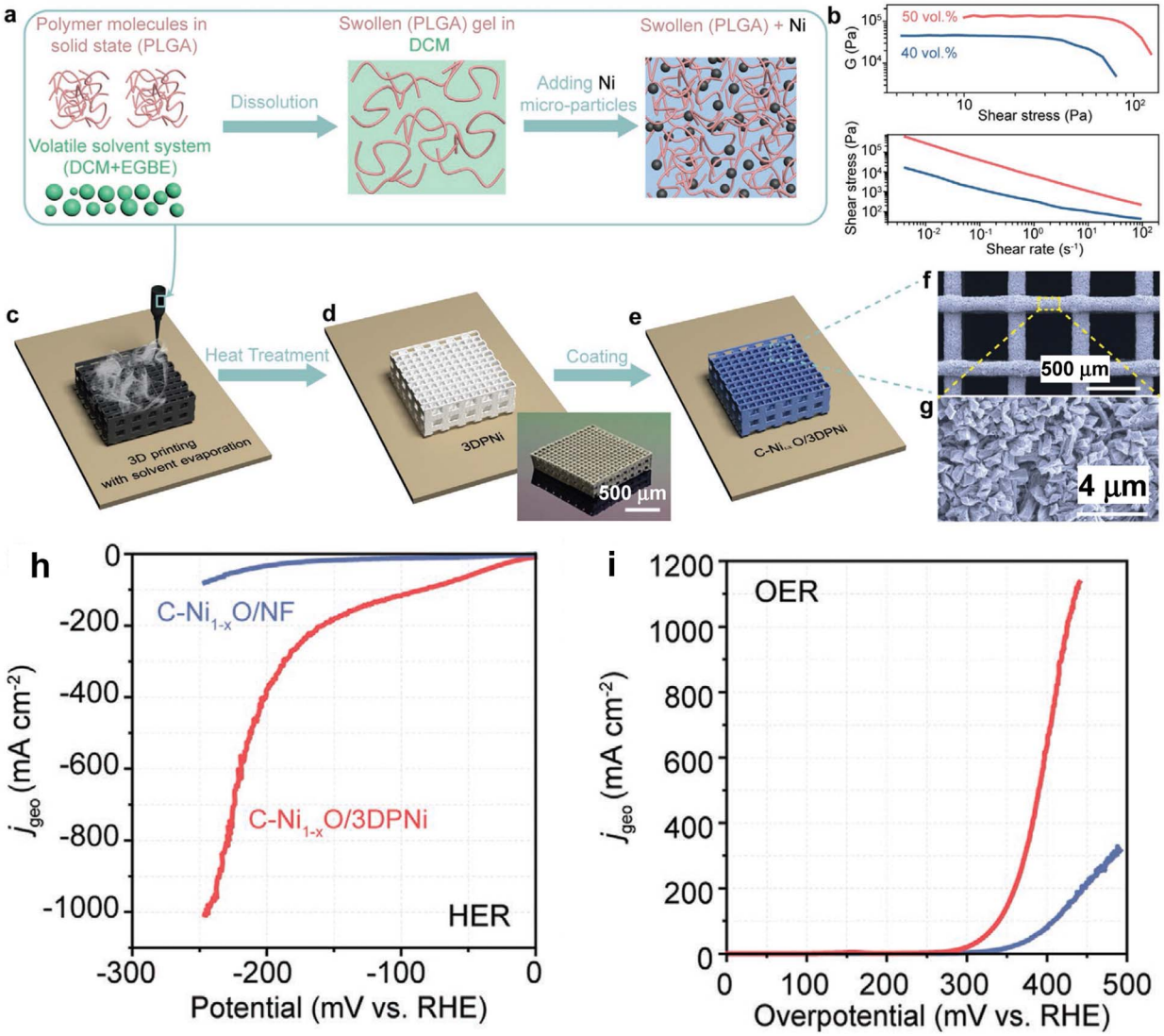

Fig. 1 (a) Schematic diagram depicting the ink formulation process; the graph located in the upper part of (b) represents the elastic modulus *versus* shear stress, and the graph located in the lower part of (b) indicates the shear stress *versus* shear rate for Ni-based inks with solid loadings of 50 vol% (red color) and 40 vol% (blue color); (c)–(e) schematic pictures depicting the fabrication process of C-$Ni_{1-x}O$/3D printed Ni, where the inset in (d) shows its corresponding digital photographic image; (f) and (g) SEM images of C-$Ni_{1-x}O$/3D printed Ni; LSV curves of C-$Ni_{1-x}O$/3D printed Ni in comparison with C-$Ni_{1-x}O$/Ni foam for (h) the HER and (i) OER in 1 M KOH (reproduced with permission from ref. 16 Copyright 2020, Wiley-VCH GmbH).

density of -1000 mA cm^{-2} for the HER (Fig. 1h), while it affords an η of 425 mV at a current density of 1000 mA cm^{-2} for the OER (Fig. 1i) in 1 M KOH, showing significantly high activity.

Integrating N-doped carbon with nanostructured transition metal/metal oxide could redistribute intermediates, enhance the conductivity, facilitate the evolution of gas, and expose abundant active sites, and that could enhance the performance of the HER and OER. Qian *et al.*[15] observed that Ni/MoO_2@CN exhibits significantly very high activity and stability for the HER and OER. It was prepared on Ni foam by hydrothermal treatment followed by carbonization at 450 °C for 2 h under a H_2/Ar atmosphere. Ni/MoO_2@CN exhibits higher activity for the HER than MoO_2@CN, while it exhibits higher activity for the OER than Ni/MoO_2. It is composed of Ni/MoO_2, which is encapsulated by N-doped carbon. It exhibits a three-phase heterojunction. It contains Ni, Mo, C, N, and O, which are homogeneously distributed. In the high-resolution XPS spectra, the Ni 2p peak of Ni/MoO_2@CN exhibits a slight positive shift, and the Mo 3d peak of Ni/MoO_2@CN exhibits a slight negative shift, when compared to that of Ni/MoO_2, suggesting a modified electronic structure due to the N doped carbon. It possesses nano-needle morphology. DFT calculations disclose the redistribution of electrons at the triple-phase heterojunction interface, which could provide optimal adsorption energy with

intermediates, and could enhance the performance of the HER and OER. For the OER in 1 M KOH, it affords an η of 250 mV at 10 mA cm^{-2}, and an η of 420 mV at a current density of 1000 mA cm^{-2}, suggesting its significantly very high activity, while it undergoes negligible decay at a current density of 1000 mA cm^{-2} for 200 h, suggesting its significantly very high stability. For the HER in 1 M KOH, it affords an η of −33 mV at −10 mA cm^{-2}, and an η of −267 mV at a current density of −1000 mA cm^{-2}, suggesting its significantly very high activity, while it undergoes negligible decay at a current density of −1000 mA cm^{-2} for 200 h, suggesting its significantly very high stability. For overall water splitting in 1 M KOH, Ni/MoO_2@CN//Ni/MoO_2@CN affords a potential of 1.83 V at 200 mA cm^{-2}, and a potential of 2.02 V at a current density of 1000 mA cm^{-2}, suggesting its significantly very high activity, while it affords 98.19% retention at 1.7 V for 168 h, suggesting its significantly very high stability.

The utilization of waste as a source for the green synthesis of electrocatalysts is highly desirable, whereas perfluorooctanoic acid, an aqueous pollutant, can be used as a fluorine source. Lu *et al.*[27] observed that WO_3@$F_{0.1}$-C exhibits enhanced activity and stability for the OER. It was obtained by the plasma-induced assembly method, where perfluorooctanoic acid (a pollutant) is used as an F source. WO_3@$F_{0.1}$-C exhibits higher activity, higher electrochemical surface area, and lower charge transfer resistance for the OER than WO_3@C. It is composed of ultra-small WO_3 nanoparticles (monoclinic crystals), which are decorated on F-doped graphite sheets. It exhibits an I_D/I_G ratio of 0.924, suggesting the existence of high defects and low graphitization degree. In the high-resolution XPS spectra, the W 4f peak of WO_3@$F_{0.1}$-C exhibits a slight shift, when compared to that of WO_3@C, suggesting a modified electronic structure due to the F doping. The DFT calculations disclose that the energy barrier for OH deprotonation is lowered by the F-doping, and the hydroxyl adsorption is enhanced by WO_3.

The fabrication of semi-oxidized transition metal oxide nanoparticles anchored on carbon produces highly active defective metal (oxy)hydroxides during the OER, and that could enhance the performance of the OER. Wang *et al.*[41] observed that Co-CoO/GO (graphene oxide) exhibits enhanced activity and stability for the OER. It was synthesized by sonication for 1 h followed by hydrothermal treatment followed by annealing at 450 °C for 30 min under an Ar atmosphere. Co-CoO/GO exhibits higher activity and lower charge transfer resistance for the OER than Co/GO, and Co_3O_4/GO. It contains metallic Co, crystalline CoO, and graphene oxide. It contains Co, C, and O, which are homogeneously distributed. It exhibits the formation of defective CoOOH during the OER.

Constructing Mott–Schottky heterojunctions could lead to the spontaneous flow of electrons at the metal–semiconductor heterointerfaces till the work functions reach equilibrium on both sides, and that could modify the electronic structure, provide optimal adsorption energy with intermediates, enhance the conductivity, and that could enhance the performance for the HER and OER. Li *et al.*[42] observed that Ni/CeO_2@N-CNFs exhibit enhanced activity and stability for the HER and OER (CNFs: carbon nanofibers). They were synthesized by electrospinning followed by stabilization at 250 °C for 2 h followed by carbonization at 600 °C for 3 h under an N_2 atmosphere. The Ni/CeO_2@N-CNFs exhibits higher activity and electrochemical surface area for the HER and OER than Ni@N-CNFs and CeO_2@N-CNFs. It is composed of crystalline Ni/CeO_2 nanoparticles, which are encased into N-doped carbon nanofibers. It exhibits a heterointerface between Ni and CeO_2. It contains Ce, Ni, O, and N, which are homogeneously distributed. In the high-resolution XPS spectra, the Ce 3d peak of Ni/CeO_2@N-CNFs exhibits a slight negative shift, when compared to that of CeO_2@N-CNFs, while the Ni 2p peak of Ni/CeO_2@N-CNFs exhibits a slight positive shift, when compared to that of Ni@N-CNFs, suggesting a modified electronic structure possibly due to the partial transfer of electrons from Ni to CeO_2 at the heterointerface in Ni/CeO_2@N-CNFs. It contains oxygen vacancies. It is porous. For overall water splitting in 1 M KOH, the Ni/CeO_2@N-CNFs//Ni/CeO_2@N-CNFs affords a potential of 1.56 V at 10 mA cm^{-2}, suggesting its very high activity, while it undergoes negligible decay for 100 h, suggesting its very high stability.

2.1.2. Constructing hydroxide electrocatalysts. Annealing at a moderate temperature on electrodeposited transition metal hydroxides could enhance the conductivity by removing a part of the intercalated water to achieve high performance for the OER. Tao *et al.*[43] observed that the annealed α-$Ni(OH)_2$ exhibits enhanced activity and stability for the OER. It was prepared on etched Ti foil by electrodeposition followed by annealing at 150 °C for 1 h under an air atmosphere. The annealed α-$Ni(OH)_2$ exhibits higher activity and lower charge transfer resistance for the OER than as-deposited $Ni(OH)_2$, suggesting the enhanced performance on annealed α-$Ni(OH)_2$ due to the improved conductivity. The annealing treatment leads to the removal of a fraction of the intercalated water in the as-deposited α-$Ni(OH)_2$, causing enhanced conductivity and activity for the OER. Moreover, it exhibits the formation of highly active γ-$Ni^{2.63}O_{0.63}(OH)_{1.37}$ during the OER.

Reduction and oxidation can occur by applying pulsed potentials on the substrate in the electrochemical method; while utilizing this strategy, a scalable, ultrafast, and energy-efficient synthesis route can be achieved for the fabrication of highly active electrocatalysts at ambient temperature, which is highly desirable for green synthesis. Liu *et al.*[26] observed that the IronCE10s exhibit enhanced activity and stability for the OER, while it was prepared on the cheap iron substrate by applying pulsed potentials for 10 s (+2.4 V for 5 s followed by −2.4 V for 5 s) in $NiSO_4$ electrolyte at 25 ± 1 °C, where the substrate was used as a counter electrode. The IronCE10s exhibits higher activity for the OER than

IronWE10s, IronCE5s, IronCE60s, and IronCE360s. It contains Ni, Fe, and O, while it may be iron-doped amorphous nickel hydroxide. The morphology of the prepared samples was a nanosheet array.

The effect of the substrate in the electrodeposition process could alter the conductivity and electrochemical surface area of the electrocatalyst, and that could influence the performance of the OER. Yin *et al.*[44] observed that FeNiOH on Ni foil exhibits enhanced activity and stability for the OER. It was obtained on the cleaned Ni foil by the electrodeposition method at 20 °C for 600 s. FeNiOH on Ni foil exhibits higher activity, higher electrochemical surface area, and lower charge transfer resistance for the OER than FeNiOH on Fe foil. It is an amorphous FeNi hydroxide, which is distributed homogeneously. It possesses nanostructured morphology. For the OER in 1 M KOH, it affords an η of 200 mV at 10 mA cm^{-2}, suggesting its very high activity, while it undergoes negligible decay at 90 mA cm^{-2} after 1000 cycles of CV, suggesting its high durability.

Fabrication of transition bimetallic hydroxides through a facile synthesis route at ambient temperature could enhance the performance of the OER. Zhuo *et al.*[45] demonstrated a rapid, facile, cost-effective, and scalable (area: 2000 cm^2) synthesis route at room temperature for Ni(Fe)$(OH)_2$, where it was synthesized by submerging the pre-cleaned Ni foam for 60 s in 0.2 M Fe$(NO_3)_3$ at ambient temperature, while it exhibits high activity and stability for the OER. The incorporation of Fe in Ni hydroxide and the *in situ* formation of Ni(Fe)OOH from Ni(Fe)$(OH)_2$ during electrolysis are attributed to the enhancement in the performance for the OER. For the OER in 1 M KOH, it affords an η of 240 mV at 10 mA cm^{-2}, and an η of 680 mV at a current density of 1000 mA cm^{-2}, suggesting its significantly high activity, while it affords high stability.

Metal–organic frameworks (MOFs) can be converted into hydroxides/(oxy)hydroxides with abundant oxygen vacancies and mesopores using an alkaline hydrolysis–oxidation strategy with the assistance of an electric field, and that could modify the electronic structure, afford optimal adsorption energy with intermediates, enhance the electrochemical surface area, and that could enhance the performance for the OER. Li *et al.*[46] observed that CoNiFe-OH exhibits enhanced activity and stability for the OER. It was synthesized by the following steps. At first, Co/Ni/Fe MOFs were obtained on Ni foam by hydrothermal treatment. Finally, CoNiFe-OH was obtained using an alkaline hydrolysis–oxidation strategy with the assistance of an electric field (at 1.45 V for 30 min), where Co/Ni/Fe MOFs were used as the working electrode, and 1 M KOH was used as the electrolyte. The CoNiFe-OH exhibits higher activity and electrochemical surface area for the OER than CoNiFe-H. It is polycrystalline, containing Co$(OH)_2$, CoOOH, Ni$(OH)_2$, NiOOH, and FeOOH phases. It contains Fe, Co, Ni, and O, which are homogeneously distributed. It contains oxygen vacancies. It possesses nanostructured ultrathin hexagonal plate-like morphology. It is mesoporous. For the OER in 1 M KOH, it affords an η of 207 mV at 10 mA cm^{-2}, suggesting its very high activity.

Doping of cerium into NiFe hydroxide could increase the valence state of Fe, modify the electronic structure, and afford optimal adsorption energy with intermediates, and that could enhance the performance of the OER. Liu *et al.*[47] observed that Ce-NiFe exhibits enhanced activity and stability for the OER. It was prepared on NiFe foam by the electrodeposition method. Ce-NiFe exhibits higher activity and electrochemical surface area for the OER than NiFe, CeNi, and CeFe. It is an amorphous Ce-doped NiFe hydroxide. It contains Ce, Ni, Fe, and O, which are homogeneously distributed. In the high-resolution XPS spectra, the Ni 2p and Fe 2p peaks of Ce-NiFe exhibit a slight positive shift, when compared to that of NiFe, suggesting a modified electronic structure. It contains high valence Fe ions (Fe > 3+). For the OER in 1 M KOH, it affords an η of 195 mV at 10 mA cm^{-2}, and an η of ~770 mV at a current density of 1000 mA cm^{-2}, suggesting its very high activity, while it affords reasonable stability at a current density of 1000 mA cm^{-2} for 100 h, suggesting its very high stability.

Fabrication of nanostructured transition bimetallic carbonate hydroxides could modify the electronic structure, afford optimal adsorption energy with intermediates, facilitate the evolution of gas, and expose abundant active sites, and that could boost the performance for the HER and OER. Hui *et al.*[17] observed that Fe-Co-CO_3-OH exhibits significantly very high activity and stability for the HER and OER. It was obtained on Ni foam by the hydrothermal treatment. Fe-Co-CO_3-OH exhibits higher activity for the HER and OER than Co-CO_3-OH and Fe-CO_3-OH. It is Fe-doped Co carbonate hydroxide. It is crystalline. It exhibits a homogeneous distribution of Fe and Co. In the high-resolution XPS spectra, the Co 2p peak of Fe-Co-CO_3-OH exhibits a slight shift, when compared to Co-CO_3-OH, suggesting a modified electronic structure due to the Fe doping. It possesses nanosheet array morphology. For the OER in 1 M KOH, it affords an η of 228 mV at 10 mA cm^{-2}, and an η of 308 mV at a current density of 1000 mA cm^{-2}, suggesting its substantially very high activity. For the HER in 1 M KOH, it affords an η of −77 mV at −10 mA cm^{-2}, and an η of −256 mV at a current density of −1000 mA cm^{-2}, suggesting its substantially very high activity, while it undergoes negligible decay at a current density of −1000 mA cm^{-2} after 10 000 cycles of CV, suggesting its substantially very high durability. Moreover, Tang *et al.*[48] observed that Co-Mn-CO_3-OH exhibits enhanced activity and stability for the HER and OER. It was obtained on Ni foam by hydrothermal treatment. Co-Mn-CO_3-OH exhibits higher activity and electrochemical surface area for the HER and OER than Co-CO_3-OH and $MnCO_3$. It is Mn-doped Co carbonate hydroxide. It has low crystallinity. It contains Mn, Co, C, and O, which are homogeneously distributed. The number of electrons present in the 3d orbital of the Co atom in Co-Mn-CO_3-OH is about 7.30, which is higher than that of Co-CO_3-OH, suggesting the modified electronic structure possibly due to the partial transfer of electrons from Mn to Co. It possesses nanosheet array morphology. For the OER in 1 M KOH, it affords an η of 462 mV

at a current density of 1000 mA cm^{-2}, suggesting its very high activity.

2.1.3. Constructing (oxy)hydroxide electrocatalysts. Creating abundant defects in Fe (oxy)hydroxide could generate highly active species after electrochemical activation, and enhance the conductivity, and performance of the OER. Hu *et al.*[49] observed that the Defect-FeOOH activated exhibits enhanced activity and stability for the OER. It was obtained by a solvothermal treatment followed by electron beam irradiation followed by electrochemical activation. The Defect-FeOOH activated exhibits higher activity and lower charge transfer resistance for the OER than FeOOH activated. The Defect-FeOOH is composed of the β-FeOOH phase with abundant defects (without oxygen vacancies), while it contains a mixed phase (α-FeOOH and β-FeOOH) after electrochemical activation. It contains high valence Fe ions ($Fe^{3.13+}$). It possesses nanorod morphology.

Doping sulfur in Fe (oxy)hydroxide could activate the redox reactivities of the lattice oxygen and Fe, and that could enhance the performance of the OER. Therefore, fabricating sulfur-doped Fe (oxy)hydroxide at ambient temperature through a facile, scalable, energy-efficient, and ultrafast synthesis route is highly desirable for green synthesis. Chen *et al.*[24] observed that S-FeOOH exhibits enhanced activity and stability for the OER. It was obtained by immersing the cleaned Fe foam for 20 min at room temperature in the solution containing $Fe(NO_3)_3$ and $Na_2S_2O_3$. S-FeOOH exhibits higher activity and electrochemical surface area for the OER than FeOOH. It is polycrystalline, containing S-doped β-FeOOH. It exhibits a homogeneous distribution of S. In the high-resolution XPS spectra, the Fe 2p peak of S-FeOOH slightly shifts, when compared to that of FeOOH, suggesting a modified electronic structure due to the S doping. It contains oxygen vacancies. The redox reactivities of the lattice oxygen and Fe in FeOOH are activated due to S doping. It possesses nanosheet array morphology. For the OER in 1 M KOH, it affords an η of 244 mV at 10 mA cm^{-2}, suggesting its very high activity, while it exhibits negligible decay at 20 mA cm^{-2} for 100 h, suggesting its very high stability.

The role of cations in the electrolyte could influence the activity of the OER. Hou *et al.*[50] observed that the activity of the NiFe-(OOH)-based catalyst for the OER in different electrolytes is in the following order: CsOH > KOH > NaOH > LiOH. The catalytic activity trend is nearly associated with the potential for maximum entropy of the system. The catalytic activity has been nearly related to the variable length of Ni–O bonds in the NiOOH active phase structure.

Fabrication of transition bimetallic alloy/(oxy) hydroxide heterostructures could tune the electronic structure, afford optimal adsorption energy with intermediates, expose abundant active sites, improve charge/mass transfer, facilitate gas evolution, and that could improve the performance for the HER and OER. lv *et al.*[11] observed that c-NiFe/a-NiFeOOH@NiMo (c: crystalline; a: amorphous) exhibits enhanced activity and stability for the HER and OER. It was obtained on carbon fiber cloth by galvanostatic electrodeposition at ~0 °C followed by cyclic voltammetry treatment followed by potentiostatic electrodeposition. c-NiFe/a-NiFeOOH@NiMo exhibits higher activity and lower charge transfer resistance for the HER and OER than c-NiFe/a-NiFeOOH and NiMo. It contains heterojunctions. It exhibits a core–shell structure, containing NiMo particles as the core, and thin c-NiFe/a-NiFeOOH nanosheets as the shell, where the thin nanosheet is composed of crystalline NiFe nanoflowers (cubic $Ni_{0.36}Fe_{0.64}$ alloy), which are embedded in amorphous NiFeOOH. a-NiFeOOH contains nanosized pores. The ultrafine NiFe alloy nanocrystals possesses abundant edges and high electronic conductivity, and the amorphous NiFeOOH support possesses abundant defects and nanosized pores, while the NiMo alloy can afford firm grasp to the c-NiFe/a-NiFeOOH nanosheets, and that could modify the electronic structure, provide optimal adsorption energy with intermediates, expose abundant active sites, enhance charge/mass transfer, facilitate gas evolution, which could enhance the performance for the HER and OER. For the OER in 1 M KOH, c-NiFe/a-NiFeOOH@NiMo affords 133.2 mV at 20 mA cm^{-2}, suggesting its very high activity. For the HER in 1 M KOH, it affords an η of −91.9 mV at −20 mA cm^{-2}, suggesting its very high activity. For overall water splitting in 1 M KOH, c-NiFe/a-NiFeOOH@NiMo// c-NiFe/a-NiFeOOH@NiMo affords a potential of 1.45 V at 10 mA cm^{-2}, suggesting its very high activity, while it affords 95.86% retention at 100 mA cm^{-2} for 100 h, suggesting its very high stability.

The fabrication of NiFe-based electrocatalysts for the OER through an electrodeposition process using a deep eutectic solvent (DES) with Ni as a source in the form of nitrate could form multi vacancies upon electrolysis, and that could enhance the performance for the OER. Wei *et al.*[6a] fabricated NiFe based electrocatalysts for the OER through a one-step electrodeposition process, where Fe was used as a sacrificial anode and ethaline-based DES with nickel nitrate was used as an electrolyte. The utilization of nitrate ions in the electrodeposition process for the preparation of NiFe based catalysts could generate multiple vacancies (such as O, Ni, and Fe vacancies) during water oxidation, leading to optimal adsorption energies with intermediates, and that could boost the performance for the OER. For the OER in 1 M KOH, it affords an η of 256 mV at 10 mA cm^{-2}, suggesting its high activity.

2.1.4. Fabricating layered double hydroxide (LDH) electrocatalysts. Fabrication of highly active transition bimetallic LDH as an electrocatalyst at ambient temperature through a facile energy-efficient synthesis route is highly desirable for green synthesis. Zhao *et al.*[25] observed that the NiFe LDH exhibits enhanced activity and stability for the OER. It was prepared by immersing cleaned, acid-treated Fe foam in $NiSO_4$ solution under ambient conditions. It is composed of four layers, an Fe foam substrate at the bottom, nanoparticle aggregates on the substrate, an interfacial film, and nanosheets at the top. It is NiFe LDH with a rhombohedral structure. It

contains Ni, Fe, and O, which are homogeneously distributed. It affords reasonable stability at 100 mA cm^{-2} for 192 h, suggesting its very high stability.

The electrochemical activation of transition bimetallic LDH can reconstruct the surface, which could generate highly active sites, enhance the surface area, and that could improve the performance of the HER and OER. Pehlivan *et al.*[51] observed that the NiFe LDH activated exhibits enhanced activity for the HER and OER. Crystalline NiFe LDH was synthesized on pretreated Ni foam by hydrothermal treatment. NiFe LDH activated affords an η of 201 mV at 10 mA cm^{-2} for the OER, and it affords an η of −189 mV at −10 mA cm^{-2} for the HER in 1 M KOH, suggesting its very high activity.

Transition bimetallic catalysts having a structure almost similar to the NiFe LDH can be fabricated by the spray pyrolysis deposition technique, and that could enhance the activity and stability of the OER. An *et al.*[52] observed that the NiFe-based catalyst exhibits enhanced activity and stability for the OER. It was obtained on a fluorine-doped tin oxide glass substrate by an ultrasonic spray pyrolysis deposition method. The NiFe-based catalyst aged at 0 min exhibits higher activity and lower charge transfer resistance for the OER than the NiFe-based catalyst aged at 2, 4, and 8 min. It is composed of NiFe oxide and layered hydroxyl nitrate. The structure of the NiFe-based catalyst is almost similar to the that of the typical NiFe LDH. It contains Fe, Ni, O, and N with a film thickness of 100 nm and uniform coral-like stripes.

Fabrication of heterostructured metal (oxy)hydroxide/transition bimetallic LDH through a facile one-step synthesis route is highly desirable. Li *et al.*[53] observed that the FeOOH@NiFe LDH exhibits enhanced activity and stability for the OER. It was synthesized by immersing the cleaned Ni foam in $FeCl_3$ solution at 100 °C for 5 s. FeOOH@NiFe LDH exhibits higher activity, higher electrochemical surface area, and lower charge transfer resistance for the OER than FeOOH and NiFe LDH. It is crystalline, containing β-FeOOH and NiFe LDH phases. It exhibits a heterointerface. It contains Fe, Ni, and O, which are uniformly distributed. It possesses nanosheet array morphology. During the OER, it is converted into highly active FeOOH@β-Ni(Fe)OOH phases. For the OER in 1 M KOH, it affords an η of 210 mV at 10 mA cm^{-2}, suggesting its very high activity, while it undergoes negligible decay for 100 h, suggesting its very high stability.

Negatively charged metal nanoparticles can be integrated with positively charged transition bimetallic LDH due to the electrostatic attraction by the physical blending method, which could modify the electronic structure, and that could enhance the performance of the OER. Wu *et al.*[54] observed that the Ag@NiFe LDH exhibits enhanced activity and stability for the OER. It was prepared by the physical blending method, where Ag@NiFe LDH can be precipitated when adding Ag with NiFe LDH due to the electrostatic attraction between positively charged NiFe LDH and negatively charged Ag nanoparticles, while the NiFe LDH was prepared by hydrothermal treatment. Ag@NiFe LDH exhibits higher activity, higher electrochemical surface area, and lower charge transfer resistance for the OER than Au@NiFe LDH and NiFe LDH. It is crystalline. It is composed of metallic Ag nanoparticles, which are anchored on NiFe LDH nanosheets. It exhibits a heterointerface. In the high-resolution XPS spectra, the Ni 2p and Fe 2p peaks of Ag@NiFe LDH exhibit a slight positive shift, when compared to that of NiFe LDH, while the Ag 3d peaks of Ag@NiFe LDH exhibit a slight negative shift, when compared to that of metallic Ag, suggesting a modified electronic structure possibly due to the partial transfer of electrons from NiFe LDH to Ag.

Doping of cerium into transition bimetallic LDH could modify the electronic structure, and that could enhance the performance of the HER and OER. Dhandapani *et al.*[55] observed that the Ce@NiCo LDH exhibits enhanced activity and stability for the HER and OER. It was obtained on cleaned Ni foam by hydrothermal treatment. Ce@NiCo LDH exhibits higher activity and lower charge transfer resistance for the HER and OER than NiCo LDH. It is 25.5% Ce doped NiCo LDH. It contains Ce, Ni, Co, and O, which are homogeneously distributed. In the high-resolution XPS spectra, the Co 2p peak of Ce@NiCo LDH exhibits a slight shift compared to that of NiCo LDH, suggesting a modified electronic structure. It possesses nano petal morphology.

Heterostructured transition bimetallic phosphide/bimetallic LDH can be obtained by the partial phosphidation of bimetallic LDH, and that could modify the electronic structure, afford optimal adsorption energy with intermediates, which could enhance the activity and stability for the HER and OER. Zheng *et al.*[56] observed that the c-CoFeP/a-CoFe LDH exhibits enhanced activity and stability for the OER, whereas the c-CoMnP/a-CoMn LDH (c: crystalline; a: amorphous) exhibits enhanced activity and stability for the HER. The c-CoFeP/a-CoFe LDH or c-CoMnP/a-CoMn LDH was prepared on pretreated Ni foam by hydrothermal treatment followed by partial phosphidation for 2 h at 250 °C under an Ar atmosphere. The c-CoFeP/a-CoFe LDH exhibits higher activity and electrochemical surface area for the OER than c-CoMnP/a-CoMn LDH, c-CoNiP/a-CoNi LDH, c-CoCuP/a-CoCu LDH, and c-CoZnP/a-CoZn LDH. The c-CoMnP/a-CoMn LDH exhibits higher activity and electrochemical surface area for the HER than c-CoFeP/a-CoFe LDH, c-CoNiP/a-CoNi LDH, c-CoCuP/a-CoCu LDH, and c-CoZnP/a-CoZn LDH. The c-CoFeP/a-CoFe LDH is the crystalline CoFeP decorated amorphous CoFe LDH heterostructure. It possesses a nanostructure. The c-CoMnP/a-CoMn LDH is the crystalline CoMnP decorated amorphous CoMn LDH heterostructure. It possesses a nanostructure. For overall water splitting in 1 M KOH, the c-CoFeP/a-CoFe LDH^{OER}//c-CoMnP/a-CoMn LDH^{HER} affords a potential of 1.498 V at 10 mA cm^{-2}, confirming its very high activity.

Integrating LDH with MXene could modify the electronic structure and provide optimal adsorption energy with intermediates, enhancing the activity and stability of the HER and OER. Yu *et al.*[57] observed that the NiFeLa LDH/v-MXene

(vertically aligned MXene) exhibits significantly very high activity and stability for the HER and OER. It was synthesized *via* the following steps: at first, Ti_3C_2 MXene nanosheets were prepared by selectively etching Al layers in Ti_3AlC_2. Then, vertically aligned Ti_3C_2 MXene was obtained on Ni foam by electrophoretic deposition followed by freeze-drying. Finally, NiFeLa LDH/v-MXene was obtained by electrodeposition. The NiFeLa LDH/v-MXene exhibits higher activity for the HER and OER than NiFe-LDH/v-MXene, NiFeLa LDH/MXene, NiFeLa LDH, and v-MXene. It comprises amorphous NiFeLa LDH nanosheets on crystalline Ti_3C_2 MXene nanosheets, where the MXene is vertically aligned on Ni foam. It contains Ti, C, Ni, Fe, La, and O, which are homogeneously distributed. In the high-resolution XPS spectra, the Ni 2p peak of NiFeLa LDH/v-MXene exhibits a slight positive shift compared to that of NiFe LDH/v-MXene, suggesting a modified electronic structure. It exhibits super hydrophilicity with a contact angle of 0°. For the OER in 1 M KOH, it affords an η of 191 mV at 10 mA cm^{-2}, suggesting its very high activity. In contrast, it undergoes negligible decay at 100 mA cm^{-2} for 1200 h, suggesting its robust stability. For the HER in 1 M KOH, it affords an η of -38 mV at -10 mA cm^{-2}, suggesting its very high activity, while it affords reasonable stability at -100 mA cm^{-2} for 400 h, suggesting its very high stability, and it undergoes negligible decay at -700 mA cm^{-2} after 2000 cycles of CV, suggesting its high durability. For overall water splitting in 1 M KOH, the NiFeLa LDH/v-MXene//NiFeLa LDH/v-MXene affords a potential of 1.48 V at 10 mA cm^{-2}, suggesting its very high activity, while it undergoes negligible decay at 100 mA cm^{-2} for 400 h, suggesting its robust stability.

2.2. Fabricating chalcogenide (sulfide and selenide) electrocatalysts

2.2.1. Fabricating sulfide electrocatalysts. Doping cobalt in nickel sulfide could modify the electronic structure, boosting the performance of the HER and OER. Li *et al.*[58] observed that Co-Ni_3S_2 exhibits enhanced activity and stability for the HER and OER. It was prepared on cleaned Ni mesh by electrodeposition followed by hydrothermal sulfurization. It is Co-doped rhombohedral Ni_3S_2. It contains Ni, Co, and S, which are homogeneously distributed. In the high-resolution XPS spectra, the Ni 2p peak of Co-Ni_3S_2 exhibits a slight shift when compared to that of Ni_3S_2, suggesting a modified electronic structure due to Co doping. It possesses a leaf-like morphology.

Fabrication of cobalt-doped nickel sulfide having an ultrathin nanostructure could modify the electronic structure and facilitate the evolution of gas even at high current densities, boosting the performance of the HER and OER. Jian *et al.*[59] observed that Co-Ni_3S_2 having an ultrathin nanosheet structure exhibits enhanced activity and stability for the HER and OER even at a current density of 1000 mA cm^{-2}, while it was obtained on pretreated Ni foam by a one-step hydrothermal treatment. Co-Ni_3S_2 exhibits higher activity for the HER and OER than Ni_3S_2. It is a Co-doped crystalline Ni_3S_2. It contains Ni, Co, and S, which are homogeneously distributed. It possesses an ultrathin nanosheet structure. For the OER in 1 M KOH, it affords an η of 310 mV at 50 mA cm^{-2} and an η of 750 mV at a current density of 1000 mA cm^{-2}, suggesting its very high activity, while it undergoes negligible decay at a current density of 1000 mA cm^{-2} after 1000 cycles of CV, suggesting its high durability. For the HER in 1 M KOH, it affords an η of -220 mV at -50 mA cm^{-2} and an η of -850 mV at a current density of -1000 mA cm^{-2}, suggesting its very high activity, while it undergoes negligible decay at a current density of -1000 mA cm^{-2} after 1000 cycles of CV, suggesting its high durability.

Besides, Jian *et al.*[14] observed that Sn-Ni_3S_2 exhibits substantially very high activity and stability for the HER and OER. It was synthesized on Ni foam by a one-step hydrothermal treatment. Sn-Ni_3S_2 exhibits higher activity for the HER and OER than Ni_3S_2, while it exhibits lower charge transfer resistance for the OER than Ni_3S_2. It is Sn-doped hexagonal Ni_3S_2. It contains Sn, Ni, and S, which are homogeneously distributed. It possesses an ultrathin nanosheet structure. For the OER in 1 M KOH, it affords an η of 267 mV at 100 mA cm^{-2} and an η of 580 mV at a current density of 1000 mA cm^{-2}, suggesting its significantly very high activity, while it undergoes negligible decay at a high current density of 2000 mA cm^{-2} after 10 000 cycles of CV, suggesting its substantially very high durability. For the HER in 1 M KOH, it affords an η of -171 mV at -100 mA cm^{-2} and an η of -570 mV at a current density of -1000 mA cm^{-2}, suggesting its significantly very high activity, while it undergoes negligible decay at a current density of -1000 mA cm^{-2} after 10 000 cycles of CV, suggesting its significantly very high durability. For overall water splitting in 1 M KOH, Sn-Ni_3S_2//Sn-Ni_3S_2 affords a potential of 1.46 V at 10 mA cm^{-2} and ~2.65 V at a current density of 1000 mA cm^{-2}, suggesting its significantly very high activity.

Moreover, Mao *et al.*[60] observed that FeCo-Ni_3S_4 exhibits enhanced activity and stability for the OER. It was prepared on pretreated Ni foam by hydrothermal treatment followed by hydrothermal sulfurization. FeCo-Ni_3S_4 exhibits higher activity, higher electrochemical surface area, and lower charge transfer resistance for the OER than Fe-Ni_3S_4, Co-Ni_3S_4, and Ni_3S_4. It is Fe and Co dual-doped cubic Ni_3S_4. It contains Ni, S, Fe, and Co, which are homogeneously distributed. It exhibits a higher amount of high valence Ni ions (Ni^{3+}) than Ni_3S_4. In the high-resolution XPS spectra, the Ni 2p peak of FeCo-Ni_3S_4 exhibits a slight shift when compared to that of Ni_3S_4, suggesting a modified electronic structure due to the Fe and Co dual doping. It possesses nanosheet array morphology. For the OER in 1 M KOH, it affords an η of 230 mV at 20 mA cm^{-2}, suggesting its very high activity, while it exhibits 22 mV decay at 20 mA cm^{-2} for 360 h, suggesting its very high stability, and it undergoes negligible decay at 100 mA cm^{-2} after 3000 cycles of CV, suggesting its very high durability.

Besides, Zhang *et al.*[61] reported that Fe, Ce-Ni_xS_y exhibits enhanced activity and stability for the HER and OER. It was synthesized on the pretreated Ni foam by a one-step hydrothermal treatment. Fe, Ce-Ni_xS_y exhibits higher activity and

electrochemical surface area for the OER than Fe-Ni_xS_y, Ce-Ni_xS_y, and Ni_xS_y. In comparison, it exhibits higher activity for the HER than Fe-Ni_xS_y, Ce-Ni_xS_y, and Ni_xS_y. It is Ce, Fe dual doped Ni_xS_y, where Ni_xS_y is crystalline, containing trigonal Ni_3S_2 and orthorhombic Ni_9S_8. It contains Ni, Fe, Ce, and S, which are homogeneously distributed. In the high-resolution XPS spectra, the Ni 2p peak of Fe, Ce-Ni_xS_y exhibits a slight shift compared to that of Ni_xS_y, suggesting a modified electronic structure possibly due to the doping of Fe and Ce. It possesses nano forest array morphology.

Moreover, Huang *et al.*[62] observed that Fe-NiS-NiS_2 exhibits enhanced activity and stability for the HER and OER. It was prepared by co-precipitation followed by hydrothermal treatment followed by annealing at 350 °C for 2 h under an N_2 atmosphere. Fe-NiS-NiS_2 exhibits higher activity and electrochemical surface area for the HER and OER than Fe-NiS_2 and NiS-NiS_2. It is Fe-doped crystalline NiS-NiS_2. It exhibits the heterojunctions at a higher amount of high valence Ni ions (Ni^{3+}) when compared to Fe-NiS_2. In the high-resolution XPS spectra, the Ni 2p peak of Fe-NiS-NiS_2 exhibits a slight positive shift compared to that of Fe-NiS_2, suggesting a modified electronic structure. It possesses a microsphere structure, where the microsphere is composed of nanoplates.

In addition, Fereja *et al.*[63] have observed that W-NiS_2/MoO_2 exhibits enhanced activity for the HER and OER. It was obtained on cleaned carbon cloth by hydrothermal treatment followed by sulfurization at 400 °C for 2 h under an H_2/Ar atmosphere. W-NiS_2/MoO_2 exhibits higher activity and electrochemical surface area for the HER than NiS_2/MoO_2, W-NiS_2, and W-MoO_2. It is W doped NiS_2/MoO_2. It exhibits the heterojunctions between the NiS_2 and MoO_2 phases. It contains W, Ni, Mo, S, and O, which are homogeneously distributed. In the high-resolution XPS spectra, the Ni 2p peak of W-NiS_2/MoO_2 exhibits a slight positive shift compared to that of NiS_2. The Mo 3d peak of W-NiS_2/MoO_2 exhibits a slight negative shift when compared to that of MoO_2, suggesting a modified electronic structure in W-NiS_2/MoO_2 possibly due to the partial transfer of electrons from NiS_2 to MoO_2, which could be due to the higher electronegativity of Mo when compared to that of Ni. It contains mesopores. For the HER in 1 M KOH, it affords an η of -52 mV at -10 mA cm^{-2}, suggesting its very high activity.

Fabrication of nickel sulfide/molybdenum sulfide as Mott–Schottky heterojunctions could lead to the spontaneous flow of electrons at the metal–semiconductor heterointerfaces till the work functions reach equilibrium on both sides, and that could modify the electronic structure, afford optimal adsorption energy with intermediates, improve the conductivity, which could boost the performance for the HER and OER. Gu *et al.*[64] observed that NiS/MoS_2 exhibits enhanced activity and stability for the HER and OER. It was obtained on pre-cleaned carbon cloth by a one-step hydrothermal treatment. NiS/MoS_2 exhibits higher activity, higher electrochemical surface area, and lower charge transfer resistance for the HER than NiS and MoS_2. It is crystalline, containing hexagonal NiS and hexagonal MoS_2, while it exhibits a heterojunction interface between NiS and MoS_2. It contains Mo, Ni, and S, which are homogeneously distributed. In the high-resolution XPS spectra, the Ni 2p peak of NiS/MoS_2 exhibits a slight negative shift compared to that of NiS. In contrast, Mo 3d peak of NiS/MoS_2 exhibits a slight positive shift compared to that of MoS_2, suggesting a modified electronic structure possibly due to the partial transfer of electrons from MoS_2 to NiS. It exhibits superior hydrophilicity, having a water contact angle of 15.72°. It possesses a flower-like morphology due to a combination of numerous nanosheets. For the HER in 1 M KOH, it affords an η of -87 mV at -10 mA cm^{-2}, suggesting its very high activity. For water splitting in 1 M KOH, NiS/MoS_2//NiS/MoS_2 affords a potential of 1.51 V at 10 mA cm^{-2}, suggesting its very high activity. At the same time, it exhibits 99.2% retention for 50 h, suggesting its very high stability. Besides, Yang *et al.*[65] observed that Ni_3S_2-MoS_2 exhibits enhanced activity and stability for the HER and OER. It was synthesized on pretreated Ni foam by a one-step hydrothermal treatment. Ni_3S_2–MoS_2 exhibits higher activity and lower charge transfer resistance for the HER than Ni_3S_2 and MoS_2. It is crystalline, containing Ni_3S_2 and MoS_2 phases. It exhibits heterointerfaces between Ni_3S_2 and MoS_2. It contains Mo, Ni, and S, which are homogeneously distributed. In the high-resolution XPS spectra, the Ni 2p peak of Ni_3S_2-MoS_2 and Mo 3d peak of Ni_3S_2-MoS_2 showed a slight shift as compared to Ni_3S_2 and MoS_2, respectively, illustrating the modified electronic structure possibly due to the partial transfer of electrons between Ni_3S_2 and MoS_2. It exhibits 3D porous flower morphology, where the flower is composed of nanosheets.

Metal (oxy)hydroxides for the OER and metallic species for the HER are formed as the active species due to the dynamic structural reconstruction of heterostructured metallic sulfide/bimetallic sulfide pre-catalysts during water electrolysis to boost the performance for the HER and OER. Wu *et al.*[66] observed that Ni_3S_2/$FeNi_2S_4$ showed high activity and stability for the HER and OER. It was synthesized on NiFe foam by the following steps: first, dual-scale porous NiFe foam was prepared by a redox process. After that, NiFeAl LDH was obtained on the pretreated NiFe foam by hydrothermal treatment. Finally, NiFeAl LDH was converted into Ni_3S_2/$FeNi_2S_4$ by hydrothermal treatment. Ni_3S_2/$FeNi_2S_4$ exhibits higher activity and lower charge transfer resistance for the HER and OER than NiFeAl LDH. It is crystalline, containing Ni_3S_2 and $FeNi_2S_4$ phases. It exhibits heterointerfaces between Ni_3S_2 and $FeNi_2S_4$. It contains Fe, Ni, and S, which are homogeneously distributed, while it exhibits a trace amount of Al (3.4%). Ni_3S_2/$FeNi_2S_4$ act as pre-catalysts, exhibiting dynamic structural reconstruction during water electrolysis, where the metallic Ni^0 for the HER and γ-NiOOH for the OER are the active species formed during electrolysis. It possesses porous, nanosheet array morphology. For the OER and HER in 1 M KOH, it affords an η of 201 mV at 10 mA cm^{-2} and an η of -50 mV at -10 mA cm^{-2}, respectively, showing its better activity. For overall water splitting in 1 M KOH, Ni_3S_2/$FeNi_2S_4$//Ni_3S_2/$FeNi_2S_4$ affords a potential of 1.55 V at 10 mA cm^{-2}, suggesting its very high activity.

Besides, Zhang *et al.*[22] observed that CuS-Ni_3S_2/CuNi exhibits enhanced activity and stability for the OER. It was obtained on pretreated Ni foam by electrodeposition followed by hydrothermal sulfurization. CuS-Ni_3S_2/CuNi exhibits higher activity, higher electrochemical surface area, and lower charge transfer resistance for the OER than Ni_3S_2/Ni. It is crystalline, containing CuS and Ni_3S_2 phases, where CuS–Ni_3S_2 is *in situ* grown on a CuNi alloy. It exhibits heterointerfaces between CuS and Ni_3S_2. It contains Ni, Cu, and S, which are homogeneously distributed. It contains macropores. For the OER in 1 M KOH, it affords an η of 337 mV at 100 mA cm^{-2} and an η of 510 mV at a current density of 1000 mA cm^{-2}, suggesting its very high activity, while it undergoes negligible decay at a current density of 1000 mA cm^{-2} after 5000 cycles of CV, suggesting its high durability.

Moreover, Luo *et al.*[67] observed that MoS_2-MoO_{3-x}/Ni_3S_2 exhibits enhanced activity and stability for the HER. It was prepared on Ni foam by a spontaneous chemical reaction at 80 °C followed by electrodeposition. MoS_2-MoO_{3-x}/Ni_3S_2 exhibits higher activity and lower charge transfer resistance for the HER than MoS_2, MoO_{3-x}, and Ni_3S_2. It comprises a Ni_3S_2 layer on Ni foam, which is covered by the MoS_2–MoO_{3-x} layer on the top. It exhibits a heterostructure. It has low crystallinity. It contains MoS_2 with abundant bridging S_2^{2-} sites, MoO_{3-x}, and Ni_3S_2, which could afford optimal adsorption energy with intermediates. For the HER in 1 M KOH, it affords an η of −76 mV at −10 mA cm^{-2}, suggesting its very high activity.

In addition, Wang *et al.*[68] observed that Ni_xS_y@MnO_xH_y exhibits enhanced activity and stability for the HER and OER. It was obtained on pretreated Ni foam by hydrothermal sulfurization followed by anodic galvanostatic electrodeposition. Ni_xS_y@MnO_xH_y exhibits higher activity, higher electrochemical surface area, and lower charge transfer resistance for the HER and OER than Ni_xS_y and MnO_xH_y. It comprises a rod-like Ni_xS_y, surrounded by MnO_xH_y, where Ni_xS_y comprises Ni_3S_2 and NiS phases. It exhibits a heterointerface between Ni_xS_y and MnO_xH_y. In the high-resolution XPS spectra, the Ni 2p peak of Ni_xS_y@MnO_xH_y exhibits a slight positive shift compared to that of Ni_xS_y, suggesting a modified electronic structure. Moreover, it contains Mn–O, Mn–Mn, and Mn–S bonds, where the existence of the Mn–S bond suggests the presence of electronic interaction at the heterointerface. It possesses a nanostructure. For the OER in 1 M KOH, it affords reasonable stability at 100 mA cm^{-2} for 150 h, suggesting its very high stability, and it undergoes negligible decay at 500 mA cm^{-2} after 5000 cycles of CV, suggesting its high durability. For the HER in 1 M KOH, it affords an η of −179 mV at −10 mA cm^{-2}, suggesting its very high activity, while it affords reasonable stability at −100 mA cm^{-2} for 100 h, suggesting its very high stability. For overall water splitting in 1 M KOH, Ni_xS_y@MnO_xH_y//Ni_xS_y@MnO_xH_y affords a potential of 1.53 V at 10 mA cm^{-2}, suggesting its very high activity. In contrast, it undergoes negligible decay at 100 mA cm^{-2} for 100 h, suggesting its very high stability.

Moreover, Che *et al.*[69] observed that (Ni-Fe)S_x/NiFe$(OH)_y$ exhibits enhanced activity and stability for the HER and OER. It was obtained on pretreated Ni foam by the one-step electrodeposition method at room temperature. (Ni-Fe)S_x/NiFe$(OH)_y$ exhibits higher activity for the HER and OER than $Fe_{0.96}S$/$Fe(OH)_3$. It is an amorphous (Ni-Fe)S_x/NiFe$(OH)_y$ composite. It possesses micro/nano-architecture, and exhibits high wettability with a water contact angle of ≤0°, suggesting its superaerophobic properties, which could facilitate the evolution of gas. For the OER in 1 M KOH, it affords an η of 199 mV at 10 mA cm^{-2} and an η of ∼510 mV at a current density of 1000 mA cm^{-2}, suggesting its very high activity. For overall water splitting in 1 M KOH, (Ni-Fe)S_x/NiFe$(OH)_y$//(Ni-Fe)S_x/NiFe$(OH)_y$ affords a potential of 1.46 V at 10 mA cm^{-2}, suggesting its very high activity.

In addition, Lu *et al.*[70] observed that $FeCoS_x$-PBA exhibits enhanced activity and stability for the OER, where $FeCoS_x$-PBA is composed of amorphous $FeCoS_x$, which is embedded in Prussian blue analog hetero-nanoframes. It possesses a hollow cubic-like morphology, where plenty of nanoparticles are attached to the cubic surface. It contains two forms of S atom, where one is S^{2-} in $FeCoS_x$, while the other is S-doped PBA. In the high-resolution XPS spectra, the Fe 2p peak of $FeCoS_x$-PBA exhibits a slight shift when compared to that of mixed PBA, suggesting a modified electronic structure in $FeCoS_x$-PBA. The following steps are involved in the synthesis: first, PBA was obtained by the precipitation method. Then, mixed PBA was prepared by an ultrasound-assisted ion exchange route. Finally, $FeCoS_x$-PBA was obtained by solvothermal treatment. $FeCoS_x$-PBA exhibits higher activity, higher electrochemical surface area, and lower charge transfer resistance for the OER PBA and mixed PBA.

The incorporation of Ni in iron thiophosphate could tune the electronic structure and increase the electronic conductivity, and that could enhance the activity for the HER and OER. Tang *et al.*[71] observed that Ni-$FePS_3$ exhibits enhanced activity and stability for the HER and OER in 1 M KOH. It was prepared by impregnation–adsorption followed by annealing at 450 °C for 5 minutes in an Ar atmosphere. The Ni-$FePS_3$ exhibits higher activity for the HER and OER than Co-$FePS_3$, Pd-$FePS_3$, and $FePS_3$. The differential electron density of Ni-$FePS_3$ (Structure 1 as shown in Fig. 2a and Structure 2 as shown in Fig. 2b) are provided to understand the causes of the interaction of Ni atom with $FePS_3$, which enhances the catalysis. The interaction of the Ni atom with $FePS_3$ in Ni-$FePS_3$ leads to the flow of electrons of the Fe atom, preferably towards the opposite Ni–S bonding, which causes a large negative charge on S and lesser electron density on Fe, as shown in Fig. 2a. In the same way, the charge distribution at the Ni–S bond changes when the charge of the S atom increases to −0.45 from −0.38, as shown in Fig. 2b. Moreover, the charge of Fe atoms near the Ni atom linked by edge S atom sharing (Fe-S-Ni) increases to 0.74 from 0.7. Structure 2 is considered a more suitable configuration because it exhibits lower formation energy than Structure 1. The

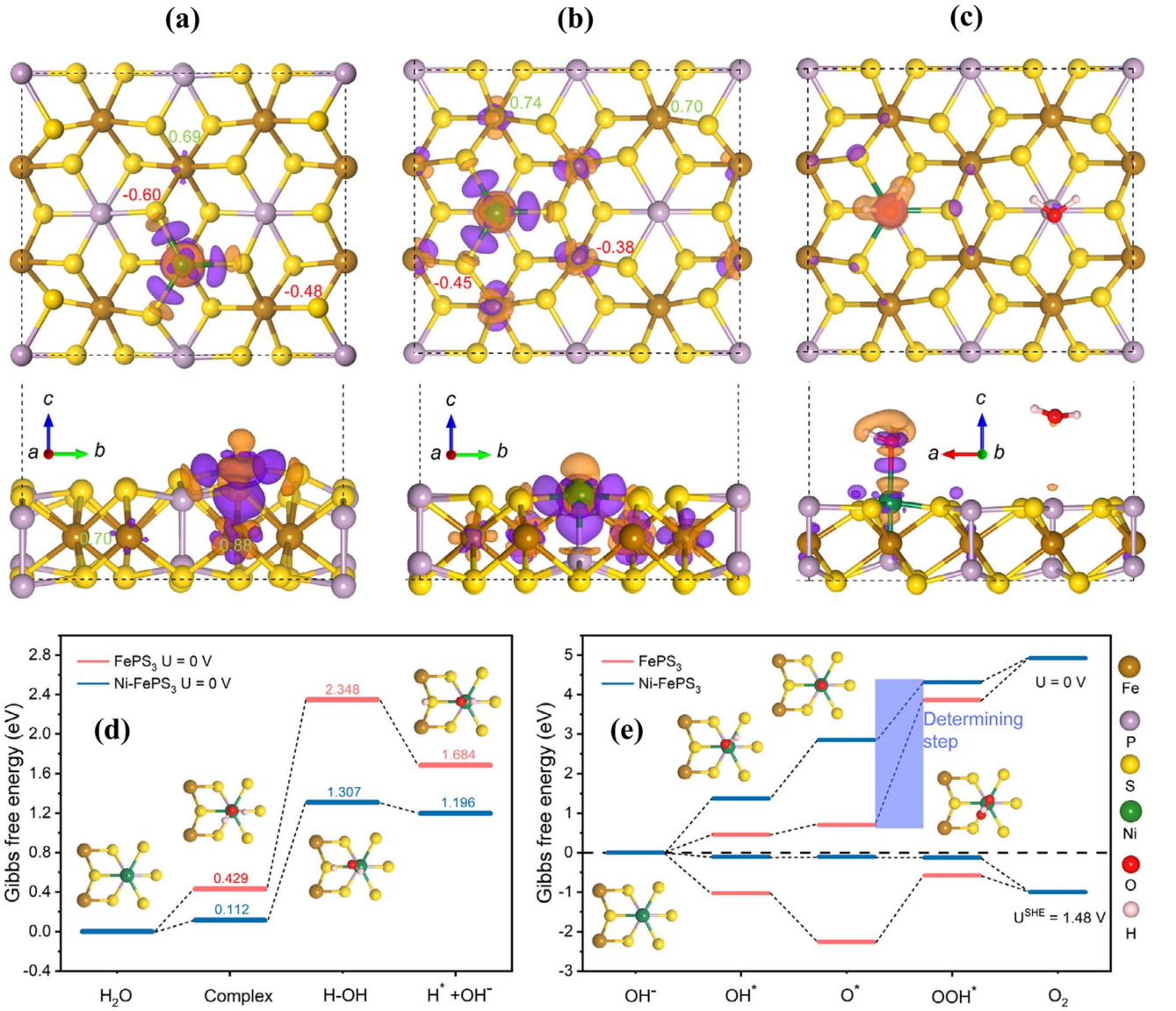

Fig. 2 Differential electron density (top-view and side-view) of (a) Structure 1 and (b) Structure 2 of Ni-$FePS_3$ (iso-surface value: 0.005 eBohr^{-3}), where the red and green color numbers indicate Bader charge numbers of S and Fe, respectively; (c) differential electron density (top-view and side-view) of water adsorbed on the basal plane of Ni-$FePS_3$ (iso-surface value: 0.002 eBohr^{-3}); Gibbs free energy profiles of Ni-$FePS_3$ in comparison with $FePS_3$ for the (d) HER and (e) OER (reproduced with permission from ref. 71 Copyright 2021, Zhengzhou University).

outbound H_2O adsorption behavior on Ni sites of Ni-$FePS_3$ for the HER was disclosed by the differential electron density (Fig. 2c). Fig. 2d depicts the calculated Gibbs free energy profiles and the proposed reaction mechanism for the HER. Ni-$FePS_3$ exhibits lower water adsorption energy (0.11 eV) and lesser water dissociation energy barrier (1.2 eV), suggesting its enhanced HER catalysis. In contrast, $FePS_3$ exhibits higher water adsorption energy (0.43 eV) and a more enormous water dissociation energy barrier (1.92 eV), suggesting its sluggish HER catalysis. The water adsorption/dissociation configurations on Ni-$FePS_3$ suggest that water molecules could be adsorbed on the Ni sites, where the water dissociation could be supported by the nearby S sites having increased electron density. Fig. 2e depicts the calculated Gibbs free energy profiles and the proposed reaction mechanism for the OER. The Ni atoms with charge enrichment in Ni-$FePS_3$ could serve as active sites to more suitably weaken the rate-limiting O* intermediates compared to the P sites in the $FePS_3$. Ni-$FePS_3$ comprises the monoclinic phase of $FePS_3$, anchored by atomically dispersed Ni atoms. The characteristic peak corresponding to Ni–Ni bonding at about 2.48 Å was not observed for Ni-$FePS_3$ from the Ni K-edge EXAFS spectra, suggesting the existence of Ni

predominantly as a single atomic species in Ni-$FePS_3$. The Fe K-edge XANES spectra disclose that the near-edge absorption energy of Ni-$FePS_3$ is higher than that of $FePS_3$ and Fe foil, suggesting that the average electron density around Fe in Ni-$FePS_3$ is less than that of $FePS_3$ and Fe foil. In the high-resolution XPS spectra of S 2p, Ni-$FePS_3$ exhibits a slight negative shift (0.2 eV) when compared to $FePS_3$, suggesting the modified electronic structure after Ni incorporation in $FePS_3$. The projected density of states discloses the formation of some new electronic states for Ni-$FePS_3$ due to the hybridization of Fe 3d, S 2p, and Ni 3d in the bandgap, which could be due to the charge redistribution, suggesting the higher electronic conductivity after Ni incorporation in $FePS_3$. Ni, Fe, P, and S possess nanosheet morphology and are distributed homogeneously. Thus, incorporation of Ni in $FePS_3$ could modify the electronic structure and improve the electronic conductivity, and that could enhance the activity for the HER and OER.

Besides, Yang *et al.*[72] observed that Ni_2P-$Ni_{12}P_5$@Ni_3S_2 exhibits enhanced activity and stability for the HER. It was obtained on cleaned Ni foam by hydrothermal treatment for simultaneous corrosion and sulfidation followed by phosphidation at 370 °C for 2 h under an N_2 atmosphere. Ni_2P-$Ni_{12}P_5$@Ni_3S_2 exhibits higher activity, higher electrochemical surface area, and lower charge transfer resistance for the HER than Ni_2P. It comprises a Ni_2P-$Ni_{12}P_5$ nanorod array, which is rooted in Ni_3S_2 film. It exhibits a heterointerface between Ni_2P and $Ni_{12}P_5$ phases. It exhibits super hydrophilicity with a contact angle of 0°. For the HER in 1 M KOH, it affords an η of -32 mV at -10 mA cm^{-2}, suggesting its very high activity.

Moreover, Paudel *et al.*[73] observed that the 1T Co-WS_2/$NiTe_2$/Ni exhibits enhanced activity and stability for the HER and OER. It was obtained on pretreated Ni foam by a two-step hydrothermal treatment. The 1T Co-WS_2/$NiTe_2$/Ni exhibits higher activity and lower charge transfer resistance for the HER than WS_2/$NiTe_2$/Ni, WS_2/Ni, and 1T $NiTe_2$/Ni. 1T Co-WS_2/$NiTe_2$/Ni exhibits higher activity and electrochemical surface area for the OER than WS_2/$NiTe_2$/Ni, WS_2/Ni, and 1T $NiTe_2$/Ni. It comprises a metallic $NiTe_2$/Ni nanoskeleton as the core and a Co-WS_2 nanosheet layer as the shell. It exhibits a heterointerface between the WS_2 and $NiTe_2$ phases. For the HER in 1 M KOH, it affords an η of -88 mV at -10 mA cm^{-2}, suggesting its very high activity. For overall water splitting in 1 M KOH, the 1T Co-WS_2/$NiTe_2$/Ni//1T Co-WS_2/$NiTe_2$/Ni affords a potential of 1.521 V at 10 mA cm^{-2}, suggesting its high activity.

Fabrication of electrocatalysts with high valence state sites could act as favorable reductive centers for large-current-density water splitting. Li *et al.*[74] proposed that a high valence state of Co^{3+} in the $Ni_{9.5}Co_{0.5}$-S-FeO_x hybrid catalyst can act as a favorable center for a stable and efficient HER compared to the hybrid catalyst with low chemical states. At the same time, it was obtained on Cu foam through a two-step electrodeposition method. For the HER in 1 M KOH at 60 °C, it affords an η of -22 mV at -10 mA cm^{-2} and an η of -175 mV at a current density of -1000 mA cm^{-2}, suggesting its very high activity. For overall water splitting in 1 M KOH at 60 °C, $Ni_{9.5}Co_{0.5}$-S-FeO_x//$Ni_{9.5}Co_{0.5}$-S-FeO_x affords a potential of 1.730 V at a current density of 1000 mA cm^{-2}, suggesting its very high activity, while it exhibits high stability.

Coupling of the suitable transition metal atoms with the nanostructured Chevrel-phase metal sulfides could cause the delocalization of d-electrons, enhance the charge transfer, afford optimal adsorption energies with intermediates, and that could enhance the performance for the HER and OER. Chandrasekaran *et al.*[75] demonstrated that Co/N-$NiMo_3S_4$ exhibits high activity and stability for the HER and OER while it was prepared by hydrothermal treatment. Theoretical and experimental investigation discloses that delocalization of the d-electron on Co/N-$NiMo_3S_4$ can occur due to the coupling of Co atoms with edge Ni atoms, leading to enhancement in charge transfer, which could enhance the performance for overall water electrolysis. Moreover, an upshift in the d-band center of Co/N-$NiMo_3S_4$ can provide optimal adsorption energies for the intermediates for water dissociation and adsorption, enhancing overall water electrolysis. For the HER in 1 M KOH, it affords an η of -78 mV at -10 mA cm^{-2} and an η of -307 mV at a high current density of -1000 mA cm^{-2}, suggesting its very high activity. For the OER in 1 M KOH, it affords an η of 186 mV at 50 mA cm^{-2} and an η of 225 mV at 300 mA cm^{-2}, suggesting its very high activity. For overall water splitting in 1 M KOH, Co/N-$NiMo_3S_4$//Co/N-$NiMo_3S_4$ affords a potential of 1.47 V at 10 mA cm^{-2}, suggesting its very high activity while it exhibits high stability.

2.2.2. Fabricating selenide electrocatalysts. Fabrication of heterostructured transition metal selenide/metal selenide having a nanostructure could modify the electronic structure, provide optimal adsorption energy with intermediates, facilitate the evolution of gas, and that could enhance the performance of the HER and OER. Majumdar *et al.*[76] observed that $MoSe_2$@-$NiCo_2Se_4$ exhibits enhanced activity for the HER and OER. It was obtained on pretreated Ni foam by hydrothermal treatment followed by hydrothermal selenization at 140 °C for 2 h. $MoSe_2$@$NiCo_2Se_4$ exhibits higher activity and lower charge transfer resistance for the HER and OER than MoO_3/Ni-$Co(OH)_2$. It is a $MoSe_2$@$NiCo_2Se_4$ heterostructure. It possesses a nanosheet on nanosheet structure. For the HER in 1 M KOH, it affords an η of -89 mV at -10 mA cm^{-2}, suggesting its very high activity.

Fabrication of transition bimetallic doped selenides could modify the electronic structure and provide optimal adsorption energy with intermediates, enhancing the performance for the HER and OER. Ibraheem *et al.*[77] observed that Fe@Co/Se_2 exhibits enhanced activity and stability for the HER and OER. It was obtained by hydrothermal treatment. Fe@Co/Se_2 exhibits higher activity and lower charge transfer resistance for the HER and OER than Fe-Se_2 and Co-Se_2. It is crystalline, containing an Fe, Co dual doped selenide. It contains Co, Fe, and Se, which are homogeneously distributed. In the high-resolution XPS spectra, the Fe 2p peak of Fe@Co/Se_2 exhibits a slight positive shift when compared to that of Fe-Se_2. In contrast, the Co 2p peak of Fe@Co/Se_2 exhibits a slight negative shift when compared to

that of Co-Se_2, suggesting a modified electronic structure, possibly due to the partial transfer of electrons from the Fe to Co, which could be due to the higher electronegativity of Co, when compared to that of Fe. It contains $Fe^{2+/3+}/Co^{2+}$ species, which are coupled to selenide utilizing an Fe-coordinated Co-bridged bond. It possesses nanorod morphology. For the OER in 1 M KOH, it affords an η of 200 mV at 10 mA cm^{-2}, suggesting its very high activity. For the HER in 1 M KOH, it affords an η of -78 mV at -10 mA cm^{-2}, suggesting its very high activity. For overall water splitting in 1 M KOH, Fe@Co/Se_2//Fe@Co/Se_2 affords a potential of 1.51 V at 10 mA cm^{-2}, suggesting its very high activity.

Fabrication of nanostructured tungsten incorporated CoSe/Co_3O_4 could modify the electronic structure, afford optimal adsorption energy with intermediates, facilitate the gas evolution, and expose abundant active sites, and that could enhance the activity and stability for the HER and OER. Balaji *et al.*[78] observed that WCoSe/WCo_3O_4 exhibits very high activity and stability for the HER and OER. It was synthesized on Ni foam by hydrothermal treatment at ~160 °C for 16 h followed by selenization at ~180 °C for 4 h followed by calcination at 300 °C for 2 h in an air atmosphere. WCoSe/WCo_3O_4 exhibits higher activity and electrochemical surface area for the HER and OER than WSe_2/WO_2 and CoSe/Co_3O_4. It possesses a nanosheet-like structure having nanopores (Fig. 3a). It is polycrystalline (Fig. 3b). It contains WSe_2, WO_2, CoSe, and Co_3O_4 phases, while it exhibits heterointerfaces (Fig. 3c). It exhibits a high crystalline structure (Fig. 3d). It contains W, Co, Se, and O (Fig. 3e). In the XPS spectra, the W 4f peak for WCoSe/WCo_3O_4 is slightly shifted towards higher binding energy when compared to that of WSe_2/WO_2, suggesting a modified electronic structure. For the OER in 1 M KOH, it affords an η of 175 mV at 10 mA cm^{-2}, suggesting its very high activity. For the HER in 1 M KOH, it affords an η of -98 mV at -10 mA cm^{-2}, suggesting its very high activity. For overall water splitting in 1 M KOH, WCoSe/WCo_3O_4//WCoSe/WCo_3O_4 affords a potential of 1.49 V at 10 mA cm^{-2}, suggesting its very high activity. In contrast, it affords reasonable stability at 100 mA cm^{-2} for 100 h, suggesting its high stability.

Selenization of stainless steel followed by heat treatment followed by electrochemical oxidation could create abundant oxygen vacancies, increase the Ni content, and that could enhance the performance of the OER. Han *et al.*[79] observed that

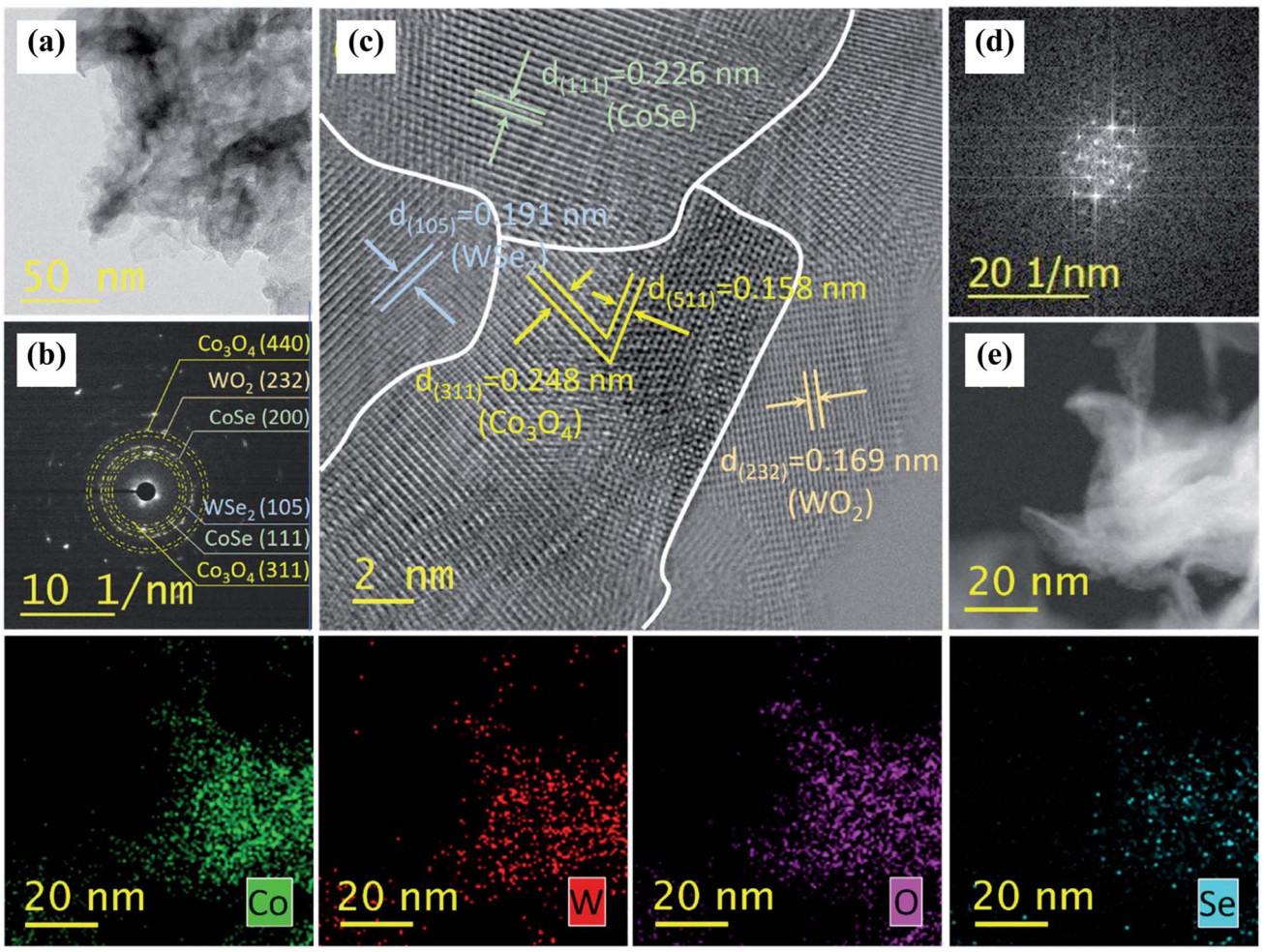

Fig. 3 Characterization of the WCoSe/WCo_3O_4 heterostructure: (a) TEM image; (b) SAED pattern; (c) HRTEM image; (d) FFT pattern; (e) STEM image and its corresponding EDS elemental mapping (reproduced with permission from ref. 78 Copyright 2022, The Royal Society of Chemistry).

SS-500-AO exhibits enhanced activity and stability for the OER. SS-500-AO is an electrocatalyst on SUS304 stainless steel, where the catalyst was prepared by selenization followed by heat treatment followed by electrochemical oxidation. It contains abundant oxygen vacancies (76.09%). It contains 51.18% of Ni^{3+}, 12.72% of Ni^{2+}, and 36.1% of metallic Ni. For the OER in 1 M KOH, it affords an η of 284.3 mV at 10 mA cm^{-2}, suggesting its very high activity, while it undergoes negligible decay at 10 mA cm^{-2} for 160 h, suggesting its very high stability.

Fabrication of composites containing transition metal selenides and perovskite oxides could enhance the performance of the HER and OER. Kim *et al.*[9] observed that LSCO-$MoSe_2$ exhibits enhanced activity for the HER and OER, where LSCO is $La_{0.5}Sr_{0.5}CoO_{3-\delta}$ perovskite oxide. It was prepared by a sol–gel process followed by calcination followed by ball milling. Fabrication of composites containing transition metal selenides, N-doped graphene quantum dots, and perovskite oxides could modify the electronic structure, afford optimal adsorption energy with intermediates, enhance the conductivity, and that could enhance the performance for the HER and OER. Cao *et al.*[80] observed that LSC-N-GQDs-$MoSe_2$ exhibits enhanced activity and stability for the HER and OER (LSC: $La_{0.5}Sr_{0.5}CoO_{3-\delta}$; N-GQDs: N-doped graphene quantum dots). It is a composite containing a thin layer of N-GQDs (thickness: 2 to 3 nm) at the interface of LSC and $MoSe_2$. In the high-resolution XPS spectra, the La 3d and Co 2p peaks of LSC-N-GQDs-$MoSe_2$ exhibit a slight positive shift when compared to that of LSC, suggesting a modified electronic structure. LSC-N-GQDs-$MoSe_2$ exhibits higher activity and lower charge transfer resistance for the HER and OER than LSC-$MoSe_2$. For overall water splitting in 1 M KOH, LSC-N-GQDs-$MoSe_2$//LSC-N-GQDs-$MoSe_2$ affords a potential of ~1.57 V at 10 mA cm^{-2}, suggesting its very high activity, while it undergoes negligible decay at 500 mA cm^{-2} for 24 h, suggesting its very high stability. The following steps were used in its preparation: at first, N-GQDs were obtained by hydrothermal treatment, and the LSC was synthesized by a sol–gel process followed by calcination. Then, LSC-N-GQDs were obtained by sonication of the LSC and N-GQDs. Later, $MoSe_2$ was obtained by ball milling. Finally, LSC-N-GQDs-$MoSe_2$ was prepared by ball milling the LSC-N-GQDs and $MoSe_2$.

Ion irradiation could activate the inert basal plane of $MoSe_2$, and that could enhance the performance of the HER. Huang *et al.*[81] demonstrated that the activity of $MoSe_2$ nanosheet arrays was activated by He^+ ion irradiation, which could generate multiple vacancies in the inert basal planes. DFT studies disclose that the increase in electrical conductivity and reduction in energy barriers for water dissociation and subsequent proton adsorption can be due to the existence of single Mo and single Se vacancies on the basal plane of $MoSe_2$, which could enhance HER performance. For the HER in 1 M KOH, it affords an η of −90 mV at −10 mA cm^{-2}, suggesting its very high activity, while it exhibits high stability at a current density of 1000 mA cm^{-2}.

2.3. Fabricating metal phosphide/phosphate electrocatalysts

Fabrication of nickel phosphide nanoarrays with a superaerophobic surface could facilitate the gas evolution, expose abundant active sites, enhance the conductivity, and that could enhance the performance for the HER. Yu *et al.*[82] observed that Ni_2P exhibits enhanced activity and stability for the HER. It was prepared by two-step hydrothermal treatment followed by phosphorization at 300 °C for 30 min under Ar atmosphere. The Ni_2P exhibits higher activity, higher electrochemical surface area, and lower charge transfer resistance for the HER than $Ni(OH)_2$. It is hexagonal Ni_2P. It contains Ni and P, which are homogeneously distributed. It possesses nanoarray morphology. It exhibits a superaerophobic surface, which could facilitate the evolution of gas. For the HER in 1 M KOH, it affords an η of −37 mV at −10 mA cm^{-2} and an η of −306 mV at current density of −1000 mA cm^{-2}, suggesting its very high activity, and it undergoes negligible decay at −1200 mA cm^{-2} after 5000 cycles of CV, suggesting its high durability. For overall water splitting in 1 M KOH, the NiFe LDH^{OER}//Ni_2P^{HER} affords a potential of ~2.05 V at a current density of 1000 mA cm^{-2}, suggesting its very high activity.

Fabrication of transition bimetallic phosphides could modify the electronic structure, afford optimal adsorption energy with intermediates, and enhance the performance of the HER and OER. Zhao *et al.*[83] observed that NiCoP exhibits enhanced activity and stability for the HER and OER. It was synthesized by ultrasonic agitation followed by phosphorization at 350 °C for 3 h. NiCoP exhibits higher activity, higher electrochemical surface area, and lower charge transfer resistance for the HER and OER than CoP. It is quasi-monolayered Ni5% CoP. It contains Ni, Co, and P, which are homogeneously distributed. In the high-resolution XPS spectra, the P 2p peaks of NiCoP exhibit a slight negative shift compared to that of CoP, suggesting a modified electronic structure. It possesses a 2D sub-nanostructure. It contains abundant mesopores. For the OER in 1 M KOH, it affords an η of 259 mV at 10 mA cm^{-2}, suggesting its very high activity, and it undergoes negligible decay at 90 mA cm^{-2} after 10 000 cycles of CV, suggesting its high durability. For the HER in 1 M KOH, it affords an η of −84 mV at −10 mA cm^{-2}, suggesting its very high activity, and it undergoes slight decay at −140 mA cm^{-2} after 10 000 cycles of CV, suggesting its high durability. For overall water splitting in 1 M KOH, the NiCoP//NiCoP affords a potential of 1.48 V at 10 mA cm^{-2}, suggesting its very high activity. Moreover, Song *et al.*[84] observed that CoNiP exhibits enhanced activity for the HER and OER. It was prepared by ion exchange/etching of ZIF-67 (Co-based zeolitic imidazolate frameworks) followed by phosphidation. CoNiP exhibits higher activity for the HER and OER than that of CoNi LDH. It is crystalline, containing nanostructured CoNiP. It contains Ni, Co, P, and C, which are homogeneously distributed. In the high-resolution XPS spectra, the Ni 2p and Co 2p peaks of CoNiP exhibit a slight shift compared to that of CoNi LDH, suggesting a modified electronic structure.

Nanostructured Fe-doped CoP can be prepared by the phosphorization of a bimetallic Prussian blue analog, and that could facilitate the evolution of gas, enhance the conductivity, which could enhance the performance for the HER and OER. Cao *et al.*[85] observed that the Fe-CoP exhibits enhanced activity and stability for the HER and OER. It was obtained on pre-treated Ni foam by co-precipitation followed by phosphorization at 400 °C for 3 h under an N_2 atmosphere. Fe-CoP exhibits higher activity and lower charge transfer resistance for the HER and OER than $CoFe_2O_4$. It is Fe-doped CoP. It contains Fe, Co, P, O, and C, which are homogeneously distributed. It possesses a hierarchical nanoporous structure, where the crystalline nanoparticles are embedded in amorphous carbon layers. It possesses a high specific surface area of 177 $m^2 g^{-1}$. It contains mesopores and macropores. For the OER in 1 M KOH, it affords an η of 190 mV at 10 mA cm^{-2} and an η of 428 mV at a current density of 1000 mA cm^{-2}, suggesting its very high activity, while it undergoes negligible decay at 1000 mA cm^{-2} for 30 h, suggesting its very high stability. For the HER in 1 M KOH, it affords an η of −78 mV at −10 mA cm^{-2}, suggesting its very high activity. For overall water splitting in 1 M KOH, Fe-CoP//Fe-CoP affords a potential of 1.49 V at 10 mA cm^{-2}, suggesting its very high activity.

Fabrication of the nanostructured trimetallic MnNiCo phosphide could modify the electronic structure, provide optimal adsorption energy with intermediates, facilitate the evolution of gas, enhance the conductivity, expose abundant active sites, and that could enhance the performance for the HER and OER. Salem *et al.*[10] observed that $Mn_1Ni_1Co_1$-P exhibits enhanced activity and stability for the HER and OER. It was obtained on Ni foam by electrodeposition followed by plasma phosphidation at 250 °C for 3 h under a PH_3/Ar atmosphere. $Mn_1Ni_1Co_1$-P exhibits higher activity, higher electrochemical surface area, and lower charge transfer resistance for the HER and OER than MnNiCo-OH. It is trimetallic $Mn_1Ni_1Co_1$-P, containing hexagonal NiCoP. It contains Ni, Mn, Co, and P, which are homogeneously distributed. In the high-resolution XPS spectra, the P 2p peak of $Mn_1Ni_1Co_1$-P exhibits a slight negative shift when compared to that of phosphorus, suggesting a modified electronic structure possibly due to the strong interaction between the metals and the P atom. It possesses an interconnected nanosheet structure. For the OER in 1 M KOH, it affords an η of 289 mV at 10 mA cm^{-2}, suggesting its very high activity, and it undergoes negligible decay at 10 mA cm^{-2} after 5000 cycles of CV, suggesting its high durability. For the HER in 1 M KOH, it affords an η of −14 mV at −10 mA cm^{-2}, suggesting its substantially very high activity, and it undergoes negligible decay at −10 mA cm^{-2} after 5000 cycles of CV, suggesting its high durability. For overall water splitting in 1 M KOH, $Mn_1Ni_1Co_1$-P//$Mn_1Ni_1Co_1$-P affords a potential of 1.48 V at 10 mA cm^{-2}, suggesting its very high activity.

Besides, Wu *et al.*[19] observed that Ni_2P-Fe_2P exhibits enhanced activity and stability for the HER and OER. The following steps were employed to obtain it. At first, $Ni(OH)_2$ was prepared on cleaned Ni foam by the etching growth method at room temperature. Then, $Ni(OH)_2$ was converted into $(Ni,Fe)(OH)_2$ by an ion-exchange process at room temperature. Finally, $(Ni,Fe)(OH)_2$ was converted into Ni_2P-Fe_2P by phosphidation at 450 °C for 1.5 h under an Ar atmosphere. Ni_2P-Fe_2P exhibits higher activity, higher electrochemical surface area, and lower charge transfer resistance for the HER and OER than $Ni(OH)_2$ and Ni_2P-Ni_5P_4. It is crystalline, containing Ni_2P and Fe_2P phases. It exhibits a heterostructure. It contains Fe, Ni, and P, which are homogeneously distributed. It possesses microsheet morphology having a thickness of about 7.4 nm. For the OER in 1 M KOH, it affords an η of 218 mV at 10 mA cm^{-2} and an η of 337 mV at a current density of 1000 mA cm^{-2}, suggesting its very high activity, and it undergoes negligible decay at 1000 mA cm^{-2} after 3000 cycles of CV, suggesting its high durability. For the HER in 1 M KOH, it affords an η of −128 mV at −10 mA cm^{-2} and an η of −333 mV at a current density of −1000 mA cm^{-2}, suggesting its very high activity, and it undergoes negligible decay at −1000 mA cm^{-2} after 3000 cycles of CV, suggesting its high durability. For overall water splitting in 1 M KOH, Ni_2P-Fe_2P//Ni_2P-Fe_2P affords a potential of 1.561 V at 10 mA cm^{-2} and ∼1.98 V at a current density of 1000 mA cm^{-2}, suggesting its very high activity.

Moreover, Yu *et al.*[18] observed that FeP/Ni_2P exhibits significantly very high activity and stability for the HER and OER. It was prepared on Ni foam by a two-step phosphidation process. FeP/Ni_2P exhibits higher activity and electrochemical surface area for the HER than Ni_2P*, while it exhibits higher activity and electrochemical surface area for the OER than Ni_2P. It exhibits lower charge transfer resistance than Ni_2P for the HER and OER. FeP/Ni_2P possesses mesopores and/or nanopores (Fig. 4a and b). It possesses nanoparticle morphology. It is crystalline and contains FeP and Ni_2P phases (Fig. 4c, d and g). It contains Ni, Fe, and P, which are homogeneously distributed (Fig. 4e). It is a metal phosphide (Fig. 4f). Thus, the nanostructured transition hybrid metal phosphides with pores on 3D Ni foam could modify the electronic structure, provide optimal adsorption energy with intermediates, enhance the conductivity, facilitate the gas evolution, and expose abundant active sites, and that could enhance the activity and stability for the HER and OER. For the OER in 1 M KOH, it affords an η of 154 mV at 10 mA cm^{-2} and an η of 293 mV at a current density of 1000 mA cm^{-2}, suggesting its outstanding activity, while it undergoes negligible decay at a current density of 1500 mA cm^{-2} after 5000 cycles of CV, suggesting its outstanding durability. For the HER in 1 M KOH, it affords an η of −14 mV at −10 mA cm^{-2} and an η of ∼−270 mV at a current density of −1000 mA cm^{-2}, suggesting its outstanding activity, while it undergoes negligible decay at −1000 mA cm^{-2} after 5000 cycles of CV, suggesting its outstanding durability. For overall water splitting in 1 M KOH, FeP/Ni_2P//FeP/Ni_2P affords a potential of 1.42 V at 10 mA cm^{-2} and a potential of ∼1.78 V at a current density of 1000 mA cm^{-2} (Fig. 4h), suggesting its outstanding activity, while it undergoes negligible decay at 500 mA cm^{-2} for >40 h (Fig. 4i), suggesting its very high stability.

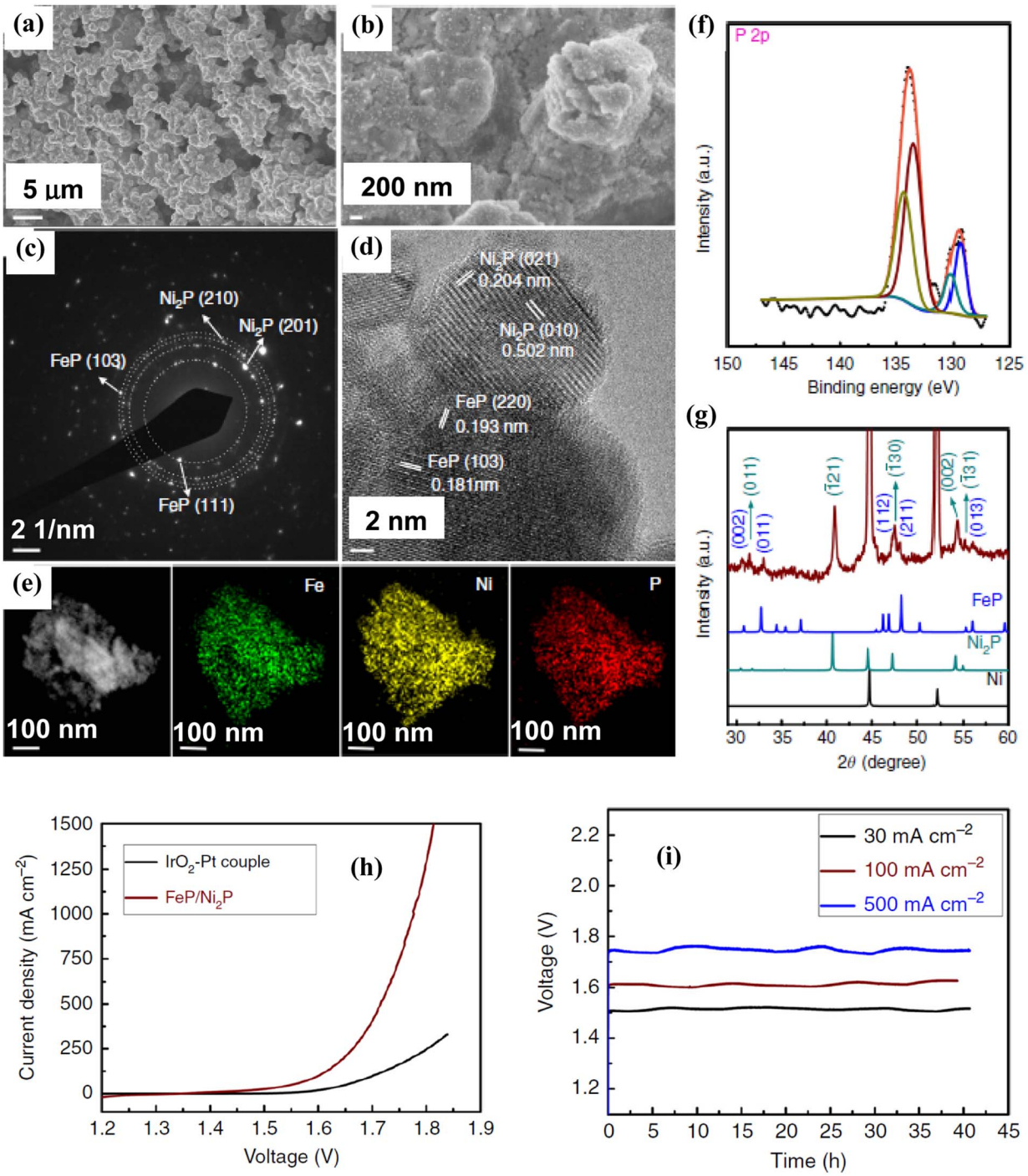

Fig. 4 Characterization of FeP/Ni_2P: (a) and (b) SEM images; (c) SAED pattern; (d) HRTEM image; (e) TEM image and its corresponding EDX elemental mapping; (f) XPS spectrum; (g) XRD pattern; (h) LSV curves of FeP/Ni_2P//FeP/Ni_2P in comparison with IrO_2//Pt for overall water splitting in 1 M KOH; (i) chronopotentiometric curves of FeP/Ni_2P at 30, 100, and 500 mA cm^{-2} in 1 M KOH (reproduced with permission from ref. 18 Copyright 2018, Nature Publishing Group).

In addition, Yu *et al.*[86] observed that $Ni_{2(1-x)}Mo_{2x}P$ exhibits enhanced activity and stability for the HER. It was prepared on pretreated Ni foam by hydrothermal treatment followed by phosphorization at 500 °C for 1 h under an Ar atmosphere. $Ni_{2(1-x)}Mo_{2x}P$ exhibits higher activity, higher electrochemical surface area, and lower charge transfer resistance for the HER than Ni_2P and $NiMoO_4$. The XRD patterns show the prominent peaks for Ni_2P and a tiny peak for the $NiMoO_4$ precursor. It contains Mo, Ni, and P, which are homogeneously distributed. In the high-resolution XPS spectra, the Ni 2p peak of

$Ni_{2(1-x)}Mo_{2x}P$ exhibits a slight negative shift when compared to that of Ni_2P, suggesting the modified electronic structure. It possesses highly porous nanowire array morphology. For the HER in 1 M KOH, it affords an η of -72 mV at -10 mA cm^{-2} and an η of -294 mV at a current density of -1000 mA cm^{-2}, suggesting its very high activity, while it affords reasonable stability for 160 h, suggesting its very high stability, and it undergoes negligible decay at -700 mA cm^{-2} after 5000 cycles of CV, suggesting its high durability.

Besides, Yuan *et al.*[87] observed that S-Co_2P@Ni_2P exhibits enhanced activity and stability for the HER and OER. It was synthesized on cleaned Ti mesh by hydrothermal treatment followed by an ion-exchange process followed by a chemical deposition method followed by phosphidation at 320 °C for 2 h under an Ar atmosphere. S-Co_2P@Ni_2P exhibits higher activity for the HER and OER than Co_2P@Ni_2P. It is a S-doped Co_2P@Ni_2P heterostructure, where the Co_2P nanowire is the core, and the Ni_2P nanosheets are the shell. It exhibits a heterointerface between the Co_2P and Ni_2P phases. In the high-resolution XPS spectra, the Ni 2p and Co 2p peaks of S-Co_2P@Ni_2P exhibit slight shift when compared to that of Co_2P@Ni_2P, suggesting a modified electronic structure possibly due to the partial transfer of electrons from Co_2P to Ni_2P after S doping, which could be due to the higher electronegativity of Ni, when compared to that of Co. From the ultraviolet photoelectron spectroscopy, the value of the work function for S-Co_2P is 4.03 eV, which is lower than that of 4.78 eV for Ni_2P, suggesting the existence of a heterostructure, which could cause interfacial electron redistribution till the work functions reach equilibrium on both sides. For the OER in 1 M KOH, it undergoes negligible decay at 600 mA cm^{-2} after 1000 cycles of CV, suggesting its high durability. For the HER in 1 M KOH, it affords an η of -43 mV at -10 mA cm^{-2}, suggesting its very high activity, and it undergoes negligible decay at -700 mA cm^{-2} after 1000 cycles of CV, suggesting its high durability. For overall water splitting in 1 M KOH, S-Co_2P@Ni_2P//S-Co_2P@Ni_2P affords a potential of 1.52 V at 10 mA cm^{-2}, suggesting its very high activity.

Active sites of nickel phosphide can be tuned by pulse-reverse electrodeposition, which could enhance the performance of the HER and OER. Kim *et al.*[88] observed that the NiP film exhibits enhanced activity and stability for the HER and OER. It was prepared by pulse-reverse electrodeposition, where the dissolution step can modulate the chemical states of P in the NiP film. The enhanced activity for the HER of NiP film can be achieved by enhancing the generation of Ni_xP by inhibiting the oxidation of P to PO_x^- in the pulse-reverse electrodeposition, the dissolution step should be as minimal as possible. On the other hand, the enhanced activity for the OER of the NiP film can be achieved by increasing the dissolution amount in the pulse-reverse electrodeposition.

Phosphorus doping can play a crucial role in the formation of a nanoporous surface, where the nanoporous surface can be formed by the electrochemical etching of a phosphorus-doped alloy, which could expose abundant active sites and that could improve the performance of the HER and OER. Feng *et al.*[89] observed that e-FeCoNiCu-P exhibits enhanced activity and stability for the HER and OER, where e-FeCoNiCu-P is electrochemically etched FeCoNiCu-P. The following steps were involved in its preparation: first, FeCoNiCu foil as a medium entropy alloy was obtained by the arc melting process. Then, FeCoNiCu-P was obtained by phosphidation of the pretreated FeCoNiCu foil. Finally, e-FeCoNiCu-P was prepared by electrochemical etching of FeCoNiCu-P. e-FeCoNiCu-P exhibits higher activity for the HER and OER than FeCoNiCu-P. It possesses a nanoporous surface, which could expose abundant active sites and enhance the performance of the HER and OER.

Besides, Li *et al.*[90] observed that Ni_5P_4@FeP exhibits enhanced activity and stability for the OER. It was obtained on Ni foam by immersion for about 5 s (corrosion process) followed by phosphorization at 350 °C for 1 h under an N_2 atmosphere. Ni_5P_4@FeP exhibits higher activity and lower charge transfer resistance for the OER than Ni_5P_4 and FeP. It is crystalline, while it exhibits a heterointerface between Ni_5P_4 and FeP phases. It possesses nanosheet array morphology. It is reconstructed into $NiFe_2O_4$ during the OER at low oxidation potentials, while $NiFe_2O_4$ is partially reconstructed into Ni/FeOOH at large oxidation potentials. Thus, Ni_5P_4@FeP is reconstructed into Ni/FeOOH@$NiFe_2O_4$ during the OER, where this genuinely active species has high structural reversibility. For the OER in 1 M KOH, it affords an η of 205 mV at 10 mA cm^{-2}, suggesting its very high activity. In contrast, it undergoes negligible decay at 100 mA cm^{-2} for 100 h, suggesting its very high stability.

Fabricating nanostructured phosphide-based electrocatalysts using relatively low-cost metals such as Fe, Mn, and Zn is highly desirable for green synthesis, which could modify the electronic structure, provide optimal adsorption energy with intermediates, facilitate the gas evolution, and that could enhance the performance for the HER and OER. Huang *et al.*[28] observed that Zn-Fe/Mn@Mn-FeP exhibits enhanced activity and stability for the HER and OER. It was prepared by the etching of $Fe_{70}Mn_{28}Zn_2$ for 1 h followed by annealing at 400 °C for 1 h in air followed by etching for 1 h followed by phosphorization at 500 °C for 3 h in an Ar atmosphere. Zn-Fe/Mn@Mn-FeP exhibits higher activity and electrochemical surface area for the HER than Fe/Mn@Mn-FeP, Zn-Fe@Zn-FeP, and Fe@FeP. Zn-Fe/Mn@Mn-FeP exhibits higher activity for the OER than Fe/Mn@Mn-FeP, Zn-Fe@Zn-FeP, and Fe@FeP. It is Zn-Fe/Mn@Mn-FeP. It contains orthorhombic FeP, cubic Fe, and Mn, where the Zn phase is not observed, possibly due to its low content. It contains an Mn–P bond. In the high-resolution XPS spectra, the Fe 2p peak of Zn-Fe/Mn@Mn-FeP exhibits a slight positive shift when compared to that of metallic Fe, and the Mn 2p peak of Zn-Fe/Mn@Mn-FeP exhibits a slight positive shift, when compared to that of metallic Mn, suggesting a modified electronic structure. It contains Mn, Zn, Fe, and P, which are homogeneously distributed. It possesses ultrathin nanosheet morphology. For the HER in 1 M KOH, it affords an η of

−165 mV at −10 mA cm^{-2}, suggesting its very high activity. S-doped NiFeP can be derived from the phosphorization of MOF, and that could modify the electronic structure, provide optimal adsorption energy with intermediates, downshift the d-band center from the Fermi level, which could enhance the performance for the HER and OER. Li *et al.*[91] observed that S-NiFeP-20 exhibits enhanced activity and stability for the HER, while S-NiFeP-10 exhibits enhanced activity and stability for the OER. S-NiFeP-20 or S-NiFeP-10 was prepared on pretreated carbon cloth by hydrothermal treatment (for MOF preparation) followed by phosphorization at 300 °C for 2 h under an Ar atmosphere. It is S-doped NiFeP. In the high-resolution XPS spectra, the Fe 2p peak of S-NiFeP exhibits a slight positive shift compared to NiFeP, suggesting a modified electronic structure due to S doping. The DFT calculations disclose that the S doping in NiFeP plays a crucial role in the formation of optimal ΔG values for the formation of intermediates on Ni atoms, and that enhances the performance of the OER. S-NiFeP-20 downshifts the d-band center from the Fermi level, and that enhances the performance for the HER. In 1 M KOH, S-NiFeP-20 affords an η of −56 mV at −10 mA cm^{-2} for the HER, while S-NiFeP-10 affords an η of 201 mV at 10 mA cm^{-2} for the OER, suggesting their very high activity. For overall water splitting in 1 M KOH, S-NiFeP-10^{OER}//S-NiFeP-20^{HER} affords a potential of 1.5 V at 10 mA cm^{-2}, suggesting its very high activity.

Besides, Kumar *et al.*[13] observed that the NiP_2-FeP_2@Cu nanoarray exhibits enhanced activity and stability for the HER. The following steps were involved in its preparation: at first, a Cu nanoarray was grown on pretreated Cu foam by chemical oxidation followed by calcination followed by electrochemical reduction. Then, NiFe LDH was grown on the Cu nanoarray by electrodeposition. Finally, the NiP_2-FeP_2@Cu nanoarray was obtained by the phosphidation of the NiFe LDH@Cu nanoarray at 350 °C for 2 h under an Ar atmosphere. The NiP_2-FeP_2@Cu nanoarray on Cu foam exhibits higher activity, higher electrochemical surface area, and lower charge transfer resistance for the HER than NiP_2-FeP_2 on carbon fiber paper. It is NiP_2-FeP_2 on a Cu nanoarray. It exhibits heterointerfaces between NiP_2 and FeP_2 phases. It contains Ni, Fe, P, and Cu, which are homogeneously distributed. The high-resolution XPS spectra of Cu 2p for the NiP_2-FeP_2@Cu nanoarray obtained before and after Ar etching disclose the existence of Cu^0 along with a small peak, where the small peak is attributed to $Cu^{\delta+}$, which could be due to the coupling between NiP_2-FeP_2 and the Cu nanoarray. For the HER in 1 M KOH, it affords an η of −23.6 mV at −10 mA cm^{-2} and an η of −357 mV at a current density of −1000 mA cm^{-2}, suggesting its substantially very high activity, while it affords reasonable stability at −1000 mA cm^{-2} for 50 h, suggesting its very high stability.

Moreover, Zhang *et al.*[92] observed that Ni_2P/NC exhibits enhanced activity and stability for the HER. It was synthesized by a coordination reaction followed by calcination followed by phosphorization followed by etching. Ni_2P/NC exhibits higher activity for the HER than Ni_2P. It is composed of nickel phosphide nanoparticles, which are anchored on N-doped porous carbon nanorods. It contains N, C, Ni, and P, which are homogeneously distributed. In the high-resolution XPS spectra, the Ni 2p peak of Ni_2P/NC exhibits a slight positive shift compared to that of Ni_2P, suggesting a modified electronic structure, possibly due to the partial transfer of electrons between Ni_2P and NC. It possesses nanorod morphology, having abundant mesopores.

In addition, Liu *et al.*[93] observed that NiCoFe-P/C exhibits enhanced activity and stability for the HER and OER. It was synthesized on pretreated Ni foam by hydrothermal treatment followed by carbonization at 450 °C for 2 h in N_2 followed by phosphorization at 350 °C for 2 h in N_2. NiCoFe-P/C exhibits higher activity and electrochemical surface area for the HER than NiCoFe-ZIF and NiCoFe-C. NiCoFe-P/C exhibits higher activity for the OER than NiCoFe-ZIF and NiCoFe-C. It is composed of 0D NiCoFe-P quantum dots, which are anchored on 2D porous carbon, where NiCoFe-P comprises Ni_2P, CoP, and Fe_2P phases. It exhibits heterointerfaces. In the high-resolution XPS spectra, the Ni 2p peak of NiCoFe-P/C is slightly less than that of Ni^{2+}, suggesting a modified electronic structure. For the HER in 1 M KOH, it affords an η of −87 mV at −10 mA cm^{-2}, suggesting its very high activity. For overall water splitting in 1 M KOH, NiCoFe-P/C//NiCoFe-P/C affords a potential of 1.55 V at 10 mA cm^{-2}, suggesting its very high activity. The surface properties of the materials can be improved by plasma treatment.[94] Fabrication of Co-Nb bimetallic phosphide on plasma-modified carbon cloth could modify the electronic structure, provide optimal adsorption energy with intermediates, enhance the conductivity, and that could enhance the performance for the HER. Xiang *et al.*[95] observed that CoP_3-Nb_2P/PCC exhibits enhanced activity and stability for the HER (PCC: plasma modified carbon cloth). The following steps were involved in its preparation: first, plasma-modified carbon-cloth was obtained by dielectric barrier discharge atmospheric pressure plasma treatment on cleaned carbon cloth. Then, the CoO-NbO/PCC was prepared by hydrothermal treatment. Finally, CoP_3-Nb_2P/PCC was obtained by phosphorization at 550 °C for 2 h in N_2. CoP_3-Nb_2P/PCC exhibits higher activity, higher electrochemical surface area, and lower charge transfer resistance for the HER than CoO-NbO/PCC. It comprises the cubic phase of CoP_3 and the orthorhombic phase of Nb_2P on plasma-modified carbon cloth. It contains Nb, Co, and P, which are homogeneously distributed. It possesses drum-like morphology. DFT calculations and *in situ* Raman spectra results disclose that the enhanced performance for the HER of CoP_3-Nb_2P/PCC is attributed to the synergistic effect between Nb and Co phosphide. For the HER in 1 M KOH, it affords an η of −111 mV at −10 mA cm^{-2} and an η of −375 mV at a current density of −1000 mA cm^{-2}, suggesting its very high activity, and it affords undergoes negligible decay at −500 mA cm^{-2} after 5000 cycles of CV, suggesting its high durability.

Besides, Bai *et al.*[6e] observed that Fe_2P/Co@NPC exhibits enhanced activity and stability for the HER and OER. It was

synthesized by hydrothermal treatment followed by carbonization at 950 °C for 3 h under an Ar atmosphere. Fe_2P/Co@NPC exhibits higher activity and lower charge transfer resistance for the HER and OER than Co@NC and Fe_2P@NPC. It is composed of Fe_2P and Co nanoparticles, which are embedded in P and N-incorporated porous carbon. It contains Fe, Co, C, N, and P, which are homogeneously distributed. It contains pyridinic N, pyrrolic N, and graphitic N. It contains micropores and mesopores. It exhibits a high specific surface area of 547 $m^2 g^{-1}$.

Moreover, Singh *et al.*[96] observed that NiP_2/NbP@CNTs exhibit enhanced activity and stability for the HER and OER (CNTs: carbon nanotubes). It was obtained on Ni foam by electrodeposition followed by chemical vapor deposition followed by hydrothermal treatment followed by phosphorization at 300 °C for 2 h under an Ar atmosphere. NiP_2/NbP@CNTs exhibit higher activity and electrochemical surface area for the HER and OER than NbP@CNTs and NiP_2@CNTs. It comprises carbon nanotubes as the core and NiP_2/NbP nanosheets as the shell, while it also contains a small amount of Nb_2Ni_9P phase. It exhibits a heterointerface between the NbP and NiP_2 phases. In the high-resolution XPS spectra, the Ni 2p peak of NiP_2/NbP@CNTs exhibits a slight negative shift when compared to that of NiP_2@CNTs, the Nb 3d peak of NiP_2/NbP@CNTs exhibits a slight positive shift, when compared to that of pure NbP, suggesting a modified electronic structure, possibly due to the partial transfer of electrons from Ni to Nb, which could be due to the higher electronegativity of Ni, when compared to that of Nb. For overall water splitting in 1 M KOH, NiP_2/NbP@CNTs//NiP_2/NbP@CNTs affords a potential of 1.51 V at 10 mA cm^{-2}, suggesting its very high activity.

In addition, Chu *et al.*[97] observed that Ni-CoP/Co_2P@NC exhibits enhanced activity and stability for the HER, while the activated Ni-CoP/Co_2P@NC exhibits enhanced activity and stability for the OER. Ni-CoP/Co_2P@NC was prepared by epitaxial growth followed by pyrolysis. The activated Ni-CoP/Co_2P@NC was obtained by electrochemical activation of Ni-CoP/Co_2P@NC, where the activation forms the thin cobalt oxyhydroxide layer as the active species for the OER on the surface of Ni-CoP/Co_2P@NC. Ni-CoP/Co_2P@NC exhibits higher activity and lower charge transfer resistance for the HER than CoP/Co_2P@NC. In comparison, the activated Ni-CoP/Co_2P@NC exhibits higher activity and lower charge transfer resistance for the OER than Ni-CoP/Co_2P@NC and CoP/Co_2P@NC. Ni-CoP/Co_2P@NC exhibits numerous interfaces along with defects between the 2D nanosheets and 3D nanoparticles. It contains Co_2P and CoP phases. Graphitized carbon layers cover the cobalt phosphides. In the high-resolution XPS spectra, the Co 2p peak of Ni-CoP/Co_2P@NC exhibits a slight negative shift compared to that of CoP/Co_2P@NC, suggesting a modified electronic structure. It contains Ni, Co, C, P, O, and N, which are homogeneously distributed. For overall water splitting in 1 M KOH, the activated-Ni-CoP/Co_2P@NC^{OER}//Ni-CoP/Co_2P@NC^{HER} affords a potential of 1.59 V at 10 mA cm^{-2}, suggesting its very high activity. In contrast, it undergoes negligible decay at 1.6 V for 400 h, suggesting its very high stability.

Besides, Riyajuddin *et al.*[12] observed that Gr-CNTs-Sn_4P_3 exhibit enhanced activity and stability for overall water splitting (Gr: graphene; CNTs: carbon nanotubes). It was prepared on pretreated Ni foam by thermal chemical vapor deposition followed by immersion in ferric nitrate solution for 12 h followed by thermal chemical vapor deposition followed by electrochemical deposition followed by phosphorization through solvothermal treatment followed by acid treatment. Gr-CNTs-Sn_4P_3 exhibits higher activity for the OER than Gr-CNTs. It is composed of Sn_4P_3 with a rhombohedral structure, which is grown on a carbon matrix, where the carbon matrix is composed of graphene and multi-walled carbon nanotubes. It exhibits a heterojunction interface between CNTs and Sn_4P_3. In the high-resolution XPS spectra, the C 1s peak of Gr-CNTs-Sn_4P_3 exhibits a slight positive shift when compared to that of Gr-CNTs, suggesting a modified electronic structure, possibly due to the partial transfer of electrons between the carbon matrix and Sn_4P_3. It possesses a flower-like morphology. It exhibits a superhydrophilic surface with a contact angle of 0°, suggesting its high surface wettability. For the OER in 1 M KOH, it affords an η of 169 mV at 20 mA cm^{-2}, suggesting its very high activity, while it affords ~96% retention for 105 h, suggesting its very high stability, and it undergoes negligible decay at 200 mA cm^{-2} after 5000 cycles of CV, suggesting its high durability. For overall water splitting in 1 M KOH, Gr-CNTs-Sn_4P_3//Gr-CNTs-Sn_4P_3 affords a potential of 1.482 V at 10 mA cm^{-2}, suggesting its very high activity.

Moreover, Vijayakumar *et al.*[98] observed that CoP-NC@NiFeP exhibits enhanced activity and stability for the HER and OER. It was prepared by precipitation followed by carbonization followed by pyro-phosphatization followed by hydrothermal treatment followed by pyro-phosphatization. CoP-NC@NiFeP exhibits higher activity for the HER and OER than CoP-NC and Co_3O_4-NC. It is composed of CoP-NC as a core and NiFeP as a shell. It contains crystalline CoP and NiFeP phases, while it contains N-doped amorphous carbon. It contains graphitic N, pyridinic N, and pyrrolic N. It contains Co, Ni, Fe, C, N, P, and O, which are homogeneously distributed. It possesses a coral-like morphology.

Co_xP/NC can be obtained from melamine-modified ZIF-9, while the surface modification of ZIF-9 with melamine can generate robust Co coordination sites on the surface of the ZIF-9 by coordination of Co with N donor sites in the melamine, and that could enhance the performance of the OER (ZIF-9: cobalt benzimidazole zeolitic imidazolate framework). Liu *et al.*[99] observed that Co_xP/NC-melamine exhibits enhanced activity and stability for the OER. The following steps are involved in its preparation. First, ZIF-9 was obtained by the microwave hydrothermal treatment. Then, ZIF-9-melamine was prepared by modifying ZIF-9 with melamine at 100 °C for 1 h. Finally, Co_xP/NC-melamine was obtained by phosphidation at 700 °C for 2 h under an Ar atmosphere. The surface engineering of ZIF-

9 using melamine constructs robust Co coordination sites on the surface of the ZIF-9 *via* coordination of Co with N donor sites in the melamine. DFT calculations disclose that the ZIF-9 is surface modified using melamine at coordinatively unsaturated Co sites and at coordinatively saturated Co sites through a thermodynamically favored ligand exchange process between melamine and benzimidazole in ZIF-9. Co_xP/NC prepared using melamine exhibits higher activity and electrochemical surface area for the OER than Co_xP/NC prepared using hexamethylenetetramine, Co_xP/NC prepared using phenanthroline, and Co_xP/NC. It is composed of Co_xP nanoparticles, which are dispersed on the carbon rods. It contains Co_2P and CoP phases. It contains graphitic N, pyridinic N, Co–N_x, and pyrrolic N. It contains Co, P, N, and C, which are homogeneously distributed.

Developing a synthesis route at an industrial scale for efficient electrocatalysts for the HER and OER is highly desirable for industrial applications. Hundred-gram scale production of the Cu_3P-Cu_2O heterostructure integrated with N, P dual doped porous carbon can be achieved by carbonization of Cu^{2+}-containing ion-exchange resins with KOH, and that could modify the electronic structure and provide abundant active sites, which could enhance the performance for the HER and OER. Zhu *et al.*[100] observed that Cu_3P-Cu_2O/NPC exhibits enhanced activity and stability for the HER and OER. Hundred-gram scale production of Cu_3P-Cu_2O/NPC was achieved by carbonization of Cu^{2+}-containing ion-exchange resins with KOH, where the pyrolysis was performed for 1 h at 850 °C under an N_2 atmosphere. Cu_3P-Cu_2O/NPC exhibits higher activity for the HER and OER than Cu_2O/NPC and Cu_3P/NPC. Cu_3P-Cu_2O/NPC exhibits lower charge transfer resistance for the OER than Cu_2O/NPC and Cu_3P/NPC. It is composed of Cu_3P-Cu_2O nanoparticles, which are embedded in N,P dual-doped porous carbon. It exhibits a heterointerface between hexagonal Cu_3P and cubic Cu_2O. It contains quaternary N, pyridinic N, and pyrrolic N. For the OER in 1 M KOH, it affords an η of 286 mV at 10 mA cm^{-2}, suggesting its very high activity, and it undergoes negligible decay at 150 mA cm^{-2} after 20 000 cycles of CV, suggesting its high durability. For the HER in 1 M KOH, it

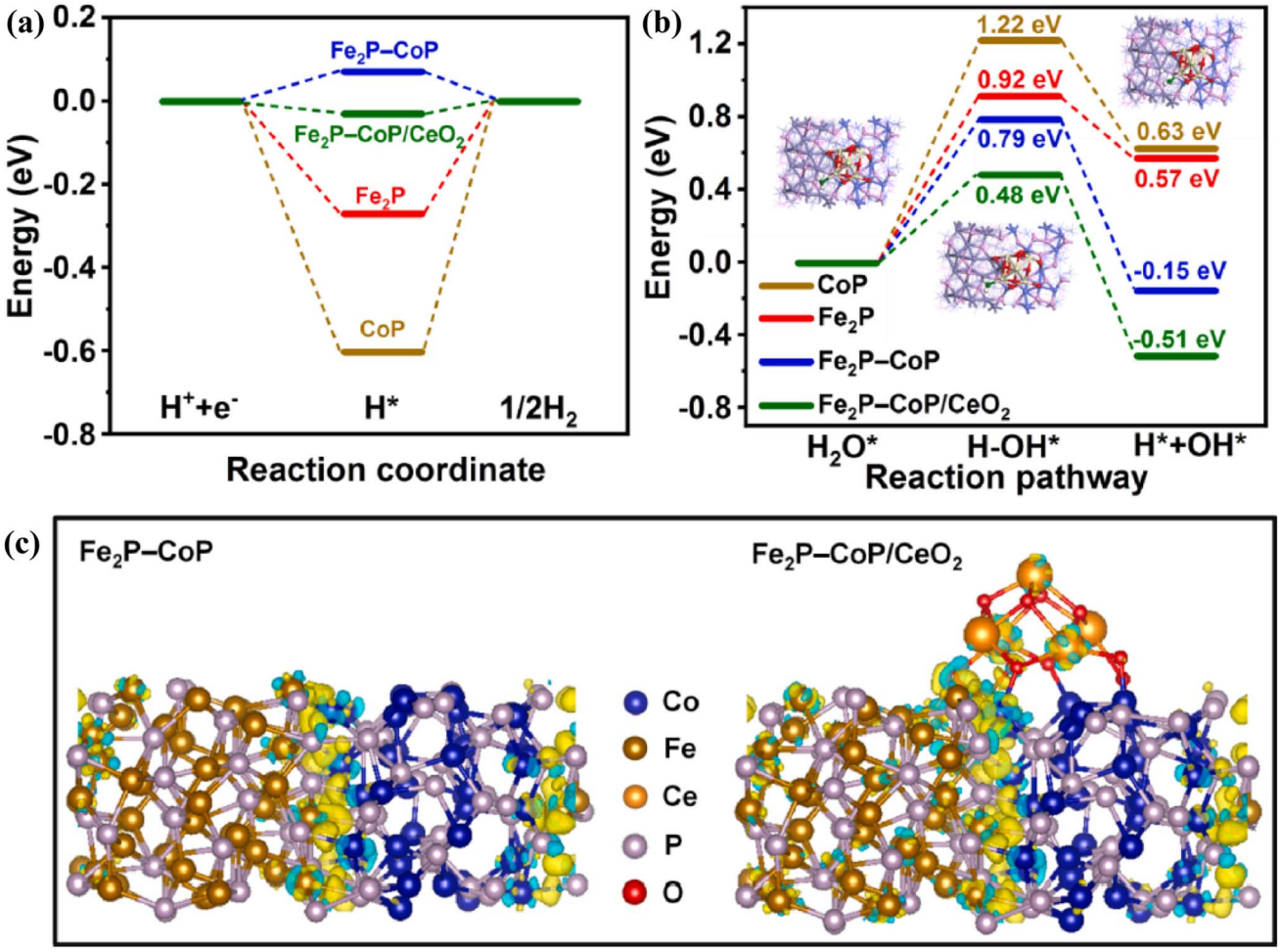

Fig. 5 (a) Gibbs free energy profiles for the HER on Fe_2P-CoP/CeO_2 in comparison with Fe_2P, CoP, and Fe_2P-CoP; (b) water dissociation capability of Fe_2P-CoP/CeO_2 in comparison with Fe_2P, CoP, and Fe_2P-CoP (insets depict the final, transient, and initial state geometries of Fe_2P-CoP/CeO_2 for water dissociation); (c) charge density difference plot of Fe_2P-CoP/CeO_2 in comparison with Fe_2P-CoP, where the yellow color indicates electron accumulation, and the cyan color represents electron depletion (reproduced with permission from ref. 101 Copyright 2022, Elsevier B.V.).

affords an η of $\sim$−155 mV at −10 mA cm^{-2}, suggesting its very high activity, and it undergoes negligible decay at −45 mA cm^{-2} after 20 000 cycles of CV, suggesting its high durability. For overall water splitting in 1 M KOH, Cu_3P-Cu_2O/NPC//Cu_3P-Cu_2O/NPC affords a potential of 1.57 V at 10 mA cm^{-2}, suggesting its very high activity, while it affords 98.19% retention at 1.7 V for 168 h, suggesting its very high stability.

Besides, Ding *et al.*[101] observed that Fe_2P-CoP/CeO_2 exhibits enhanced activity and stability for the HER and OER. It was synthesized by co-precipitation followed by refluxing followed by phosphidation (300 °C for 2 h under an N_2 atmosphere). Fe_2P-CoP/CeO_2 exhibits higher activity and electrochemical surface area for the HER and OER than Fe_2P-CoP and CeO_2. It contains a higher amount of oxygen vacancies than Fe_2P-CoP. It is crystalline and contains Fe_2P, CoP, and CeO_2 phases. It contains a triphase heterojunction. It contains Co, Fe, P, O, and Ce, which are homogeneously distributed. It possesses a porous nanocube structure having mesopores and micropores. In the high-resolution XPS spectra, the peaks corresponding to the Fe–P bond and Co–P bond of Fe_2P-CoP/CeO_2 show a slight positive shift when compared to that of Fe_2P-CoP, while the peaks of Ce 3d in Fe_2P-CoP/CeO_2 show a slight negative shift when compared to that of CeO_2, suggesting the modified electronic structure and strong electronic interaction at the triphase heterojunction, where the partial electrons could be transferred between Co/Fe and Ce. The ΔG_{H^*} value of Fe_2P-CoP/CeO_2 was calculated to be −0.03 eV (Fig. 5a), suggesting its enhanced intrinsic HER catalytic activity. The water dissociation energy of Fe_2P-CoP/CeO_2 (0.48 eV) is lower than that of CoP, Fe_2P, and Fe_2P-CoP (Fig. 5b), suggesting its accelerated HER kinetics. As shown in Fig. 5c, the charge density difference of Fe_2P-CoP and Fe_2P-CoP/CeO_2 discloses the increase in localized charge density at the Fe_2P–CoP interface, suggesting the strong interaction of Fe_2P with CoP. In contrast, charge density has been redistributed at the three-phase heterojunction interface, possibly due to the introduction of CeO_2 with Fe_2P-CoP, suggesting the enhanced intrinsic electrocatalytic activity. For the HER in 1 M KOH, it affords an η of −45 mV at −10 mA cm^{-2}, suggesting its outstanding activity. For overall water splitting in 1 M KOH, Fe_2P-CoP/CeO_2//Fe_2P-CoP/CeO_2 affords a potential of 1.52 V at 10 mA cm^{-2}, suggesting its very high activity, while it affords reasonable stability at 500 mA cm^{-2} for 40 h, suggesting its very high stability.

Moreover, Peng *et al.*[102] observed that Fe_2P-$WO_{2.92}$ exhibits enhanced activity and stability for the OER. It was synthesized on pretreated Ni foam with hydrothermal treatment, followed by phosphating at 350 °C for 2 h under an N_2 atmosphere. Fe_2P-$WO_{2.92}$ exhibits higher activity and electrochemical surface area for the OER than Fe_2P and $WO_{2.92}$. It is composed of monoclinic $WO_{2.92}$ and hexagonal Fe_2P phases. It contains oxygen vacancies. It contains W, Fe, P, C, and O, which are homogeneously distributed. It possesses a porous structure. For the OER in 1 M KOH, it affords an η of 215 mV at 10 mA cm^{-2}, suggesting its very high activity, while it affords 93% retention at 100 mA cm^{-2} for 60 h, suggesting its very high stability.

In addition, Chen *et al.*[103] observed that $Co(OH)_2$/NiP_x exhibits enhanced activity and stability for the OER. It was prepared on a cleaned carbon cloth by a two-step electrodeposition approach. $Co(OH)_2$/NiP_x exhibits higher activity and electrochemical surface area for the OER than NiP_x and $Co(OH)_2$. It is composed of $Co(OH)_2$ and NiP_x. In the high-resolution XPS spectra, the Co 2p peak of $Co(OH)_2$/NiP_x exhibits a slight shift compared to that of $Co(OH)_2$, suggesting a modified electronic structure. It possesses nanosheet array morphology. It exhibits a highly hydrophilic surface with a contact angle of 18.9°, suggesting its high surface wettability.

Besides, Cheng *et al.*[104] observed that CoP/FeOOH exhibits enhanced activity and stability for the OER. The following steps were involved in its preparation: at first, Co_3O_4 nanofibers were synthesized by electrospinning, followed by calcination, followed by annealing. Then, CoP was obtained by phosphorization of Co_3O_4 for 2 h at 400 °C under an Ar atmosphere. Finally, CoP/FeOOH was prepared by stirring the CoP in ethanol with $FeCl_3$ and NH_4HCO_3 for 6h at room temperature. CoP/FeOOH exhibits higher activity, higher electrochemical surface area, and lower charge transfer resistance for the OER than CoP and FeOOH. It is composed of a thin amorphous FeOOH layer, which is covered on CoP porous nanofiber. It exhibits a heterointerface between CoP and FeOOH. In the high-resolution XPS spectra, the Co 2p peak of CoP/FeOOH exhibits a slight shift compared to that of CoP, suggesting a modified electronic structure.

Fabrication of a nickel phosphate microprism with unique nanochannels through a one-step solvothermal method could expose more active sites, enhancing HER performance. Calcinating the nickel phosphate microprism followed by incorporating Fe could increase the proportion of high valence Ni ions, modify the electronic structure, and enhance the performance of the OER. Zhao *et al.*[105] observed that VSB/NiPO exhibits enhanced activity and stability for the HER, while Fe-VSB/NiPO-500 exhibits enhanced activity and stability for the OER. VSB/NiPO is a nickel phosphate microprism. The microprism is mainly composed of Versailles-Santa Barbara-5, which is a kind of nickel phosphate molecular sieve having the chemical formula of $Ni_{20}[(OH)_{12}(H_2O)_6][(HPO_4)_8(PO_4)_4]\cdot 12H_2O$. VSB/NiPO possesses unique nanochannels, which could expose more active sites and that could enhance the performance for the HER. VSB/NiPO exhibits higher activity, higher electrochemical surface area, and lower charge transfer resistance for the HER than $Ni(OH)_2$ and $Ni(PO_3)_2$. VSB/NiPO was prepared on the pretreated Ni foam by a solvothermal method. VSB/NiPO-500 was obtained by the calcination of VSB/NiPO at 500 °C. Fe-VSB/NiPO-500 was prepared by immersing VSB/NiPO-500 in $Fe(NO_3)_3$ solution at room temperature for 5 min. In the high-resolution XPS spectra, the proportion of Ni^{3+} in Fe-VSB/NiPO-500 is 92.86%, which is much higher than that of VSB/NiPO (59.52%), suggesting the modified electronic structure after Fe

doping, which could be due to the partial transfer of electrons between Fe and VSB/NiPO-500. Fe-VSB/NiPO-500 with a higher proportion of high valence Ni ions and a modified electronic structure could enhance the performance of the OER. Fe-VSB/NiPO-500 exhibits higher activity, higher electrochemical surface area, and lower charge transfer resistance for the OER than VSB/NiPO-500. For the OER in 1 M KOH, Fe-VSB/NiPO-500 affords an η of ~227 mV at 50 mA cm^{-2}, suggesting its very high activity, while it affords 98.2% retention at 50 mA cm^{-2} for 100 h, suggesting its very high stability. For the HER in 1 M KOH, it affords an η of −58 mV at −10 mA cm^{-2}, suggesting its very high activity. For overall water splitting in 1 M KOH, Fe-VSB/NiPO-500^{OER}//VSB/NiPO^{HER} affords a potential of 1.487 V at 10 mA cm^{-2}, suggesting its very high activity. In contrast, it affords 96.44% retention at 100 mA cm^{-2} for 100 h, suggesting its very high stability.

2.4. Constructing nitride electrocatalysts

Cobalt nitride coupled with N-doped carbon with a porous nanostructure could modify the electronic structure, afford optimal adsorption energy with intermediates, increase the conductivity, and that could enhance the performance of the HER and OER. Song *et al.*[106] observed that CoN@NC exhibits enhanced activity and stability for the HER and OER. The following steps were involved in its preparation: at first, the Co precursor was obtained on cleaned Ni foam by a vaporization deposition approach at 70 °C for 1 h. Finally, CoN@NC was prepared by calcinating the Co precursor under an NH_3 atmosphere at 300 °C for 1 h. CoN@NC exhibits higher activity and lower charge transfer resistance for the HER and OER than the Co precursor. It is composed of crystalline CoN, which is wrapped by an amorphous N-doped carbon layer. It contains Co-N, pyrrolic-N, pyridinic-N, and graphitic-N. It contains Co, C, and N, which are homogeneously distributed. It contains defects. It possesses porous nanosheet morphology. It exhibits the formation of CoOOH as the active species during the OER, which could be due to the partial oxidation of CoN in CoN@NC. For the HER in 1 M KOH, it affords an η of −61 mV at −10 mA cm^{-2}, suggesting its very high activity. For overall water splitting in 1 M KOH, CoN@NC//CoN@NC affords a potential of 1.53 V at 10 mA cm^{-2}, suggesting its very high activity.

Fabrication of nanostructured antiperovskite nitrides could modify the electronic structure, enhance the conductivity, expose abundant active sites, and that could enhance the performance of the HER and OER. Zhu *et al.*[107] observed that $CoN_{0.73}Co_3$ exhibits enhanced activity and stability for the HER, and $CuNCo_3$ exhibits enhanced activity and stability for the OER. $CoN_{0.73}Co_3$ or $CuNCo_3$ was prepared by hydrothermal treatment followed by annealing at 420 °C for 2 h under an NH_3 atmosphere. $CoN_{0.73}Co_3$ exhibits higher activity and lower

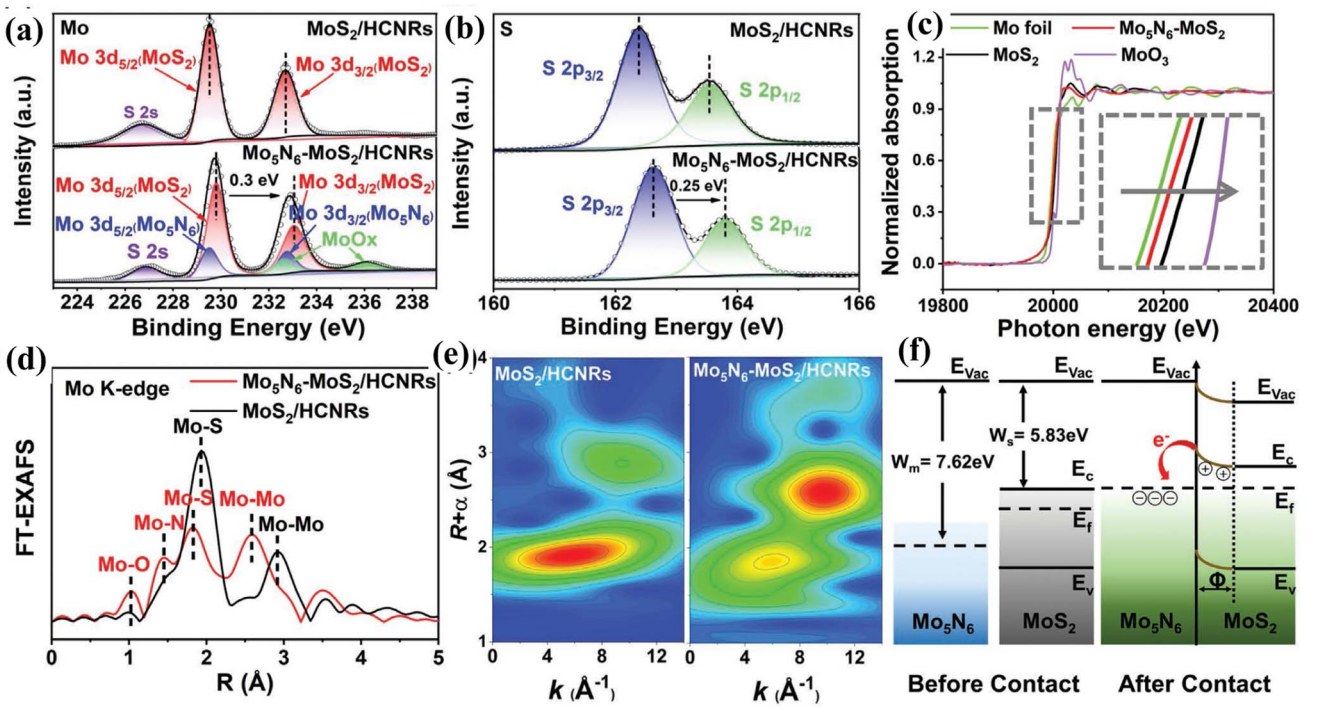

Fig. 6 High-resolution XPS spectra of (a) Mo 3d and (b) S 2p obtained from Mo_5N_6-MoS_2-HCNRs in comparison with 2H-MoS_2/HCNRs; (c) Mo K-edge XANES spectrum of Mo_5N_6-MoS_2/HCNR in comparison with Mo foil, MoO_3, and 2H-MoS_2/HCNRs; (d) FT-EXAFS curves and (e) WT-EXAFS of Mo_5N_6-MoS_2-HCNRs in comparison with 2H-MoS_2/HCNRs, disclosing the generation of the N–Mo–S triatomic interface and in-plane electronic coupling between MoS_2 and Mo_5N_6; (f) schematic illustration depicts the energy band of the Schottky-type Mo_5N_6-MoS_2 heterojunction, where the electron is transferred from 2H-MoS_2 to Mo_5N_6 due to the metallic Mo_5N_6/semiconducting MoS_2 heterojunction (E_{vac} = vacuum energy, E_g = energy gap, E_c = conduction band, E_f = Fermi level, E_v = valence band, Φ = depletion region, and W = work function) (reproduced with permission from ref. 108 Copyright 2022, Wiley-VCH GmbH).

charge transfer resistance for the HER than $CuNCo_3$. $CuNCo_3$ exhibits higher activity, higher electrochemical surface area, and lower charge transfer resistance for the OER than $CoN_{0.73}Co_3$. $CoN_{0.73}Co_3$ is antiperovskite $CoN_{0.73}Co_3$ having a cubic crystal structure. It contains Co and N, which are homogeneously distributed. It possesses nanowire-like morphology. $CuNCo_3$ is antiperovskite $CuNCo_3$, having a cubic crystal structure. It contains Co, Cu, and N, which are homogeneously distributed. It possesses nanosheet morphology. For the HER in 1 M KOH, it affords an η of -31 mV at -10 mA cm^{-2}, suggesting its very high activity. For overall water splitting in 1 M KOH, $CuNCo_3^{OER}//CoN_{0.73}Co_3^{HER}$ affords a potential of 1.53 V at 10 mA cm^{-2}, suggesting its very high activity.

Besides, Hu *et al.*[20] observed that $Co_2N_{0.67}/CoMoO_4$ exhibits enhanced activity and stability for the HER and OER. It was prepared on cleaned carbon cloth by hydrothermal treatment followed by hydrothermal treatment followed by annealing at 400 °C for 5 h under an NH_3 atmosphere. $Co_2N_{0.67}/CoMoO_4$ exhibits higher activity and lower charge transfer resistance for the HER and OER than $Co_2N_{0.67}$ and $CoMoO_4$. It exhibits a heterointerface between $Co_2N_{0.67}$ and $CoMoO_4$ phases. It contains Mo, Co, O, and N, which are homogeneously distributed. It contains Co^{2+}, Mo^{4+}, Co–N and pyridinic N. It possesses nanosheet morphology, where the nanosheet is composed of numerous nanoparticles. For the HER in 1 M KOH, it affords an η of -63 mV at -10 mA cm^{-2} and an η of -315 mV at high current density of -1000 mA cm^{-2}, suggesting its very high activity. For overall water splitting in 1 M KOH, $Co_2N_{0.67}/CoMoO_4//Co_2N_{0.67}/CoMoO_4$ affords a potential of 1.71 V at 100 mA cm^{-2} and 1.98 V at a current density of 1000 mA cm^{-2}, suggesting its very high activity.

Fabricating the Mott–Schottky heterointerface comprising metallic and semiconductor heterojunctions could tune the interfacial charge polarization and provide an optimal band structure, boosting the intrinsic activity for the HER. Pi *et al.*[108] observed that Mo_5N_6-MoS_2-HCNRs (HCNRs: hollow carbon nanoribbons) exhibit outstanding activity and stability for the HER. It was prepared by hydrothermal treatment followed by chemical polymerization followed by hydrothermal treatment (220 °C for 36 h) followed by thermal nitridation (750 °C under an NH_3 atmosphere). Mo_5N_6-MoS_2-HCNRs exhibit higher activity and electrochemical surface area for the HER than MoS_2-HCNRs and Mo_5N_6-HCNRs. It is composed of Mo_5N_6-MoS_2 nanosheets, which are grown on hollow carbon nanoribbons. It is polycrystalline, which contains Mo_5N_6 and 2H-MoS_2 phases with heterointerfaces. It contains Mo, N, S, and C, which are homogeneously distributed. In the high-resolution XPS spectra, the Mo 3d peak of Mo^{4+} (Fig. 6a) and S 2p peak of S^{2-} (Fig. 6b) of Mo_5N_6-MoS_2-HCNRs exhibit slight positive shifts when compared to those of MoS_2-HCNRs, suggesting a modified electronic structure, where partial electrons could be transferred from MoS_2 to Mo_5N_6. The Mo K-edge XANES spectra (Fig. 6c) disclose that the valence state of Mo in Mo_5N_6-MoS_2-HCNRs is almost closer to that of Mo foil, while the Mo_5N_6-MoS_2-HCNRs exhibit a lower valence state than MoS_2-HCNRs and MoO_3. In the FT-EXAFS curves (Fig. 6d), the MoS_2-HCNRs exhibit peaks for Mo–Mo, Mo–S, and Mo–O, whereas the Mo_5N_6-MoS_2-HCNRs exhibit peaks for Mo–N (1.5 Å), Mo–Mo, Mo–S, and Mo–O with a slight shift of positions for Mo atoms. In the radial distance *K*-space of Mo K-edge EXAFS (Fig. 6e), the WT intensity maximum of Mo_5N_6-MoS_2-HCNRs is at 6.0 Å corresponding to the Mo–S bond in pristine MoS_2, which is higher than that of the 5.6 Å in 2H-MoS_2/HCNRs, suggesting the generation of the N–Mo–S triatomic interface and synergistic electronic coupling. The work functions of 2H-MoS_2 and Mo_5N_6 are 5.83 and 7.62 eV, respectively, where the former corresponds to semiconductor characteristics and the latter to metallic characteristics. On integrating 2H–MoS_2 with Mo_5N_6 (Fig. 6f), a Mott–Schottky heterojunction comprising metallic Mo_5N_6 and semiconductor 2H-MoS_2 can be formed, which can cause the transfer of valence electrons from 2H-MoS_2 to Mo_5N_6 till the system reaches equilibrium, and that could boost the HER kinetics. For the HER in 1 M KOH, it affords an η of -53 mV at -10 mA cm^{-2} and an η of -315 mV at a current density of -1000 mA cm^{-2}, suggesting its outstanding activity. In contrast, it undergoes negligible decay for 33 h, suggesting its very high stability.

Besides, Zhai *et al.*[109] fabricated a heterostructured NiMoN/NiFe LDH array through hydrothermal treatment followed by nitridation followed by electrodeposition, where the amorphous NiFe LDH nanosheets on NiMoN nanorods could modify the electronic structure, enhance the conductivity, improve the charge transport, and facilitate the evolution of gas. For the OER in 1 M KOH, it affords an η of 266 mV at a current density of 1000 mA cm^{-2}, suggesting its very high activity, while it affords high stability. The design of a lamella-heterostructured nanoporous self-supported catalyst could expose abundant active sites, facilitate electron transfer, enhance conductivity, and enhance the performance of the OER. Zeng *et al.*[110] demonstrated a self-supported catalytic bimetallic iron–cobalt alloy/oxyhydroxide and cerium oxynitride ($FeCo/CeO_{2-x}N_x$) having a nanoporous lamella-heterostructure as the high-performance catalyst for the OER. The catalyst was prepared by alloying/dealloying lamella-nanostructured eutectic intermetallic compounds, followed by subsequent thermal nitridation. The 3D nanoporous architecture could expose abundant active sites, while the heterostructure could facilitate mass transport and electron transfer. For the OER in 1 M KOH, it affords an η of 360 mV at a current density of >3900 mA cm^{-2}, suggesting its very high activity, while it shows robust stability at a current density of ~1900 mA cm^{-2} for >1000 h.

2.5. Constructing carbon-based electrocatalysts

Fabrication of a Ni–C hybrid nanosheet array with dual nanoislands (one is metallic Ni and the other is metallic Ni coated by C) could modify the electronic structure, enhance the conductivity, expose abundant active sites, and that could enhance the

performance for the HER and OER. Zhu *et al.*[111] observed that the Ni–C hybrid nanosheet array exhibits enhanced activity for the HER and OER. The following steps were involved in its synthesis: at first, Ni MOF was prepared on pretreated Ni foam by hydrothermal treatment. Finally, Ni–C was obtained by annealing the Ni MOF at 450 °C for 2 h under an N_2 atmosphere. The Ni–C hybrid nanosheet array exhibits higher activity and lower charge transfer resistance for the HER than the Ni@C nanosheet array, Ni nanosheet array, and Ni MOF. It is a Ni–C hybrid nanosheet array, where the nanosheet comprises uniformly dispersed nanoparticles. It exhibits dual nanoislands on nanosheets, where one is a metallic Ni particle, and the other is a metallic Ni core with a graphitic C shell. It contains Ni and C, which are homogeneously distributed. For the HER in 1 M KOH, it affords an η of −37 mV at −10 mA cm^{-2}, suggesting its very high activity, and it undergoes almost negligible decay at

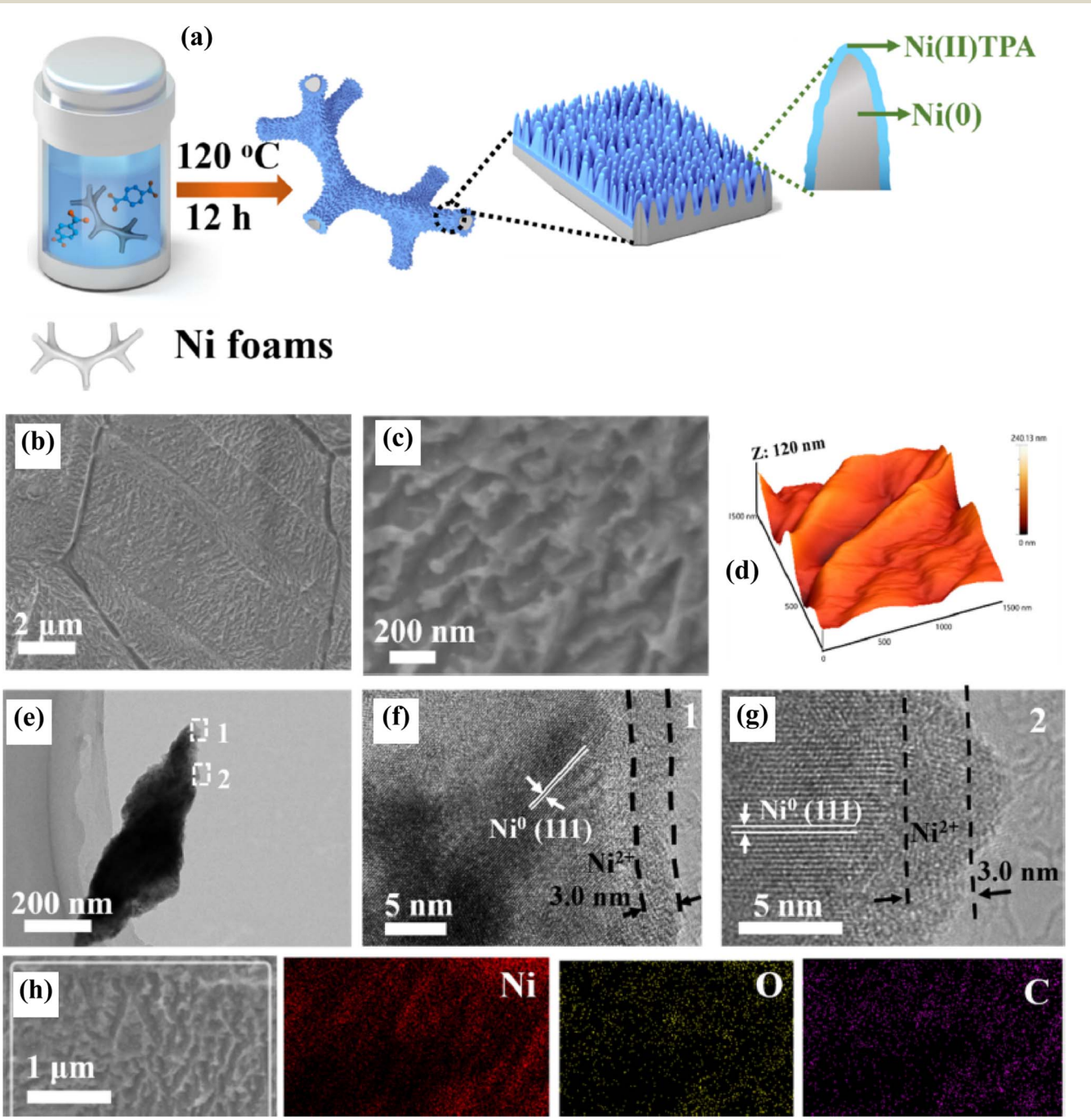

Fig. 7 Synthesis and characterization of KT-Ni(0)@Ni(II)-TPA: (a) chematic diagram depicting the preparation process through a hydrothermal reaction using TPA; (b and c) SEM images; (d) 3D surface architecture obtained using AFM; (e) TEM image; (f) and (g) HRTEM images; (h) SEM image and its corresponding elemental mapping (reproduced with permission from ref. 112 Copyright 2021, Elsevier B.V.).

−190 mA cm^{-2} after 10 000 cycles of CV, suggesting its high durability. For overall water splitting in 1 M KOH, Ni–C//Ni–C affords a potential of ∼1.45 V at 50 mA cm^{-2}, suggesting its very high activity.

Constructing a well-controlled core–shell heterostructured electrocatalyst with a superaerophobic surface could provide optimal adsorption energy with intermediates, and facilitate the evolution of gas, and that could enhance the activity and stability of the OER and HER. Hu *et al.*[112] observed that KT-Ni(0)@Ni(II)-TPA exhibits outstanding activity for the OER and it exhibits enhanced activity for the HER, and it was prepared by hydrothermal treatment (Fig. 7a), where a terephthalic acid (TPA)-regulated etching strategy is used on Ni foam for the preparation of a karst topography (KT) featured electrode containing core–shell structured Ni(0)@Ni(II)-TPA. KT-Ni(0)@Ni(II)-TPA exhibits higher activity for the OER than Ni(0)@Ni(II)-TPA and Ni(II)-TPA. It is a karst topography featured electrode containing core–shell structured Ni(0)@Ni(II)-TPA, where the Ni(0) as a core is surrounded by a thin amorphous Ni(II) complex as a shell with the thickness of ∼3.0 nm (Fig. 7f and g). The karst topography (Fig. 7a–c) is composed of arrays of tall towers and low valleys, where the tall tower is ∼120 nm in height (Fig. 7d) and ∼700 nm in length (Fig. 7e). It possesses a superaerophobic surface. It contains Ni, O, and C (Fig. 7h), which are homogeneously distributed. For the OER in 1 M KOH, it affords an η of 197 mV at 10 mA cm^{-2} and an η of 380 mV at a current density of 1500 mA cm^{-2}, suggesting its outstanding activity, while it affords reasonable stability at an η of 206 mV to 370 mV for >45 h, suggesting its very high stability.

Fabrication of a metallic Co and N dual doped carbon nanosheet array on copper foam could modify the electronic structure, improve the conductivity, expose more active sites, and enhance the performance for the HER. Xin *et al.*[113] observed that CoNC exhibits enhanced activity for the HER. The following steps were involved in its synthesis: at first, ZIF-L was grown on pretreated Cu foam by immersing in an aqueous solution of $Co(NO_3)_2$ and 2-methylimidazole for 1 h at room temperature. The recrystallized ZIF-L was obtained by immersing it in a fresh aqueous solution of Co ion and 2-methylimidazole. Finally, CoNC was obtained by pyrolyzing the recrystallized ZIF-L at 500 °C for 2 h under an Ar atmosphere. The CoNC on Cu foam exhibits higher activity, higher electrochemical surface area, and lower charge transfer resistance for the HER than CoNC on Ni foam. It is a metallic Co and N dual-doped carbon nanosheet array. It contains graphitic N, pyridinic N, pyrrolic N, and Co–N. For the HER in 1 M KOH, it affords an η of −64 mV at −10 mA cm^{-2}, suggesting its very high activity.

ZIF-67 represents a Co-based zeolitic imidazolate framework. The introduction of water in the synthesis of modified-ZIF-67 could alter the morphology and phase of the modified-ZIF-67, generating CoOOH with abundant oxygen vacancies as active species during the OER. In contrast, the heat and acid treatments of modified ZIF-67 could form active species for the HER. Lei *et al.*[114] observed that M-Co-CN exhibits enhanced activity for the HER, while the activated-modified-ZIF-67 exhibits enhanced activity and stability for the OER. The modified-ZIF-67 was obtained by the precipitation method at 0 °C, where a de-ionized water/methanol/isobutanol mixture solution was used. M–Co–CN was synthesized by heat treatment of modified-ZIF-67 at 900 °C for 2 h under an Ar atmosphere followed by acid treatment. The activated-modified-ZIF-67 was obtained by the electrochemical activation process of modified-ZIF-67. The morphology and crystalline phase of the modified ZIF-67 are changed when compared to that of ZIF-67, which could be due to the introduction of water molecules in the synthesis of modified ZIF-67. The modified ZIF-67 possesses nanorod-like morphology, whereas ZIF-67 possesses particle morphology. Moreover, the crystalline phase of modified ZIF-67 is entirely different from that of ZIF-67. In the high-resolution O 1s XPS spectrum of modified-ZIF-67, the peaks at 532.0 eV and 535.2 eV are ascribed to the –OH and absorbed H_2O, respectively, while the peak corresponding to adsorbed H_2O for modified-ZIF-67 exhibits a slight shift when compared to that of ZIF-67. The modified ZIF-67 contains Co, C, O, and N, which are homogeneously distributed. The formation of CoOOH with abundant oxygen vacancies on modified-ZIF-67 during the OER process is much easier when compared to that of ZIF-67, which could be due to the change in the morphology and crystalline phase of the modified-ZIF-67. M-Co-CN exhibits higher activity for the HER than Co–CN. The activated-modified-ZIF-67 exhibits higher activity and lower charge transfer resistance for the OER than modified-ZIF-67, activated-ZIF-67, and ZIF-67. For the OER in 1 M KOH, the activated-modified-ZIF-67 affords an η of 175 mV at 10 mA cm^{-2}, suggesting its very high activity, while it affords 96.6% retention at 100 mA cm^{-2} for 100 h, suggesting its very high stability. For the HER in 1 M KOH, M–Co–CN affords an η of −80 mV at −10 mA cm^{-2}, suggesting its very high activity. For overall water splitting in 1 M KOH, the activated-modified-ZIF-67^{OER}//M-Co-CN^{HER} affords a potential of 1.51 V at 10 mA cm^{-2}, suggesting its very high activity, while it affords 93.7% retention at 20 mA cm^{-2} for 100 h, suggesting its very high stability.

Fabrication of Co and N dual-doped carbon nanotubes having an abundance of atomically dispersed low-coordinate Co–N sites could provide optimal adsorption energy with intermediates, enhancing HER performance. Ding *et al.*[115] observed that Co-900-A exhibits enhanced activity for the HER. Co-900-A represents acid-treated Co-900, where Co-900 indicates Co and N co-doped carbon nanotubes with an abundance of atomically dispersed low-coordinate Co–N sites. Co-900-A contains Co, C, and N, which are homogeneously distributed. Co-900 was prepared by the precipitation method followed by pyrolysis at 950 °C for 1 h under an N_2 atmosphere, followed by stirring with reflux for 4 h and heat treatment at 900 °C for 1 h under an N_2 atmosphere.

Besides, Liu *et al.*[116] observed that Ni-Mo_2C-0.67 exhibits enhanced activity and stability for the HER. It was prepared on a Ni plate cathode by electrodeposition in molten LiF-NaF-KF-

Na_2MoO_4-K_2CO_3 salts at 750 °C. Ni-Mo_2C-0.67 is Ni-doped Mo_2C. It contains Mo^{2+}, Mo^{3+}, Mo^{4+}, and Mo^{6+}, where Mo^{2+} and Mo^{3+} could be ascribed to Mo–C in Mo_2C, while Mo^{4+} and Mo^{6+} could be attributed to MoO_2 and MoO_3, respectively, possibly due to the oxidation in air. It possesses a porous 3D flower-like morphology, which is composed of nanosheets. The contact angle of Ni-Mo_2C-0.67 is 0°, suggesting its super-hydrophilic surface and high wettability, which could enhance the electrolyte interaction and facilitate the gas evolution. The DFT calculations disclose that the ΔG_{H^*} value of optimized Ni-Mo_2C-0.67 was calculated to be −0.13 eV, suggesting its enhanced intrinsic HER catalytic activity. For the HER in 1 M KOH, it affords an η of −151 mV at −10 mA cm^{-2}, suggesting its very high activity, while it affords reasonable stability for 100 h, suggesting its very high stability.

Moreover, Xu *et al.*[117] observed that Fe/Mo_2C-NC^{OER}//Ni/Mo_2C-NC^{HER} exhibits enhanced activity and stability for overall water splitting. Ni/Mo_2C-NC or Fe/Mo_2C-NC was prepared on pretreated Ni foam by the impregnation method followed by carbonization (500 °C for 2 h followed by 750 °C for 2 h) under an Ar atmosphere. Ni/Mo_2C-NC exhibits higher activity, higher electrochemical surface area, and lower charge transfer resistance for the HER than Mo_2C-NC, Fe/Mo_2C-NC, and Co/Mo_2C-NC. In comparison, Fe/Mo_2C-NC exhibits higher activity for the OER than Mo_2C-NC, Ni/Mo_2C-NC, and Co/Mo_2C-NC. Ni/Mo_2C-NC comprises an Ni/Mo_2C heterostructure, which is embedded in N-doped carbon sheets. In the high-resolution XPS spectra, the Mo 3d peak of Ni/Mo_2C-NC exhibits a slight negative shift when compared to that of Mo_2C-NC, suggesting a modified electronic structure in the Ni/Mo_2C-NC possibly due to the partial transfer of electrons from Ni to Mo_2C, which could be due to the higher electronegativity of Mo, when compared to that of Ni. For overall water splitting in 1 M KOH, Fe/Mo_2C-NC^{OER}//Ni/Mo_2C-NC^{HER} affords a potential of 1.66 V at 100 mA cm^{-2}, suggesting its very high activity.

In addition, Yuan *et al.*[118] observed that Co/Mo_2C@C exhibits enhanced activity and stability for the HER and OER. It was prepared by stirring, followed by heat treatment for 3 h at 850 °C in an H_2/Ar atmosphere. Co/Mo_2C@C exhibits higher activity and lower charge transfer resistance for the HER and OER than Mo_2C@C. It comprises a cubic Co and hexagonal β-Mo_2C heterostructure supported on carbon. The carbon could be graphitic carbon or disordered carbon. In the high-resolution XPS spectra, the Mo 3d peak of Co/Mo_2C@C exhibits a slight negative shift when compared to that of Mo_2C@C, suggesting a modified electronic structure in Co/Mo_2C@C possibly due to the partial transfer of electrons from Co to Mo_2C, which could be due to the higher electronegativity of Mo, when compared to that of Co. As a result, the antibonding orbitals of Mo can be filled by the accumulated electrons on Mo_2C, which could alter the adsorption of H_2O* and H*, enhancing the intrinsic HER catalytic activity. The Mo in Mo_2C@C is completely oxidized after the OER. On the other hand, the oxidation of Mo in Co/Mo_2C@C is prevented after the OER, where Co is oxidized into CoOOH, suggesting the self-sacrifice effect of Co. The dissolution and oxidation of Mo_2C in Co/Mo_2C@C could be prevented by Co, where the formation of high valence Co ion and the well-preserved Mo_2C could lead to high stability for the OER. It contains micropores. For the HER in 1 M KOH, it affords an η of −98 mV at −10 mA cm^{-2}, suggesting its very high activity.

Besides, Li *et al.*[119] observed that Co-MoC/Mo_2C exhibits enhanced activity and stability for the HER. It was synthesized by hydrothermal treatment followed by the impregnation method followed by annealing (400 °C for 2 h followed by 750 °C for 2 h) under an Ar atmosphere. Co-MoC/Mo_2C exhibits higher activity (η at −10 mA cm^{-2}), higher electrochemical surface area, and lower charge transfer resistance for the HER than Ni-MoC/Mo_2C, Fe-MoC/Mo_2C, Cu-MoC/Mo_2C, and MoC. It is a Co-MoC/Mo_2C heterostructure. It exhibits heterogeneous interfaces between α-MoC and β-Mo_2C phases. It contains Co, Mo, C, and N, which are homogeneously distributed. It contains Mo^{2+}, Mo^{3+}, Mo^{4+}, and Mo^{6+}. In the high-resolution XPS spectra, the Co 2p peak of Co-MoC/Mo_2C exhibits a slight shift compared to that of Co-Mo_2C, suggesting a modified electronic structure. It contains pores (about 5.6 nm). It possesses 2D stripe morphology. For the HER in 1 M KOH, it affords an η of −82 mV at −10 mA cm^{-2}, suggesting its very high activity.

Moreover, Gong *et al.*[120] observed that Mo_2C-CoO@NC exhibits enhanced activity and stability for the HER and OER. It was obtained by electrospinning followed by pre-oxidation at 250 °C for 3 h in air and carbonization at 800 °C for 3 h under an N_2 atmosphere. It comprises hexagonal β-Mo_2C and cubic CoO, which are encapsulated in N-doped carbon nanofiber. It contains pyrrolic-N, pyridinic-N, and graphitic-N. It contains a Mo–N bond, suggesting the existence of interaction between Mo_2C and N-doped carbon. It contains Mo, Co, N, C, and O, which are homogeneously distributed. For the OER in 1 M KOH, it affords an η of 222 mV at 10 mA cm^{-2}, suggesting its very high activity.

In addition, Sun *et al.*[121] observed that Co_2P/Mo_2C@NC exhibits enhanced activity and stability for the HER and OER. It was prepared by heating the SiO_2@CoPMo@dopamine complex for 6 h at 800 °C under an N_2 atmosphere followed by acid treatment (HCl followed by HF). Co_2P/Mo_2C@NC exhibits higher activity, higher electrochemical surface area, and lower charge transfer resistance for the HER and OER than Co_2P@NC and Mo_2C@NC. It comprises a Co_2P/Mo_2C heterojunction, which is supported on N-doped carbon. It contains a Mo–N bond, suggesting the existence of interaction between Mo_2C and N-doped carbon. It contains Mo^{2+}, Mo^{4+}, and Mo^{6+}. It contains Mo, Co, P, C, and N, which are homogeneously distributed. It possesses a porous structure. The Co_2P/Mo_2C@NC//Co_2P/Mo_2C@NC electrolyzer using AsGa solar cells exhibits a solar-to-hydrogen conversion efficiency of 18.1%. For the OER in 1 M KOH, it affords an η of 209 mV at 10 mA cm^{-2}, suggesting its very high activity. For the HER in 1 M KOH, it affords an η of −86 mV at −10 mA cm^{-2}, suggesting its very high activity. For overall water splitting in 1 M KOH, Co_2P/

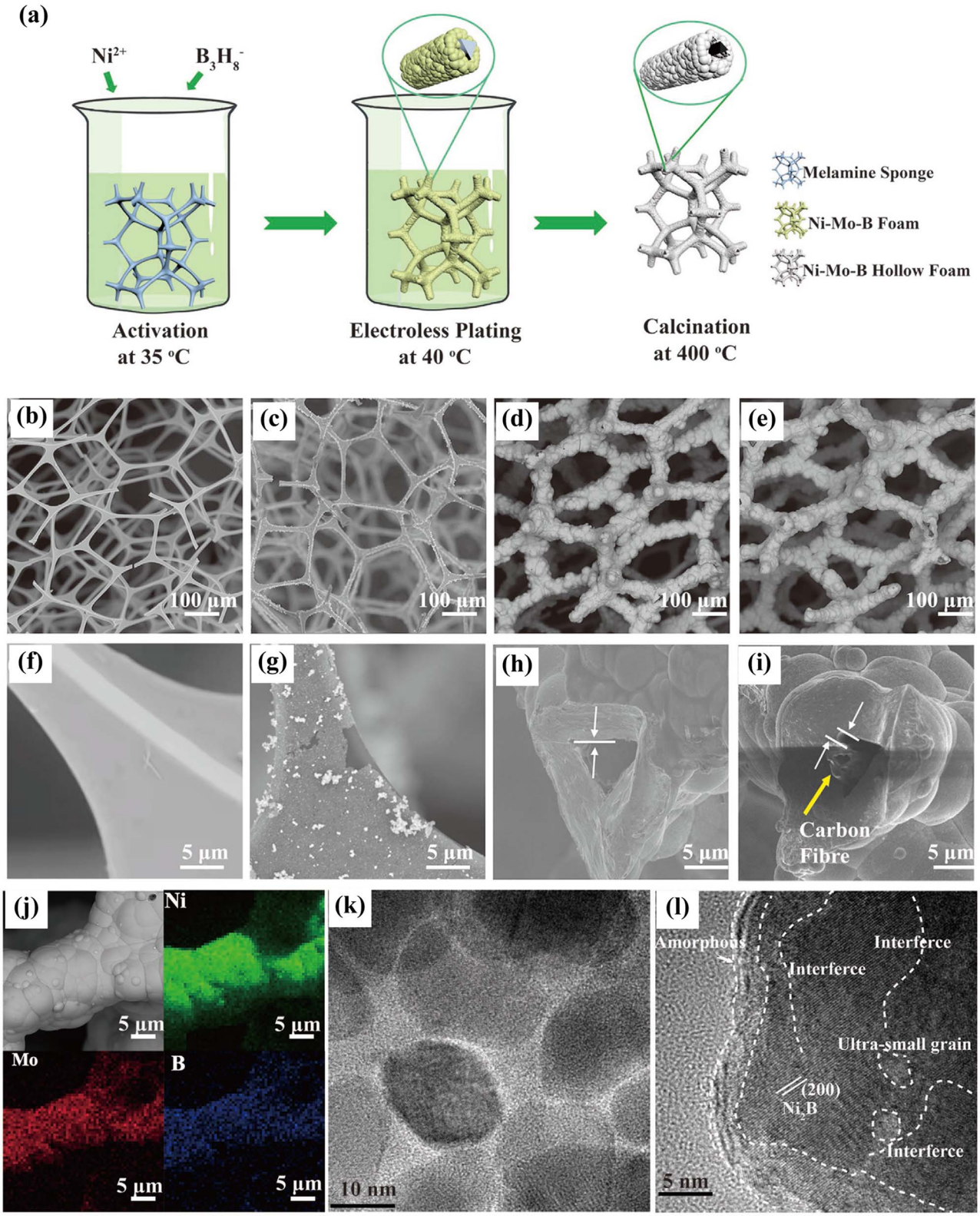

Fig. 8 (a) Schematic diagram depicting the fabrication process of NiMoB hollow foam; (b) and (f) SEM images of bare melamine sponge; (c) and (g) SEM images of activated melamine sponge; (d) and (h) SEM images of Ni-Mo-B foam; (e) and (i) SEM images of NiMoB hollow foam; (j) SEM image and the corresponding EDX elemental mapping of NiMoB hollow foam; (k) and (l) TEM images of NiMoB hollow foam (reproduced with permission from ref. 8 Copyright 2021, Wiley-VCH GmbH).

Mo_2C@NC//Co_2P/Mo_2C@NC affords a potential of 1.55 V at 10 mA cm^{-2}, suggesting its very high activity.

Besides, Luo *et al.*[21] observed that MoS_2/Mo_2C exhibits enhanced activity and stability for the HER. It was prepared on pretreated Ti foil by hydrothermal treatment followed by chemical vapor deposition at 750 °C with CH_4. MoS_2/Mo_2C exhibits higher activity and lower charge transfer resistance for the HER than MoS_2. MoS_2/Mo_2C is composed of MoS_2 microspheres, and the microspheres comprised MoS_2 nanosheets, where the β-Mo_2C nanoparticles are decorated on the edges of MoS_2 nanosheets. It contains S, Mo, and C, which are homogeneously distributed. The contact angle of MoS_2/Mo_2C is ∼0°, suggesting its superhydrophilic surface and high wettability, which could enhance the electrolyte interaction. At the same time, it exhibits a small gas bubble releasing size (<0.2 mm), which could facilitate the gas evolution. For the HER in 1 M KOH, it affords an η of ∼−120 mV at −10 mA cm^{-2}, and an η of −220 mV at a current density of −1000 mA cm^{-2}, suggesting its very high activity, and it undergoes negligible decay at −10 mA cm^{-2} after 10 000 cycles of CV, suggesting its high durability.

2.6. Constructing alloy/B/V/F/Si-based electrocatalysts

Fabrication of alloy ribbons by tuning the atomic packing structure could enhance the electron transferring efficiency, reduce the electron binding energy, and enhance the activity for the HER. Liu *et al.*[122] observed that $Ni_{56.5}Co_{35}Ti_{8.5}$ exhibits enhanced activity for the HER. The following steps were involved in the preparation of the $Ni_{56.5}Co_{35}Ti_{8.5}$ alloy ribbon: initially, the master alloy was obtained by arc-melting the

Table 1 Overpotential (η (Part 1: η from −14 to −127 mV)) to achieve −10 mA cm^{-2} for the hydrogen evolution reaction (HER) of various reported noble metal-free electrocatalysts in 1 M KOH alkaline electrolyte (η values to achieve greater than −10 mA cm^{-2} are indicated on the η, which is described in the footnote of this table)[a]

Section 1			Section 2		
HER electrocatalysts	η at −10 mA cm^{-2} (mV)	Ref.	HER electrocatalysts	η at −10 mA cm^{-2} (mV)	Ref.
$Mn_1Ni_1Co_1$-P	−14	10	Fe@Co/Se_2	−78	77
FeP/Ni_2P	−14	18	Fe-CoP	−78	85
NiMoB hollow foam	−18	8	M-Co-CN	−80	114
NiP_2-FeP_2@Cu nanoarray	−23.6	13	Co-MoC/Mo_2C	−82	119
Mn_6-CoO	−25.6	31	NiCoP	−84	83
$CoN_{0.73}Co_3$	−31	107	Co_2P/Mo_2C@NC	−86	121
Ni_2P-$Ni_{12}P_5$@Ni_3S_2	−32	72	NiCoFe-P/C	−87	93
Ni/MoO_2@CN	−33	15	NiS/MoS_2	−87	64
Ni-C hnsa	−37	111	1T Co-WS_2/$NiTe_2$/Ni	−88	73
Ni_2P	−37	82	$MoSe_2$@$NiCo_2Se_4$	−89	76
NiFeLa LDH/v-MXene	−38	57	C-$Ni_{1-x}O$/3D printed Ni	∼−90[b]	16
S-Co_2P@Ni_2P	−43	87	c-NiFe/a-NiFeOOH@NiMo	−91.9[c]	11
P-$CoMoO_4$	−44	40	HR-NiMoO@Ni	−96	38
Fe_2P-CoP/CeO_2	−45	101	WCoSe/WCo_3O_4	−98	78
MoO_2/Co	−48	30	Co/Mo_2C@C	−98	118
Ni_3S_2/$FeNi_2S_4$	−50	66	Ni/CeO_2@N-CNFs	−100	42
W-NiS_2/MoO_2	−52	63	hea-d48h	−101	125
Mo_5N_6-MoS_2-HCNRs	−53	108	Ni_3S_2-MoS_2	−103	65
Zn-Fe/Mn@Mn-FeP	−53	28	NiP	−107	88
S-NiFeP-20	−56	91	CoNiP	−107.56	84
VSB/NiPO	−58	105	CoP_3-Nb_2P/PCC	−111	95
CoN@NC	−61	106	$Ni_3Fe_{0.75}V_{0.25}$/$Ni_3Fe_{0.75}V_{0.25}N$	−113	129
$Co_2N_{0.67}$/$CoMoO_4$	−63	20	Mo_2C-CoO@NC	−115	120
CoNC	−64	113	Faceted $CuMn_2O_4$	−116	32
MH-TMO	∼−70	1g	Ni-CoP/Co_2P@NC	−117	97
$Ni_{2(1-x)}Mo_{2x}P$	−72	86	MoS_2/Mo_2C	∼−120	21
$Co_{0.21}Fe_{0.28}$(OH)F	−73	130	(Ni-Fe)S_x/Ni$Fe(OH)_y$	−124[d]	69
MoS_2-MoO_{3-x}/Ni_3S_2	−76	67	Fe,Ce-Ni_xS_y	−125	61
Fe-Co-CO_3-OH	−77	17	Bi_2O_3 based	−127	33

[a] η: overpotential; Ref.: references; PCC: plasma modified carbon cloth; HCNRs: hollow carbon nanoribbons; c-NiFe/a-NiFeOOH@NiMo: crystalline-NiFe/amorphous-NiFeOOH@NiMo; LDH: layered double hydroxide; VSB/NiPO: nickel phosphate microprism, where the microprism is mainly composed of Versailles-Santa Barbara-5, which is a kind of nickel phosphate molecular sieve having the chemical formula of $Ni_{20}[(OH)_{12}(H_2O)_6][(HPO_4)_8(PO_4)_4]\cdot 12H_2O$; MH-TMO: mesoporous and heterostructured transition metal oxides; hea-d48h: it is a high-entropy alloy (hea), which is de-alloyed for 48 h, where the $Ni_{30}Co_{30}Cr_{10}Fe_{10}Al_{18}W_2$ high-entropy alloy comprises FCC and ordered aluminum-enriched BCC phases, while three dimensional porous architecture is constructed by de-alloying (selective etching of the BCC phase) the high-entropy alloy for 48 h; N-CNFs: N-doped carbon nanofibers; hnsa: hybrid nanosheet array; M-Co-CN: it was synthesized by the heat treatment of modified-ZIF-67 followed by acid treatment, where ZIF-67 represents a Co-based zeolitic imidazolate framework. [b] ∼−90 mV at −100 mA cm^{-2}. [c] −91.9 mV at −20 mA cm^{-2}. [d] −124 mV at −100 mA cm^{-2}.

elements (purity: >99.9 wt%). Finally, the alloy ribbon was obtained by re-melting the master alloy in a quartz tube using induction melting, followed by injecting it onto a roller having a spinning tangent speed of about 40 m s^{-1}. $Ni_{56.5}Co_{35}Ti_{8.5}$ exhibits higher activity and lower charge transfer resistance for the HER than $Ni_{57.5}Co_{35}Ti_{7.5}$, $Ni_{50}Co_{37}Ti_{13}$, and $Ni_{46}Co_{35.5}Ti_{18.5}$. The enhanced activity of $Ni_{56.5}Co_{35}Ti_{8.5}$ for the HER is ascribed to low electron binding energy and low atomic packing density.

Table 2 Overpotential (η (Part 2: η from −128 to −425 mV)) to achieve −10 mA cm^{-2} for the hydrogen evolution reaction (HER) of various reported noble metal-free electrocatalysts in an alkaline electrolyte (η to achieve greater than −10 mA cm^{-2} are indicated on the η, which is described in the footnote of this table)[a]

HER electrocatalysts	η at −10 mA cm^{-2} (mV)	Electrolyte	Ref.
Ni_2P-Fe_2P	−128	1 M KOH	19
Ni/Mo_2C-NC	−131[b]	1 M KOH	117
Ce@NiCo LDH	−134[c]	1 M KOH	55
NiP_2/NbP@CNTs	−137[d]	1 M KOH	96
MoO_3-$Co(OH)_2$@Ag	−142	1 M KOH	39
Ni-Mo_2C-0.67	−151	1 M KOH	116
Cu_3P-Cu_2O/NPC	∼−155	1 M KOH	100
SAE_{HER}-ECT-NiSi	−156[e]	1 M KOH	132
CoP-NC@NiFeP	∼−163[f]	1 M KOH	98
e-FeCoNiCu-P	−165	1 M KOH	89
Fe-NiS-NiS_2	−167	1 M KOH	62
c-CoMnP/a-CoMn LDH	−170.3[g]	1 M KOH	56
Sn-Ni_3S_2	−171[h]	1 M KOH	14
Co_3O_4	−177	1 M KOH	29
Ni_xS_y@MnO_xH_y	−179	1 M KOH	68
Co-Mn-CO_3-OH	−180	1 M KOH	48
NiFe $LDH^{activated}$	−189	1 M KOH	51
Co-Ni_3S_2	−192	1 M NaOH	58
Ni_2P/NC	−201	1 M KOH	92
Co-Ni_3S_2	−220[i]	1 M KOH	59
KT-Ni(0)@Ni(II)-TPA	−228	1 M KOH	112
Fe_2P/Co@NPC	−235	1 M KOH	6e
Co-900-A	−246	1 M KOH	115
LSCO-$MoSe_2$	−260	1 M KOH	9
Ni-$FePS_3$	−356	1 M KOH	71
$Fe_{62.5}(CoNi)_{27.5}Cr_{10}$	−378	1 M NaOH	123
LSC-N-GQDs-$MoSe_2$	−409	1 M KOH	80
$Ni_{56.5}Co_{35}Ti_{8.5}$	−425[j]	1 M KOH	122

[a] η: overpotential; LDH: layered double hydroxide; Co-900-A: it represents acid treated Co-900, where Co-900 indicates Co and N co-doped carbon nanotubes with an abundance of low-coordinate Co–N sites; e-FeCoNiCu-P: electrochemically etched FeCoNiCu-P; CNTs: carbon nanotubes; c-CoMnP/a-CoMn LDH: crystalline CoMnP decorated amorphous CoMn LDH; KT-Ni(0)@Ni(II)-TPA: a terephthalic acid (TPA)-regulated etching strategy is used for the preparation of a karst topography (KT) featured electrode containing core-shell structured Ni(0)@Ni(II)-TPA; LSC/LSCO: $La_{0.5}Sr_{0.5}CoO_{3-\delta}$; N-GQDs: N-doped graphene quantum dots; SAE_{HER}-ECT-NiSi: NiSi is subjected to ECT followed by SAE_{HER}, where ECT is an electrochemical tuning process comprising lithiation and rapid delithiation of NiSi, while SAE_{HER} is a self-adaptive evolution that involves conducting multiple linear sweep voltammetry on ECT-NiSi under HER conditions. [b] −131 mV at −100 mA cm^{-2}. [c] −134 mV at −50 mA cm^{-2}. [d] −137 mV at −20 mA cm^{-2}. [e] −156 mV at −100 mA cm^{-2}. [f] −163 mV at −50 mA cm^{-2}. [g] −170.3 mV at −100 mA cm^{-2}. [h] −171 mV at −100 mA cm^{-2}. [i] −220 mV at −50 mA cm^{-2}. [j] −425 mV at −500 mA cm^{-2}.

Anodization followed by electrochemical activation of the $Fe_{60}(CoNi)_{30}Cr_{10}$ medium entropy alloy could generate an optimal metal (oxy)hydroxide layer as active sites on the surface, enhance the conductivity, increase the surface wettability, expose abundant active sites, and that could enhance the activity for the OER. Park *et al.*[123] observed that $Fe_{62.5}(CoNi)_{27.5}Cr_{10}$ exhibits enhanced activity for the HER, while the activated $Fe_{60}(CoNi)_{30}Cr_{10}$ exhibits enhanced activity for the OER. The activated $Fe_{60}(CoNi)_{30}Cr_{10}$ was prepared by the anodization of $Fe_{60}(CoNi)_{30}Cr_{10}$ followed by CV activation. $Fe_{62.5}(CoNi)_{27.5}Cr_{10}$ exhibits higher activity for the HER than $Fe_{60}(CoNi)_{30}Cr_{10}$, $Fe_{57.5}(CoNi)_{32.5}Cr_{10}$, CoCrNi, and CoCrFeMnNi. $Fe_{60}(CoNi)_{30}Cr_{10}$ exhibits higher activity for the OER than $Fe_{62.5}(CoNi)_{27.5}Cr_{10}$, $Fe_{57.5}(CoNi)_{32.5}Cr_{10}$, CoCrNi, and CoCrFeMnNi, while the activated $Fe_{60}(CoNi)_{30}Cr_{10}$ exhibits higher activity and lower charge transfer resistance for the OER than pristine $Fe_{60}(CoNi)_{30}Cr_{10}$ and anodized $Fe_{60}(CoNi)_{30}Cr_{10}$. $Fe_{60}(CoNi)_{30}Cr_{10}$ is a medium entropy alloy. The contact angle of activated $Fe_{60}(CoNi)_{30}Cr_{10}$ is 35°, suggesting its hydrophilic surface and high wettability, which could enhance the electrolyte interaction. The activated $Fe_{60}(CoNi)_{30}Cr_{10}$ contains an optimal metal (oxy)hydroxide layer as active sites on the surface of $Fe_{60}(CoNi)_{30}Cr_{10}$. For the OER in 1 M NaOH, the activated $Fe_{60}(CoNi)_{30}Cr_{10}$ affords an η of 187 mV at 10 mA cm^{-2}, suggesting its very high activity.

Polymetallic MOF can be obtained by a facile precipitation route at room temperature, while the CoNiCuMnAl high-entropy alloy wrapped in ultra-thin carbon can be prepared by the pyrolysis of the polymetallic MOF followed by acid treatment, and that could generate a metal (oxy)hydroxide as active sites during the OER, enhance the conductivity, and that could enhance the performance for the OER. Wang *et al.*[124] observed that CoNiCuMnAl@C exhibits enhanced activity and stability for the OER. It was obtained by room temperature precipitation followed by pyrolysis at 700 °C for 2 h under an Ar_2/H_2 atmosphere followed by acid treatment. CoNiCuMnAl@C exhibits higher activity for the OER than CoNiCuMnAl MOF, NiMnCuAl@C, CoMnCuAl@C, CoNiCuMn@C, CuMnAl@C, and CoNiMn@C. It possesses a core–shell structure, where the face-centered cubic CoNiCuMnAl high-entropy alloy as the core is wrapped in ultra-thin carbon as the shell. It exhibits the generation of a metal (oxy)hydroxide as an active species during the OER. For the OER in 1 M KOH, it affords an η of 215 mV at 10 mA cm^{-2}, suggesting its very high activity.

The $Ni_{30}Co_{30}Cr_{10}Fe_{10}Al_{18}W_2$ high-entropy alloy possesses a unique eutectic dual-phase microstructure comprising face-centered cubic (FCC) and ordered aluminum-enriched body-centered cubic (BCC) phases. Selective etching of the aluminum-enriched BCC phase of $Ni_{30}Co_{30}Cr_{10}Fe_{10}Al_{18}W_2$ could construct a three-dimensional porous architecture and increase the oxidation state of the alloying elements, which could expose abundant active sites and enhance the performance of the HER and OER. Han *et al.*[125] observed that hea-d48h exhibits enhanced activity and stability for the HER and OER. hea-d48h is a high-entropy alloy (HEA), which is de-alloyed for 48 h, where the $Ni_{30}Co_{30}Cr_{10}Fe_{10}Al_{18}W_2$ high-

entropy alloy comprises FCC and ordered aluminum-enriched BCC phases. In comparison, three-dimensional porous architecture is constructed by de-alloying (selective etching of the BCC phase) the high-entropy alloy for 48 h. The following steps were involved in the preparation of the $Ni_{30}Co_{30}Cr_{10}Fe_{10}Al_{18}W_2$ high-entropy alloy: at first, the master alloy ingot was obtained by vacuum arc melting. Finally, the high-entropy alloy was obtained by re-melting the ingot four times followed by drop-casting into a copper mold. The high-entropy alloy $Ni_{30}Co_{30}Cr_{10}Fe_{10}Al_{18}W_2$ de-alloyed for 48 h (hea-d48h) exhibits higher activity for the HER than bare $Ni_{30}Co_{30}Cr_{10}Fe_{10}Al_{18}W_2$, $Ni_{30}Co_{30}Cr_{10}Fe_{10}Al_{18}W_2$ de-alloyed for 12 h, $Ni_{30}Co_{30}Cr_{10}Fe_{10}Al_{18}W_2$ de-alloyed for 24 h, and $Ni_{30}Co_{30}Cr_{10}Fe_{10}Al_{18}W_2$ de-alloyed for 72 h. The high-entropy alloy $Ni_{30}Co_{30}Cr_{10}Fe_{10}Al_{18}W_2$ de-alloyed for 48 h (hea-d48h) exhibits higher activity and electrochemical surface area for the OER than bare $Ni_{30}Co_{30}Cr_{10}Fe_{10}Al_{18}W_2$, $Ni_{30}Co_{30}Cr_{10}Fe_{10}Al_{18}W_2$ de-alloyed for 12 h, $Ni_{30}Co_{30}Cr_{10}Fe_{10}Al_{18}W_2$ de-alloyed for 24 h, and $Ni_{30}Co_{30}Cr_{10}Fe_{10}Al_{18}W_2$ de-alloyed for 72 h. High-resolution XPS spectra disclose that both the bare $Ni_{30}Co_{30}Cr_{10}Fe_{10}Al_{18}W_2$ alloy and $Ni_{30}Co_{30}Cr_{10}Fe_{10}Al_{18}W_2$ de-alloyed for 48 h contain Cr, Fe, Al, Ni, Co, and W, suggesting the existence of all the elements after acid etching. However, the peaks corresponding to Cr, Fe, Al, Ni, Co, and W of $Ni_{30}Co_{30}Cr_{10}Fe_{10}Al_{18}W_2$ de-alloyed for 48 h exhibit a positive shift, when compared to that of bare $Ni_{30}Co_{30}Cr_{10}Fe_{10}Al_{18}W_2$ alloy, suggesting the

Table 3 Long-term stability (Part 1: 30 h to 400 h of duration) of various reported noble metal-free electrocatalysts for the hydrogen evolution reaction (HER) in 1 M KOH alkaline electrolyte[a]

HER electrocatalysts	Chr amp	Chr pot	Dur (h)	Remark after the stability test	Ref.
NiFeLa LDH/v-MXene	NA	Yes	400	Reasonable stability at a CD of −100 mA cm^{-2}	57
Ni/MoO_2@CN	NA	Yes	200	Negligible decay at a CD of −1000 mA cm^{-2}	15
$Ni_{2(1-x)}Mo_{2x}P$	Yes	NA	160	Reasonable stability	86
P-$CoMoO_4$	NA	Yes	100	Negligible decay at a CD of −50 mA cm^{-2}	40
MH-TMO	NA	Yes	100	Reasonable stability at a CD of −10 mA cm^{-2}	1g
HR-NiMoO@Ni	NA	Yes	100	Reasonable stability at a CD of −1000 A m^{-2}	38
Ni-Mo_2C-0.67	Yes	NA	100	Reasonable stability	116
Ni_xS_y@MnO_xH_y	NA	Yes	100	Reasonable stability at a CD of −100 mA cm^{-2}	68
Cu_3P-Cu_2O/NPC	Yes	NA	90	96% retention	100
Zn-Fe/Mn@Mn-FeP	NA	Yes	80	Negligible decay at a CD of −10 mA cm^{-2}	28
Mn_6-CoO	Yes	NA	60	83.6% retention	31
$Co_2N_{0.67}$/$CoMoO_4$	NA	Yes	60	Reasonable stability at a CD of −100 mA cm^{-2}	20
Sn-Ni_3S_2	Yes	NA	60	Negligible decay at an η of −223 mV	14
NiP_2-FeP_2@Cu nanoarray	NA	Yes	50	Reasonable stability at a CD of −1000 mA cm^{-2}	13
Ni-C hnsa	Yes	NA	50	Negligible decay at an η of −59 mV	111
CoP_3-Nb_2P/PCC	Yes	NA	50	93.6% retention	95
Faceted $CuMn_2O_4$	Yes	NA	50	Negligible decay	32
Ni-CoP/Co_2P@NC	Yes	NA	50	Negligible decay	97
CoP-NC@NiFeP	NA	Yes	50	Reasonable stability at a CD of −50 mA cm^{-2}	98
$Mn_1Ni_1Co_1$-P	Yes	NA	48	92% retention	10
$CoN_{0.73}Co_3$	Yes	NA	48	81% retention	107
Co/Mo_2C@C	Yes	NA	48	90.1% retention at an η of −98 mV	118
(Ni-Fe)S_x/$NiFe(OH)_y$	NA	Yes	48	Negligible decay at a CD of −120 mA cm^{-2}	69
Ni_2P-Fe_2P	NA	Yes	48	Reasonable stability at a CD of −100/−500 mA cm^{-2}	19
WCoSe/WCo_3O_4	NA	Yes	>45	Reasonable stability at a CD of −100 mA cm^{-2}	78
Fe,Ce-Ni_xS_y	NA	Yes	40	Negligible decay at a CD of −10 mA cm^{-2}	61
SAE_{HER}-ECT-NiSi	Yes	NA	35	Negligible decay at an η of −250 mV	132
NiCoFe-P/C	Yes	NA	34	Negligible decay	93
Mo_5N_6-MoS_2-HCNRs	Yes	NA	33	Negligible decay	108
NiP_2/NbP@CNTs	Yes	NA	33	~88.6% retention at an η of −247 mV	96
Fe_2P-CoP/CeO_2	Yes	NA	30	Negligible decay	101
VSB/NiPO	NA	Yes	>30	94.1% retention at a CD of −100 mA cm^{-2}	105
Fe-CoP	NA	Yes	30	Negligible decay at a CD of −10 mA cm^{-2}	85
Co_2P/Mo_2C@NC	Yes	NA	30	Negligible decay	121
$Ni_3Fe_{0.75}V_{0.25}$/$Ni_3Fe_{0.75}V_{0.25}N$	Yes	NA	30	Reasonable stability	129
Co-Ni_3S_2	Yes	NA	30	Negligible decay at an η of −462 mV	59

[a] η: overpotential; Ref.: references; Dur: duration of the stability test; Chr pot: chronopotentiometry; Chr amp: chronoamperometry; NA: not applicable; CD: current density; PCC: plasma modified carbon cloth; HCNRs: hollow carbon nanoribbons; CNTs: carbon nanotubes; LDH: layered double hydroxide; VSB/NiPO: nickel phosphate microprism, where the microprism is mainly composed of Versailles-Santa Barbara-5, which is a kind of nickel phosphate molecular sieve having the chemical formula of $Ni_{20}[(OH)_{12}(H_2O)_6][(HPO_4)_8(PO_4)_4]\cdot 12H_2O$; MH-TMO: mesoporous and heterostructured transition metal oxides; SAE_{HER}-ECT-NiSi: NiSi is subjected to ECT followed by SAE_{HER}, where ECT is an electrochemical tuning process comprising lithiation and rapid delithiation of NiSi, while SAE_{HER} is a self-adaptive evolution that involves conducting multiple linear sweep voltammetry on ECT-NiSi under HER conditions; hnsa: hybrid nanosheet array.

formation of high valence ions after acid etching. The dealloying of $Ni_{30}Co_{30}Cr_{10}Fe_{10}Al_{18}W_2$ for 48 h causes a hierarchically porous structure, which could expose abundant active sites. For overall water splitting in 1 M KOH, hea-d48h//hea-d48h affords a potential of 1.615 V at 10 mA cm^{-2}, suggesting its very high activity, while it affords 99.13% retention for 100 h, suggesting its very high stability.

BO_3^{3-} incorporated NiFe LDH could be fabricated by a facile electrodeposition method, while the incorporation of BO_3^{3-} in NiFe LDH could tune the electronic structure of the Fe atoms by filling into the oxygen vacancies, increase the oxidation state and coordination number of Fe atoms, enhance the conductivity, and that could enhance the performance for the OER. Liao *et al.*[126] observed that the NiFeB exhibits enhanced activity and stability for the OER. It was prepared on pretreated Ni foam by a one-step electrodeposition process by applying potentials for 10 cycles of CV. NiFeB exhibits higher activity, higher electrochemical surface area, and lower charge transfer resistance for the OER than NiFe LDH. NiFeB is composed of crystalline NiFe LDH, which BO_3^{3-} decorates. It contains B, Fe, Ni, and O, which are homogeneously distributed. In the high-resolution XPS spectra, the Fe 2p peak of NiFeB exhibits a slight positive shift when compared to that of NiFe LDH, suggesting a modified electronic structure in NiFeB, possibly due to the partial transfer of electrons from Fe to BO_3^{3-}. It exhibits a lesser amount of oxygen vacancies when compared to NiFe LDH. These results suggest that the incorporation of BO_3^{3-} in NiFe LDH could tune the electronic structure of the Fe atoms by filling into the oxygen vacancies. Moreover, incorporating BO_3^{3-} in NiFe LDH increases the coordination numbers of Fe atoms. It possesses ultrathin nanosheet morphology. For the OER in 1 M KOH, it affords an η of 201 mV at 10 mA cm^{-2}, suggesting its very high activity. In contrast, it affords reasonable stability at 500 mA cm^{-2} for 100 h, suggesting its high stability.

Table 4 Long-term stability (Part 2: 10 h to 29 h of duration) of various reported noble metal-free electrocatalysts for the hydrogen evolution reaction (HER) in 1 M KOH alkaline electrolyte, where the electrolyte other than 1 M KOH is indicated on the electrocatalyst[a]

HER electrocatalysts	Chr amp	Chr pot	Dur (h)	Remark after the stability test	Ref.
MoO_3-$Co(OH)_2$@Ag	NA	Yes	29	Reasonable stability at a CD of −100 mA cm^{-2}	39
Ni/CeO_2@N-CNFs	Yes	NA	27	Negligible decay at an η of −135 mV	42
CoN@NC	NA	Yes	25	Reasonable stability at a CD of −10 mA cm^{-2}	106
NiS/MoS_2	Yes	NA	25	Reasonable stability	64
FeP/Ni_2P	NA	Yes	24	Negligible decay at a CD of −100 mA cm^{-2}	18
Ni_2P-$Ni_{12}P_5$@Ni_3S_2	Yes	NA	24	Negligible decay	72
Ni_2P	Yes	NA	24	Reasonable stability at an η of −240 mV to −650 mV	82
MoO_2/Co	Yes	NA	24	Negligible decay	30
S-NiFeP-20	Yes	NA	24	Reasonable stability	91
1T Co-WS_2/$NiTe_2$/Ni	NA	Yes	24	97% retention at a CD of −50 mA cm^{-2}	73
$MoSe_2$@$NiCo_2Se_4$	Yes	NA	24	Negligible decay at an η of −135 mV	76
Ni_3S_2-MoS_2	NA	Yes	24	Reasonable stability at a CD of −10 mA cm^{-2}	65
MoS_2/Mo_2C	Yes	NA	24	Negligible decay	21
Ni/Mo_2C-NC	Yes	NA	24	Reasonable stability	117
Ce@NiCo LDH	Yes	NA	24	Reasonable stability	55
S-Co_2P@Ni_2P	Yes	NA	20	Negligible decay	87
$Co_{0.21}Fe_{0.28}(OH)F$	NA	Yes	20	Negligible decay at a CD of −20 mA cm^{-2}	130
Fe@Co/Se_2	NA	Yes	20	Negligible decay at a CD of −10 mA cm^{-2}	77
Co-MoC/Mo_2C	Yes	NA	20	Reasonable stability	119
Bi_2O_3 based	Yes	NA	20	85.4% retention	33
Co-Ni_3S_2 $^{1\ M\ NaOH}$	NA	Yes	18	Negligible decay	58
Fe_2P/Co@NPC	NA	Yes	>16	Negligible decay at a CD of −10 mA cm^{-2}	6e
Co_3O_4	NA	Yes	>15	Negligible decay at a CD of −100 mA cm^{-2}	29
NiCoP	Yes	NA	12	87% retention at an η of −84 mV	83
Fe-NiS-NiS_2	Yes	NA	12	Reasonable stability	62
Ni_2P/NC	Yes	NA	12	92% retention	92
MoS_2-MoO_{3-x}/Ni_3S_2	NA	Yes	11	Reasonable stability at a CD of −100 mA cm^{-2}	67
Co-Mn-CO_3-OH	NA	Yes	10	Negligible decay at a CD of −10 mA cm^{-2}	48

[a] η: overpotential; Ref.: references; Dur: duration of the stability test; Chr pot: chronopotentiometry; Chr amp: chronoamperometry; NA: not applicable; CD: current density; LDH: layered double hydroxide; N-CNFs: N-doped carbon nanofibers.

Fabrication of transition metal boride electrocatalysts with a 3D hollow structure could modify the electronic structure, provide optimal adsorption energy with intermediates, improve the conductivity, expose abundant active sites, provide high mechanical strength, and facilitate the gas evolution, which could enhance the activity and stability of the HER and OER. Liu *et al.*[8] observed that the NiMoB hollow foam exhibits outstanding activity and stability for the HER and OER. It was synthesized by the following steps (Fig. 8a). At first, the bare melamine sponge was activated at 35 °C for 10 minutes, where the bare 3D melamine sponge possessed a smooth surface (Fig. 8b and f), which was deposited by nanoparticles after activation (Fig. 8c and g). Then, NiMoB was formed by electroless plating at 40 °C for 4 h (Fig. 8d and h). Finally, NiMoB hollow foam was obtained by calcination at 400 °C for 4 h in an N_2 atmosphere (Fig. 8e and i), where the hollow space is observed between the inner wall of NiMoB and carbon fiber (Fig. 8i). The NiMoB hollow foam exhibits higher activity and electrochemical surface area for the HER and OER than NiMoB on the melamine sponge. It contains Ni, Mo, and B (Fig. 8j), which are homogeneously distributed. The atomic ratio of Ni : Mo : B of the NiMoB hollow foam is 1 : 0.03 : 0.23. It possesses an amorphous and crystalline state (Fig. 8k and l), where the inner part is mainly composed of a crystalline phase, and the outer layer is an amorphous state (thickness: $\approx$3 nm). It contains Ni_2B, Ni_3B, Ni, MoB_2, and Mo phases. It exhibits a density of 0.2 g cm^{-3}, which is almost nearer to that of nickel foam. It can withstand a pressure of 2.37 MPa during mechanical compression tests, suggesting its high mechanical stability. It exhibits a sheet resistance of 3.56 Ω sq^{-1}, which is less than that of the nickel foam (4.53 Ω sq^{-1}), suggesting its high electrical conductivity. It exhibits low gas mass transfer resistance. For the OER in 1 M KOH, it affords an η of 230 mV at 10 mA cm^{-2}, and an η of ~460 mV at a current density of 1000 mA cm^{-2}, suggesting its outstanding activity, while it undergoes negligible decay at 600 mA cm^{-2} after 500 cycles of CV, suggesting its very high durability. For the HER in 1 M KOH, it affords an η of −18 mV at −10 mA cm^{-2}, and an η of ~−420 mV at a huge current density of −1000 mA cm^{-2}, suggesting its outstanding activity, while it undergoes

Table 5 Durability of various reported noble metal-free electrocatalysts for the hydrogen evolution reaction (HER) in 1 M KOH alkaline electrolyte[a]

HER electrocatalysts	Cycles of CV	Remark after the durability test	Ref.
Cu_3P-Cu_2O/NPC	20 000	Negligible decay at −45 mA cm^{-2}	100
Sn-Ni_3S_2	10 000	Negligible decay at −1000 mA cm^{-2}	14
Ni-C hnsa	10 000	Almost negligible decay at −190 mA cm^{-2}	111
MoS_2/Mo_2C	10 000	Negligible decay at −10 mA cm^{-2}	21
NiCoP	10 000	Slight decay at −140 mA cm^{-2}	83
Fe-Co-CO_3-OH	10 000	Negligible decay at −1000 mA cm^{-2}	17
$Ni_{2(1-x)}Mo_{2x}P$	5000	Negligible decay at −700 mA cm^{-2}	86
CoP_3-Nb_2P/PCC	5000	Almost negligible decay at −500 mA cm^{-2}	95
$Mn_1Ni_1Co_1$-P	5000	Negligible decay at −10 mA cm^{-2}	10
FeP/Ni_2P	5000	Negligible decay at −1000 mA cm^{-2}	18
Ni_2P	5000	Negligible decay at −1200 mA cm^{-2}	82
Mn_6-CoO	3000	9 mV decay	31
$Co_2N_{0.67}$/$CoMoO_4$	3000	Slight decay at −200 mA cm^{-2}	20
Ni_2P-Fe_2P	3000	Negligible decay at −1000 mA cm^{-2}	19
Co_2P/Mo_2C@NC	3000	Negligible decay at −90 mA cm^{-2}	121
Ni/CeO_2@N-CNFs	3000	Negligible decay at −125 mA cm^{-2}	42
MoO_2/Co	3000	Very slight decay at −225 mA cm^{-2}	30
NiFeLa LDH/v-MXene	2000	Negligible decay at −700 mA cm^{-2}	57
Mo_5N_6-MoS_2-HCNRs	2000	Almost negligible decay at −100 mA cm^{-2}	108
NiS/MoS_2	2000	Negligible decay at −175 mA cm^{-2}	64
Fe@Co/Se_2	2000	Negligible decay at −10 mA cm^{-2}	77
Ni_3S_2/$FeNi_2S_4$	2000	Negligible decay at −300 mA cm^{-2}	66
Mo_2C-CoO@NC	2000	Very slight decay at −200 mA cm^{-2}	120
P-$CoMoO_4$	1000	Negligible decay	40
Zn-Fe/Mn@Mn-FeP	1000	Negligible decay at −200 mA cm^{-2}	28
Co/Mo_2C@C	1000	Negligible decay at −50 mA cm^{-2}	118
Fe,Ce-Ni_xS_y	1000	Negligible decay at −225 mA cm^{-2}	61
Co-Ni_3S_2	1000	Negligible decay at −1000 mA cm^{-2}	59
S-NiFeP-20	1000	Negligible decay	91
S-Co_2P@Ni_2P	1000	Negligible decay at −700 mA cm^{-2}	87
Hea-d48h	1000	Negligible decay at −10 mA cm^{-2}	125
NiMoB hollow foam	500	Negligible decay at −1000 mA cm^{-2}	8

[a] PCC: plasma modified carbon cloth; N-CNFs: N-doped carbon nanofibers; hnsa: hybrid nanosheet array; HCNRs: hollow carbon nanoribbons; hea-d48h: it is a high-entropy alloy (hea), which is de-alloyed for 48 h, where the $Ni_{30}Co_{30}Cr_{10}Fe_{10}Al_{18}W_2$ high-entropy alloy comprises FCC and ordered aluminum-enriched BCC phases, while three dimensional porous architecture is constructed by de-alloying (selective etching of the BCC phase) the high-entropy alloy for 48 h.

negligible decay at −1000 mA cm^{-2} after 500 cycles of CV, suggesting its very high durability. For overall water splitting in 1 M KOH, the NiMoB hollow foam//NiMoB hollow foam affords a potential of 1.431 V at 10 mA cm^{-2}, suggesting its very high activity, while it affords reasonable stability at 5000 mA cm^{-2} for 20 h, suggesting its very high stability.

Fabrication of nanostructured NiFeV hydroxide on the V_3O_7 nanofiber could modify the electronic structure, increase the oxidation state of Fe, enhance the conductivity, and expose more active sites, which could enhance the performance of the OER. Zhang *et al.*[127] observed that the NiFeV nanofibers exhibit enhanced activity and stability for the OER. It was synthesized by a two-step hydrothermal treatment. The NiFeV nanofibers exhibit higher activity, higher electrochemical surface area, and lower charge transfer resistance for the OER than NiFeV and NiFe. The NiFeV nanofibers are composed of NiFeV

Table 6 Overpotential (η (Part 1: η from 39 to 270 mV)) to achieve 10 mA cm^{-2} for the oxygen evolution reaction (OER) of various reported noble metal-free electrocatalysts in 1 M KOH alkaline electrolyte, where the electrolyte other than 1 M KOH is indicated on the electrocatalyst. (η values to achieve greater than 10 mA cm^{-2} are indicated on the η, which are described in the footnote of this table)[a]

Section 1			Section 2		
OER electrocatalysts	η at 10 mA cm^{-2} (mV)	Ref.	OER electrocatalysts	η at 10 mA cm^{-2} (mV)	Ref.
LSCO-$MoSe_2$	39	9	Fe,Ce-Ni_xS_y	227[f]	61
c-NiFe/a-NiFeOOH@NiMo	133.2[b]	11	Fe-Co-CO_3-OH	228	17
FeP/Ni_2P	154	18	FeCo-Ni_3S_4	230[g]	60
Gr-CNTs-Sn_4P_3	169[c]	12	Ni/CeO_2@N-CNFs	230	42
WCoSe/WCo_3O_4	175	78	NiMoB hollow foam	230	8
act-modified-ZIF-67	175	114	$Co(OH)_2/NiP_x$	236	103
NiFeV nf	181	127	Co_3O_4	236	29
Zn-Fe/Mn@Mn-FeP	184[d]	28	IronCE10s	239.5	26
NiFe LDH	186	25	$Co_{3-x}O_4$/NiO	240	36
$^{1\ M\ NaOH}Fe_{60}(CoNi)_{30}Cr_{10}^{activated}$	187	123	CoN@NC	240	106
Fe-CoP	190	85	S-FeOOH	244	24
NiFeLa LDH/v-MXene	191	57	Ag@NiFe LDH	246	54
Ce-NiFe	195	47	Fe_2P-CoP/CeO_2	248	101
$Co_{0.21}Fe_{0.28}(OH)F$	195	130	NiP_2/NbP@CNTs	248.2[h]	96
KT-Ni(0)@Ni(II)-TPA	197	112	$CoP/FeOOH^{Electrolyte\ NA}$	250	104
(Ni-Fe)S_x/$NiFe(OH)_y$	199	69	Ni/MoO_2@CN	250	15
FeNiOH	200	44	e-FeCoNiCu-P	250	89
Fe@Co/Se_2	200	77	Ce@NiCo LDH	250[i]	55
NiFeB	201	126	C/O-FeNi/FeF_2	253	131
S-NiFeP-10	201	91	Co/Mo_2C@C	254	118
$NiFe\ LDH^{activated}$	201	51	NiFe based	255	52
$Ni_3S_2/FeNi_2S_4$	201	66	$MoSe_2$@$NiCo_2Se_4$	255	76
Ni_5P_4@FeP	205	90	NiCoFe-P/C	257[j]	93
CoNiFe-OH	207	46	NiCoP	259	83
Co_2P/Mo_2C@NC	209	121	P-$CoMoO_4$	260[k]	40
FeOOH@NiFe LDH	210	53	$CuNCo_3$	260	107
OR-NiOOH	213	38	$Ni_3Fe_{0.75}V_{0.25}/Ni_3Fe_{0.75}V_{0.25}N$	260[l]	129
CoNiCuMnAl@C	215	124	FeCoS_x-PBA	266	70
Fe_2P-$WO_{2.92}$	215	102	NiFe-VO_x	267	128
MH-TMO	~216	1g	Sn-Ni_3S_2	267[m]	14
Ni_2P-Fe_2P	218	19	Hea-d48h	270[n]	125
Mo_2C-CoO@NC	222	120	Fe-NiS-NiS_2	270[o]	62
Fe-VSB/NiPO-500	~227[e]	105	CoP-NC@NiFeP	270[p]	98

[a] η: overpotential; Ref.: references; NA: not applicable; c-NiFe/a-NiFeOOH@NiMo: crystalline-NiFe/amorphous-NiFeOOH@NiMo; e-FeCoNiCu-P: electrochemically etched FeCoNiCu-P; CNTs: carbon nanotubes; LDH: layered double hydroxide; VSB/NiPO: nickel phosphate microprism, where the microprism is mainly composed of Versailles-Santa Barbara-5, which is a kind of nickel phosphate molecular sieve having the chemical formula of $Ni_{20}[(OH)_{12}(H_2O)_6][(HPO_4)_8(PO_4)_4]\cdot 12H_2O$; KT-Ni(0)@Ni(II)-TPA: a terephthalic acid (TPA)-regulated etching strategy is used for the preparation of a karst topography (KT) featured electrode containing core–shell structured Ni(0)@Ni(II)-TPA; LSC/LSCO: $La_{0.5}Sr_{0.5}CoO_{3-\delta}$; MH-TMO: mesoporous and heterostructured transition metal oxides; hea-d48h: it is a high-entropy alloy (hea), which is de-alloyed for 48 h, where the $Ni_{30}Co_{30}Cr_{10}Fe_{10}Al_{18}W_2$ high-entropy alloy comprises FCC and ordered aluminum-enriched BCC phases, while three dimensional porous architecture is constructed by de-alloying (selective etching of the BCC phase) the high-entropy alloy for 48 h; N-CNFs: N-doped carbon nanofibers; act-modified-ZIF-67: activated modified Co-based zeolitic imidazolate framework; NiFeV nf: NiFeV nanofibers; IronCE10s: the catalyst was prepared on an iron substrate by applying pulsed potentials for 10 seconds, where the substrate was used as a counter electrode; FeCoS_x-PBA: FeCoS embedded in a Prussian blue analogue hetero-nanoframes; Gr: graphene. [b] 133.2 mV at 20 mA cm^{-2}. [c] 169 mV at 20 mA cm^{-2}. [d] 184 mV at 20 mA cm^{-2}. [e] ~227 mV at 50 mA cm^{-2}. [f] 227 mV at 50 mA cm^{-2}. [g] 230 mV at 20 mA cm^{-2}. [h] 248.2 mV at 20 mA cm^{-2}. [i] 250 mV at 50 mA cm^{-2}. [j] 257 mV at 100 mA cm^{-2}. [k] 260 mV at 20 mA cm^{-2}. [l] 260 mV at 50 mA cm^{-2}. [m] 267 mV at 100 mA cm^{-2}. [n] 270 mV at 50 mA cm^{-2}. [o] 270 mV at 50 mA cm^{-2}. [p] 270 mV at 50 mA cm^{-2}.

hydroxide nanosheets as shells, which are vertically grown on the V_3O_7 nanofiber as the core. It exhibits a heterointerface between NiFeV hydroxide and V_3O_7. In the high-resolution XPS spectra, the Fe 2p peak of NiFeV nanofibers exhibits a slight positive shift when compared to that of NiFeV and NiFe, suggesting a modified electronic structure in NiFeV nanofibers with the formation of high valence Fe ions (Fe > 3+), possibly due to the partial transfer of electrons from Fe to V. It contains V^{3+}, V^{4+}, and, V^{5+}. In contrast, the NiFeV nanofibers exhibit a higher amount of low oxidation state vanadium (V^{3+}), when compared to that of NiFeV, suggesting the more partial transfer of electrons to the V in NiFeV nanofiber rather than in NiFeV, possibly due to the interfacial atom-substitution strategy. For the OER in 1 M KOH, it affords an η of 181 mV at 10 mA cm^{-2}, suggesting its very high activity.

Table 7 Overpotential (η (Part 2: η from 271.7 to 500 mV)) to achieve 10 mA cm^{-2} for the oxygen evolution reaction (OER) of various reported noble metal-free electrocatalysts in 1 M KOH alkaline electrolyte, where the electrolyte other than 1 M KOH is indicated on the electrocatalyst. (η values to achieve greater than 10 mA cm^{-2} are indicated on the η, which are described in the footnote of this table)[a]

OER electrocatalysts	η at 10 mA cm^{-2} (mV)	Ref.
c-CoFeP/a-CoFe LDH	271.7[b]	56
act-Ni-CoP/Co_2P@NC	272	97
MoO_2/Co	280	30
f-$Ni_{0.1}Co_{0.9}O_x$	282	35
$Co_2N_{0.67}$/$CoMoO_4$	283	20
SS-500-AO	284.3	79
Cu_3P-Cu_2O/NPC	286	100
Ni-$FePS_3$	287	71
$Mn_1Ni_1Co_1$-P	289	10
Co_3O_4 SS Mesh/ZnO$^{0.1\ M\ KOH}$	290	37
1T Co-WS_2/$NiTe_2$/Ni	290[c]	73
Fe/Mo_2C-NC	293[d]	117
Co-Mn-CO_3-OH	294[e]	48
SAE_{OER}-ECT-NiSi	296[f]	132
WO_3@$F_{0.1}$-C	298	27
NiFe-(OOH)-based$^{0.1\ M\ KOH}$	300[g]	50
Mn_6-CoO	301[h]	31
LSC-N-GQDs-$MoSe_2$	302	80
NiP	305	88
Defect-FeOOH^{activated}	307	49
Annealed α-Ni$(OH)_2$	310	43
Co-Ni_3S_2	310[i]	59
Co_xP/NC-melamine	312	99
Ni_xS_y@MnO_xH_y	326[j]	15
S-Co_2P@Ni_2P	~330[k]	87
Fe_2P/Co@NPC	331	6e
CuS-Ni_3S_2/CuNi	337[l]	22
C-$Ni_{1-x}O$/3D printed Ni	~340[m]	16
CoNiP	~350[n]	84
Ni_3S_2-MoS_2	~350[o]	65
Co-CoO/GO	372[p]	41
NiS/MoS_2	~410[q]	64
Co-$Ni_3S_2$$^{1\ M\ NaOH}$	500[r]	58

[a] η: overpotential; c-CoFeP/a-CoFe LDH: crystalline CoFeP decorated amorphous CoFe LDH; act-Ni-CoP/Co_2P@NC: activated Ni-CoP/Co_2P@NC; SS-500-AO: it is an electrocatalyst on SUS304 stainless steel, where the catalyst was prepared by selenization followed by heat treatment followed by electrochemical oxidation; SAE_{OER}-ECT-NiSi: NiSi is subjected to ECT followed by SAE_{OER}, where ECT is an electrochemical tuning process comprising lithiation and rapid delithiation of NiSi, while SAE_{OER} is a self-adaptive evolution that involves conducting multiple linear sweep voltammetry on ECT-NiSi under OER conditions; N-GQDs: N-doped graphene quantum dots; LSC/LSCO: $La_{0.5}Sr_{0.5}CoO_{3-\delta}$; Co_xP/NC-melamine: Co_xP/NC was prepared through a melamine assisted synthesis route. [b] 271.7 mV at 100 mA cm^{-2}. [c] 290 mV at 30 mA cm^{-2}. [d] 293 mV at 100 mA cm^{-2}. [e] 294 mV at 30 mA cm^{-2}. [f] 296 mV at 100 mA cm^{-2}. [g] 300 mV at ~701 A g^{-1}. [h] 301 mV at 50 mA cm^{-2}. [i] 310 mV at 50 mA cm^{-2}. [j] 326 mV at 100 mA cm^{-2}. [k] ~330 mV at 100 mA cm^{-2}. [l] 337 mV at 100 mA cm^{-2}. [m] ~340 mV at 100 mA cm^{-2}. [n] ~350 mV at 20 mA cm^{-2}. [o] ~350 mV at 50 mA cm^{-2}. [p] 372 mV at 50 mA cm^{-2}. [q] ~410 mV at 100 mA cm^{-2}. [r] 500 mV at 100 mA cm^{-2}.

Fabrication of NiFe-based vanadates with a moderate heterophase by a facile co-precipitation method could create abundant oxygen vacancies, enhance the conductivity, and generate hydroxide as active species by surface reconstruction during the OER, which could enhance the performance for the OER. Shao *et al.*[128] observed that NiFe-VO_x exhibits enhanced activity and stability for the OER. It was synthesized by a facile co-precipitation method. NiFe-VO_x exhibits higher activity and lower charge transfer resistance for the OER than NiCo-VO_x and CoFe-VO_x. NiFe-VOx exhibits a moderate heterophase, comprising both crystalline and amorphous structures. It contains $Ni_2FeV_3O_{11}$ and Ni_2FeVO_6 phases. It contains V, Fe, Ni, and O, which are homogeneously distributed. It contains abundant oxygen vacancies. It possesses nanoparticle morphology, which is further composed of small nanosheets. It exhibits the formation of hydroxide, possibly NiFe hydroxide, as an active species during the OER.

Fabrication of the $Ni_3Fe_{0.75}V_{0.25}$/$Ni_3Fe_{0.75}V_{0.25}N$ heterojunction could modify the electronic structure, enhance the conductivity, and that could enhance the performance for the HER and OER, while it could generate a cmetal(oxy) hydroxide layer as active species by surface reconstruction during the OER, and that could enhance the performance for the OER. Lu *et al.*[129] observed that $Ni_3Fe_{0.75}V_{0.25}$/$Ni_3Fe_{0.75}V_{0.25}N$ exhibits enhanced activity and stability for the HER and OER. It was synthesized by stirring followed by hydrothermal treatment followed by calcination at 500 °C for 8 h in an NH_3 atmosphere. $Ni_3Fe_{0.75}V_{0.25}$/$Ni_3Fe_{0.75}V_{0.25}N$ exhibits higher activity and lower charge transfer resistance for the HER and OER than Ni_3FeN, $Ni_3Fe_{0.75}V_{0.25}N$, and Ni_3Fe/Ni_3FeN. It is an $Ni_3Fe_{0.75}V_{0.25}$/$Ni_3Fe_{0.75}V_{0.25}N$ heterojunction, while it contains Ni_3FeN and Ni_3Fe phases, where V is incorporated in both phases. It exhibits a heterointerface. It contains V, Fe, Ni, and N, which are homogeneously distributed. It exhibits surface reconstruction during the OER, where a thin amorphous NiFeOOH layer is formed on the surface of the $Ni_3Fe_{0.75}V_{0.25}$/$Ni_3Fe_{0.75}V_{0.25}N$ heterojunction.

Fabrication of hybrid metal hydroxyl fluorides ($Co_{0.21}Fe_{0.28}$(OH)F) could modify the electronic structure, generate a larger Co^{2+}/Co^{3+} ratio, provide optimal adsorption energy with intermediates, enhance the conductivity, expose abundant active sites, and that could enhance the performance for the HER and OER. Li *et al.*[130] observed that $Co_{0.21}Fe_{0.28}$(OH)F exhibits enhanced activity and stability for the

HER and OER. It was obtained on pretreated Ni foam by one-step hydrothermal treatment at 120 °C for 3 h. $Co_{0.21}Fe_{0.28}(OH)F$ exhibits higher activity, higher electrochemical surface area, and lower charge transfer resistance for the OER than $Co_{0.14}Fe_{0.78}(OH)F$ and $Co_{0.41}Fe_{0.14}(OH)F$. In comparison, it exhibits higher activity for the HER than $Co_{0.14}Fe_{0.78}(OH)F$ and $Co_{0.41}Fe_{0.14}(OH)F$. It is a hybrid metal hydroxyl fluoride ($Co_{0.21}Fe_{0.28}(OH)F$), containing FeO(OH), Co(OH)F, and $Ni(OH)_2$ phases. It contains Fe, Co, O, F, and Ni, which are homogeneously distributed, where a small amount of Ni comes from the Ni foam substrate. The Co^{2+}/Co^{3+} ratio is 1.94 for $Co_{0.21}Fe_{0.28}(OH)F$, which is larger than

Table 8 Long-term stability (Part 1: 40 h to 1200 h of duration) of various reported noble metal-free electrocatalysts for the oxygen evolution reaction (OER) in 1 M KOH alkaline electrolyte[a]

OER electrocatalysts	Chr amp	Chr pot	Dur (h)	Remark after the stability test	Ref.
NiFeLa LDH/v-MXene	NA	Yes	1200	Negligible decay at a CD of 100 mA cm^{-2}	57
FeCo-Ni_3S_4	NA	Yes	360	22 mV decay at a CD of 20 mA cm^{-2}	60
Ni/MoO_2@CN	NA	Yes	200	Negligible decay at a CD of 1000 mA cm^{-2}	15
NiFe LDH	NA	Yes	192	Reasonable stability at a CD of 100 mA cm^{-2}	25
SS-500-AO	NA	Yes	160	Negligible decay at a CD of 10 mA cm^{-2}	79
Ni_xS_y@MnO_xH_y	NA	Yes	150	Reasonable stability at a CD of 100 mA cm^{-2}	68
$Co_{0.21}Fe_{0.28}(OH)F$	NA	Yes	120	Negligible decay at a CD of 20 mA cm^{-2}	130
Gr-CNTs-Sn_4P_3	NA	Yes	105	~96% retention	12
FeOOH@NiFe LDH	NA	Yes	100	Negligible decay	53
NiFeB	NA	Yes	100	Reasonable stability at a CD of 500 mA cm^{-2}	126
Ce-NiFe	NA	Yes	100	Reasonable stability at a CD of 1000 mA cm^{-2}	47
S-FeOOH	NA	Yes	100	Negligible decay at a CD of 20 mA cm^{-2}	24
Ni_5P_4@FeP	NA	Yes	100	Negligible decay at a CD of 100 mA cm^{-2}	90
OR-NiOOH	NA	Yes	100	Reasonable stability at a CD of 1000 A m^{-2}	38
Fe-VSB/NiPO-500	NA	Yes	100	98.2% retention at a CD of 50 mA cm^{-2}	105
MH-TMO	NA	Yes	100	Negligible decay at a CD of 10 mA cm^{-2}	1g
act-modified-ZIF-67	NA	Yes	100	96.6% retention at a CD of 100 mA cm^{-2}	114
Cu_3P-Cu_2O/NPC	Yes	NA	90	Negligible decay	100
Zn-Fe/Mn@Mn-FeP	NA	Yes	80	Negligible decay at a CD of 50 mA cm^{-2}	28
$Co_{3-x}O_4$/NiO	Yes	NA	60	Reasonable stability at 1.47 V	36
CoNiFe-OH	NA	Yes	60	Negligible decay at a CD of 10 mA cm^{-2}	46
Fe_2P-$WO_{2.92}$	NA	Yes	60	93% retention at a CD of 100 mA cm^{-2}	102
Mn_6-CoO	Yes	NA	~60	85.2% retention	31
Hea-d48h	Yes	NA	60	Negligible decay	125
Sn-Ni_3S_2	Yes	NA	60	Negligible decay at an η of 438 mV	14
Defect-FeOOH^{activated}	NA	Yes	55	Reasonable stability at a CD of 10 mA cm^{-2}	49
act-Ni-CoP/Co_2P@NC	Yes	NA	50	Negligible decay	97
WCoSe/WCo_3O_4	NA	Yes	50	Reasonable stability at a CD of 100 mA cm^{-2}	78
Ni_3S_2/$FeNi_2S_4$	Yes	NA	50	Negligible decay	66
(Ni-Fe)S_x/Ni$Fe(OH)_y$	NA	Yes	50	Negligible decay at a CD of 100 mA cm^{-2}	69
$CuNCo_3$	Yes	NA	48	86% retention	107
Ni-$FePS_3$	NA	Yes	48	Negligible decay at a CD of 10 mA cm^{-2}	71
Co/Mo_2C@C	Yes	NA	48	92.3% retention at an η of 254 mV	118
$Mn_1Ni_1Co_1$-P	Yes	NA	48	Reasonable stability	10
Ni_2P-Fe_2P	NA	Yes	48	Negligible decay at a CD of 100/500 mA cm^{-2}	19
$Co_2N_{0.67}$/$CoMoO_4$	NA	Yes	>45	Reasonable stability at a CD of 100 mA cm^{-2}	20
KT-Ni(0)@Ni(II)-TPA	Yes	NA	>45	Reasonable stability at an η of 206 mV to 370 mV	112
NiFeV nf	NA	Yes	>40	Reasonable stability	127
NiFe based	NA	Yes	40	Reasonable stability at a CD of 5 mA cm^{-2}	52
P-$CoMoO_4$	NA	Yes	40	Negligible decay at a CD of 50 mA cm^{-2}	40
Fe,Ce-Ni_xS_y	NA	Yes	40	Reasonable stability at a CD of 10 mA cm^{-2}	61
CoP-NC@NiFeP	NA	Yes	40	Negligible decay at a CD of 50 mA cm^{-2}	98

[a] η: overpotential; Ref.: references; Dur: duration of the stability test; Chr pot: chronopotentiometry; Chr amp: chronoamperometry; NA: not applicable; CD: current density; CNTs: carbon nanotubes; LDH: layered double hydroxide; VSB/NiPO: nickel phosphate microprism, where the microprism is mainly composed of Versailles-Santa Barbara-5, which is a kind of nickel phosphate molecular sieve having the chemical formula of $Ni_{20}[(OH)_{12}(H_2O)_6][(HPO_4)_8(PO_4)_4]\cdot 12H_2O$; KT-Ni(0)@Ni(II)-TPA: a terephthalic acid (TPA)-regulated etching strategy is used for the preparation of a karst topography (KT) featured electrode containing core–shell structured Ni(0)@Ni(II)-TPA; MH-TMO: mesoporous and heterostructured transition metal oxides; hea-d48h: it is a high-entropy alloy (hea), which is de-alloyed for 48 h, where the $Ni_{30}Co_{30}Cr_{10}Fe_{10}Al_{18}W_2$ high-entropy alloy comprises FCC and ordered aluminum-enriched BCC phases, while three dimensional porous architecture is constructed by de-alloying (selective etching of the BCC phase) the high-entropy alloy for 48 h; act-Ni-CoP/Co_2P@NC: activated Ni-CoP/Co_2P@NC; act-modified-ZIF-67: activated modified Co-based zeolitic imidazolate framework; NiFeV nf: NiFeV nanofibers; SS-500-AO: it is an electrocatalyst on SUS304 stainless steel, where the catalyst was prepared by selenization followed by heat treatment followed by electrochemical oxidation; Gr: graphene.

that of 1.38 for $Co_{0.14}Fe_{0.78}(OH)F$, and 1.30 for $Co_{0.41}Fe_{0.14}(OH)F$, suggesting the exposure of more Co^{2+} ions due to the presence of an optimal proportion of Co and Fe in $Co_{0.21}Fe_{0.28}(OH)F$. It exhibits the formation of metal hydroxide (metal(oxy)hydroxide or metal hydroxide) as active species by surface reconstruction during the OER. It possesses nanosheet array morphology. For the OER in 1 M KOH, it affords an η of 195 mV at 10 mA cm^{-2}, suggesting its very high activity, while it undergoes negligible decay at 20 mA cm^{-2} for 120 h, suggesting its very high stability. For the HER in 1 M KOH, it affords an η of −73 mV at −10 mA cm^{-2}, suggesting its very high activity. For overall water splitting in 1 M KOH, $Co_{0.21}Fe_{0.28}(OH)F//Co_{0.21}Fe_{0.28}(OH)F$ affords a potential of 1.53 V at 10 mA cm^{-2}, suggesting its high activity.

Fabrication of carbon-confined iron–nickel alloy/iron fluoride could modify the electronic structure, enhance the conductivity, expose abundant active sites, and enhance the performance of the OER. Li *et al.*[131] observed that C/O-FeNi/FeF_2 exhibits enhanced activity and stability for the OER. It was synthesized by hydrothermal treatment (for the formation of the Fe_2Ni MIL MOF) followed by carbonization at 800 °C for 1 h in N_2 (for the formation of FeNi-800 °C) followed by fluorination at 450 °C for 2 h in N_2 (for the formation of C/O-FeNi/FeF_2). C/O-FeNi/FeF_2 exhibits higher activity, higher electrochemical surface area, and lower charge transfer resistance for

Table 9 Long-term stability (Part 2: 4 h to 35 h of duration) of various reported noble metal-free electrocatalysts for the oxygen evolution reaction (OER) in 1 M KOH alkaline electrolyte, where electrolytes other than 1 M KOH are indicated on the electrocatalyst[a]

OER electrocatalysts	Chr amp	Chr pot	Dur (h)	Remark after the stability test	Ref.
SAE_{OER}-ECT-NiSi	Yes	NA	35	Negligible decay at an η of 470 mV	132
NiCoFe-P/C	Yes	NA	34	Negligible decay	93
NiP_2/NbP@CNTs	Yes	NA	33	~88.2% retention at an η of 274.1 mV	96
Co_2P/Mo_2C@NC	Yes	NA	30	Negligible decay	121
$Ni_3Fe_{0.75}V_{0.25}/Ni_3Fe_{0.75}V_{0.25}N$	Yes	NA	30	Reasonable stability	129
Fe_2P-CoP/CeO_2	Yes	NA	30	Negligible decay	101
Co-Ni_3S_2	Yes	NA	30	Negligible decay at an η of 465 mV	59
Fe-CoP	NA	Yes	30	Negligible decay at a CD of 1000 mA cm^{-2}	85
Annealed α-$Ni(OH)_2$	NA	Yes	26	Negligible decay at a CD of 10 mA cm^{-2}	43
CoN@NC	NA	Yes	25	Reasonable stability at a CD of 10 mA cm^{-2}	106
WO_3@$F_{0.1}$-C	NA	Yes	24	Negligible decay	27
f-$Ni_{0.1}Co_{0.9}O_x$	Yes	NA	24	Reasonable stability at a potential of 1.53 V	35
CoNiCuMnAl@C	NA	Yes	24	Negligible decay at a CD of 10 mA cm^{-2}	124
1T Co-WS_2/$NiTe_2$/Ni	NA	Yes	24	Reasonable stability at a CD of 50 mA cm^{-2}	73
S-NiFeP-10	Yes	NA	24	Reasonable stability	91
Co-Ni_3S_2[1 M NaOH]	NA	Yes	24	Negligible decay at a CD of 50 mA cm^{-2}	58
Fe/Mo_2C-NC	Yes	NA	24	Reasonable stability	117
Ce@NiCo LDH	Yes	NA	24	Reasonable stability at a potential of 1.55 V	55
FeP/Ni_2P	NA	Yes	24	Negligible decay at 100 mA cm^{-2}	18
FeNiOH	Yes	NA	20	Negligible decay at a potential of 1.46 V	44
CoP/FeOOH[Electrolyte NA]	NA	Yes	20	Reasonable stability at a CD of 10 mA cm^{-2}	104
S-Co_2P@Ni_2P	Yes	NA	20	Negligible decay	87
Fe@Co/Se_2	NA	Yes	20	Negligible decay at a CD of 10 mA cm^{-2}	77
Ag@NiFe LDH	Yes	NA	>19	Reasonable stability	54
Co-Mn-CO_3-OH	NA	Yes	18	Negligible decay at a CD of 50 mA cm^{-2}	48
C/O-FeNi/FeF_2	Yes	NA	16	Reasonable stability	131
Fe_2P/Co@NPC	NA	Yes	>16	Reasonable stability at a CD of 10 mA cm^{-2}	6e
Co_3O_4	NA	Yes	>15	Negligible decay at a CD of 100 mA cm^{-2}	29
CuS-Ni_3S_2/CuNi	NA	Yes	15	Negligible decay at a CD of 100 mA cm^{-2}	22
NiFe-VO_x	NA	Yes	12	24.2 mV decay at a CD of 10 mA cm^{-2}	128
Co-CoO/GO	Yes	NA	12	93% retention at a potential of 1.71 V	41
NiCoP	Yes	NA	12	99% retention at an η of 259 mV	83
Fe-NiS-NiS_2	Yes	NA	12	Reasonable stability at an η of 270 mV	62
$Co(OH)_2$/NiP_x	NA	Yes	>10	Reasonable stability at a CD of 10 mA cm^{-2}	103
$FeCoS_x$-PBA	Yes	NA	10	98.3% retention	70
Ni/CeO_2@N-CNFs	Yes	NA	>10	Negligible decay	42
Co_3O_4 SS Mesh/ZnO[0.1 M KOH]	Yes	NA	7	Reasonable stability	37
Co_xP/NC-melamine	NA	Yes	4	Reasonable stability at a CD of 10 mA cm^{-2}	99

[a] η: overpotential; Ref.: references; Dur: duration of the stability test; Chr pot: chronopotentiometry; Chr amp: chronoamperometry; NA: not applicable; CD: current density; SAE_{OER}-ECT-NiSi: NiSi is subjected to ECT followed by SAE_{OER}, where ECT is an electrochemical tuning process comprising lithiation and rapid delithiation of NiSi, while SAE_{OER} is a self-adaptive evolution that involves conducting multiple linear sweep voltammetry on ECT-NiSi under OER conditions; CNTs: carbon nanotubes; LDH: layered double hydroxide; $FeCoS_x$-PBA: FeCoS embedded in Prussian blue analogue hetero-nanoframes; N-CNFs: N-doped carbon nanofibers; Co_xP/NC-melamine: Co_xP/NC was prepared through a melamine assisted synthesis route.

the OER than FeNi-800 °C and Fe_2Ni MIL MOF. It is composed of oxygen-doped FeNi/FeF_2, confined by carbon. In the high-resolution XPS spectra, the Fe 2p peak corresponding to Fe^{2+} of C/O-FeNi/FeF_2 exhibits a slight positive shift when compared to that of FeNi-800 °C, suggesting a modified electronic structure. It could exhibit the formation of metal(oxy) hydroxide by surface reconstruction during the OER.

An electrochemical tuning process comprising lithiation and rapid delithiation of the nanostructured NiSi could form a core–shell structure. In contrast, the subsequent electrochemical activation could increase the oxygen vacancies, enhance the conductivity, provide optimal adsorption energy with intermediates, increase the electrochemical surface area, and that could enhance the performance of the HER and OER. Chang *et al.*[132] observed that SAE_{HER}-ECT-NiSi exhibits enhanced activity and stability for the HER, while SAE_{OER}-ECT-NiSi exhibits enhanced activity and stability for the OER. In SAE_{HER}-ECT-NiSi, the NiSi nanowires prepared by CVD are subjected to ECT followed by SAE_{HER}, where ECT is an electrochemical tuning process comprising lithiation and rapid delithiation of NiSi. At the same time, SAE_{HER} is a self-adaptive evolution that involves conducting multiple linear sweep voltammetry on ECT-NiSi under HER conditions. In SAE_{OER}-ECT-NiSi, the NiSi nanowires prepared by CVD are subjected to ECT followed by SAE_{OER}, where ECT is an electrochemical tuning process comprising lithiation and rapid delithiation of NiSi. At the same time, SAE_{OER} is a self-adaptive evolution that involves conducting multiple linear sweep voltammetry on ECT-NiSi under OER conditions. SAE_{HER}-ECT-NiSi exhibits higher activity and lower charge

Table 10 Durability of various reported noble metal-free electrocatalysts for the oxygen evolution reaction (OER) in 1 M KOH alkaline electrolyte, where the electrolyte other than 1 M KOH is indicated on the electrocatalyst[a]

OER electrocatalysts	Cycles of CV	Remark after the durability test	Ref.
Cu_3P-Cu_2O/NPC	20 000	Negligible decay at 150 mA cm^{-2}	100
NiCoP	10 000	Negligible decay at 90 mA cm^{-2}	83
Sn-Ni_3S_2	10 000	Negligible decay at 2000 mA cm^{-2}	14
Ni_xS_y@MnO_xH_y	5000	Negligible decay at 500 mA cm^{-2}	68
Gr-CNTs-Sn_4P_3	5000	Negligible decay at 200 mA cm^{-2}	12
$Mn_1Ni_1Co_1$-P	5000	Negligible decay at 10 mA cm^{-2}	10
FeP/Ni_2P	5000	Negligible decay at 1500 mA cm^{-2}	18
CuS-Ni_3S_2/CuNi	5000	Negligible decay at 1000 mA cm^{-2}	22
CoNiCuMnAl@C	3000	Negligible decay at 90 mA cm^{-2}	124
FeCo-Ni_3S_4	3000	Negligible decay at 100 mA cm^{-2}	60
Co_2P/Mo_2C@NC	3000	Negligible decay at 90 mA cm^{-2}	121
Mn_6-CoO	3000	13 mV decay	31
$Co_2N_{0.67}$/$CoMoO_4$	3000	Negligible decay	20
Ni/CeO_2@N-CNFs	3000	Negligible decay at 60 mA cm^{-2}	42
Ni_2P-Fe_2P	3000	Negligible decay at 1000 mA cm^{-2}	19
(Ni-Fe)S_x/NiFe$(OH)_y$	3000	Negligible decay at 100 mA cm^{-2}	69
c-NiFe/a-NiFeOOH@NiMo	2000	Negligible decay at 10 mA cm^{-2}	11
Ni-$FePS_3$	2000	Negligible decay at 100 mA cm^{-2}	71
Fe@Co/Se_2	2000	Negligible decay at 10 mA cm^{-2}	77
Ni_3S_2/$FeNi_2S_4$	2000	Negligible decay at 300 mA cm^{-2}	66
Mo_2C-CoO@NC	2000	Negligible decay at 75 mA cm^{-2}	120
FeOOH@NiFe LDH	1000	Negligible decay at 300 mA cm^{-2}	53
C/O-FeNi/FeF_2	1000	Negligible decay at 50 mA cm^{-2}	131
f-$Ni_{0.1}Co_{0.9}O_x$	1000	Slight decay at 100 mA cm^{-2}	35
FeNiOH	1000	Negligible decay at 90 mA cm^{-2}	44
Ni_5P_4@FeP	1000	Negligible decay at 350 mA cm^{-2}	90
Co_3O_4 SS Mesh/$ZnO^{0.1\ M\ KOH}$	1000	Negligible decay at 10 mA cm^{-2}	37
$CoP/FeOOH^{Electrolyte\ NA}$	1000	Slight decay at 90 mA cm^{-2}	104
S-Co_2P@Ni_2P	1000	Negligible decay at 600 mA cm^{-2}	87
S-NiFeP-10	1000	Negligible decay	91
Hea-d48h	1000	Negligible decay at 125 mA cm^{-2}	125
Zn-Fe/Mn@Mn-FeP	1000	Negligible decay at 150 mA cm^{-2}	28
Fe-NiS-NiS_2	1000	Negligible decay at 350 mA cm^{-2}	62
Fe,Ce-Ni_xS_y	1000	Negligible decay at 225 mA cm^{-2}	61
Co/Mo_2C@C	1000	Negligible decay at 10 mA cm^{-2}	118
Co-Ni_3S_2	1000	Negligible decay at 1000 mA cm^{-2}	59
NiMoB hollow foam	500	Negligible decay at 600 mA cm^{-2}	8

[a] NA: not applicable; CNTs: carbon nanotubes; LDH: layered double hydroxide; N-CNFs: N-doped carbon nanofibers; c-NiFe/a-NiFeOOH@NiMo: crystalline-NiFe/amorphous-NiFeOOH@NiMo; hea-d48h: it is a high-entropy alloy (hea), which is de-alloyed for 48 h, where the $Ni_{30}Co_{30}Cr_{10}Fe_{10}Al_{18}W_2$ high-entropy alloy comprises FCC and ordered aluminum-enriched BCC phases, while three dimensional porous architecture is constructed by de-alloying (selective etching of the BCC phase) the high-entropy alloy for 48 h; Gr: graphene.

transfer resistance for the HER than NiSi nanowires. SAE_{OER}-ECT-NiSi exhibits higher activity, higher electrochemical surface area, and lower charge transfer resistance for the OER than NiSi nanowires. The NiSi with a core–shell structure is formed by the ECT process of the NiSi nanowires, where the intact core is surrounded by an amorphous shell dispersed with nanoparticles. The SAE_{HER}-ECT-NiSi contains oxidized Ni, metallic Ni, oxidized Si, and metallic Si, which is almost similar to that of ECT-NiSi. In contrast, the self-adaptive evolution on ECT-NiSi under HER conditions increases the oxygen vacancies. In the high-resolution Ni 2p, Si 2p, and O 1s XPS spectra of SAE_{OER}-ECT-NiSi, a considerable decrease in the metallic Ni and Si peak intensities, an increase in the oxidized Ni and Si peak intensities, and an increase in the peak intensity for oxygen vacancies are observed, when compared to those of ECT-NiSi. At the same time, the formation of the $Ni(OH)_2$ phase is also observed in SAE_{OER}-ECT-NiS. Tables 1 and 2 provide the overpotential to achieve -10 mA cm^{-2} for the HER of various reported noble metal-free electrocatalysts in alkaline electrolytes. Tables 3 and 4 provide the long-term stability of various reported noble metal-free electrocatalysts for the HER in alkaline electrolytes. Table 5 provides the durability of various reported noble metal-free electrocatalysts for the HER in alkaline electrolytes. Tables 6 and 7 provide the overpotential to achieve 10 mA cm^{-2} for the OER of various reported noble metal-free electrocatalysts in alkaline electrolytes. Tables 8 and 9 provide the long-term stability of various reported noble metal-free electrocatalysts for the OER in alkaline electrolytes. Table 10 provides the durability of various

Table 11 Potential (Part 1: potential from 1.42 to 1.55 V) to achieve 10 mA cm^{-2} for overall water splitting of different kinds of reported non-noble metal bifunctional electrocatalysts in an alkaline electrolyte[a]

Bifunctional electrocatalysts for the HER and OER	Overall water splitting (V at 10 mA cm^{-2})	Electrolyte	Ref.
FeP/Ni_2P	1.42	1 M KOH	18
NiMoB hollow foam	1.431	1 M KOH	8
c-NiFe/a-NiFeOOH@NiMo	1.45	1 M KOH	11
Ni-C hnsa	~1.45[b]	1 M KOH	111
$Sn\text{-}Ni_3S_2$	1.46	1 M KOH	14
$(Ni\text{-}Fe)S_x/NiFe(OH)_y$	1.46	1 M KOH	69
NiCoP	1.48	1 M KOH	83
NiFeLa LDH/v-MXene	1.48	1 M KOH	57
$Mn_1Ni_1Co_1$-P	1.48	1 M KOH	10
$Gr\text{-}CNTs\text{-}Sn_4P_3$	1.482	1 M KOH	12
Co_3O_4	1.483	1 M KOH	29
$^{nb}Fe\text{-}VSB/NiPO\text{-}500^{OER}//VSB/NiPO^{HER}$	1.487	1 M KOH	105
MH-TMO	1.49	1 M KOH	1g
$WCoSe/WCo_3O_4$	1.49	1 M KOH	78
Fe-CoP	1.49	1 M KOH	85
$^{nb}c\text{-}CoFeP/a\text{-}CoFe\ LDH^{OER}//c\text{-}CoMnP/a\text{-}CoMn\ LDH^{HER}$	1.498	1 M KOH	56
$^{nb}S\text{-}NiFeP\text{-}10^{OER}//S\text{-}NiFeP\text{-}20^{HER}$	1.5	1 M KOH	91
NiS/MoS_2	1.51	1 M KOH	64
$NiP_2/NbP@CNTs$	1.51	1 M KOH	96
$^{nb}OR\text{-}NiOOH^{OER}//HR\text{-}NiMoO@Ni^{HER}$	1.51	1 M KOH	38
$Fe@Co/Se_2$	1.51	1 M KOH	77
$^{nb}act\text{-}modified\text{-}ZIF\text{-}67^{OER}//M\text{-}Co\text{-}CN^{HER}$	1.51	1 M KOH	114
Mn_6-CoO	1.52	1 M KOH	31
$S\text{-}Co_2P@Ni_2P$	1.52	1 M KOH	87
$Fe_2P\text{-}CoP/CeO_2$	1.52	1 M KOH	101
1T Co-$WS_2/NiTe_2$/Ni	1.521	1 M KOH	73
$Ni_xS_y@MnO_xH_y$	1.53	1 M KOH	68
$^{nb}CuNCo_3{}^{OER}//CoN_{0.73}Co_3{}^{HER}$	1.53	1 M KOH	107
CoN@NC	1.53	1 M KOH	106
$Co_{0.21}Fe_{0.28}(OH)F$	1.53	1 M KOH	130
$P\text{-}CoMoO_4$	1.54	1 M KOH	40
NiCoFe-P/C	1.55	1 M KOH	93
$Co_2P/Mo_2C@NC$	1.55	1 M KOH	121
$Ni_3S_2/FeNi_2S_4$	1.55	1 M KOH	66

[a] nb: non-bifunctional electrocatalyst; c-NiFe/a-NiFeOOH@NiMo: crystalline-NiFe/amorphous-NiFeOOH@NiMo; CNTs: carbon nanotubes; LDH: layered double hydroxide; c-CoMnP/a-CoMn LDH: crystalline CoMnP decorated amorphous CoMn LDH; c-CoFeP/a-CoFe LDH: crystalline CoFeP decorated amorphous CoFe LDH; VSB/NiPO: nickel phosphate microprism, where the microprism is mainly composed of Versailles-Santa Barbara-5, which is a kind of nickel phosphate molecular sieve having the chemical formula of $Ni_{20}[(OH)_{12}(H_2O)_6][(HPO_4)_8(PO_4)_4]\cdot 12H_2O$; MH-TMO: mesoporous and heterostructured transition metal oxides; M-Co-CN: it was synthesized by the heat treatment of modified-ZIF-67 followed by acid treatment, where ZIF-67 represents the Co-based zeolitic imidazolate framework; act-modified-ZIF-67: activated modified Co-based zeolitic imidazolate framework; hnsa: hybrid nanosheet array; Gr: graphene. [b] ~1.45 V at 50 mA cm^{-2}.

Table 12 Potential (Part 2: potential from 1.56 to 1.87 V) to achieve 10 mA cm^{-2} for overall water splitting of different kinds of reported non-noble metal bifunctional electrocatalysts in an alkaline electrolyte[a]

Bifunctional electrocatalysts for the HER and OER	Overall water splitting (V at 10 mA cm^{-2})	Electrolyte	Ref.
Ni/CeO_2@N-CNFs	1.56	1 M KOH	42
Fe,Ce-Ni_xS_y	1.56	1 M KOH	61
Mo_2C-CoO@NC	1.56	1 M KOH	120
Ni_2P-Fe_2P	1.561	1 M KOH	19
LSC-N-GQDs-$MoSe_2$	~1.57	1 M KOH	80
W-NiS_2/MoO_2	1.57	1 M KOH	63
CoP-NC@NiFeP	1.57	1 M KOH	98
Cu_3P-Cu_2O/NPC	1.57	1 M KOH	100
Co-Ni_3S_2	1.58	1 M KOH	59
Fe-NiS-NiS_2	1.59	1 M KOH	62
^{nb}act-Ni-CoP/Co_2P@NC^{OER}//Ni-CoP/Co_2P@NC^{HER}	1.59	1 M KOH	97
Co/Mo_2C@C	1.59	1 M KOH	118
Hea-d48h	1.615	1 M KOH	125
$^{nb}SAE_{OER}$-ECT-$NiSi^{OER}$//SAE_{HER}-ECT-$NiSi^{HER}$	1.63[b]	1 M KOH	132
^{nb}Fe/Mo_2C-NC^{OER}//Ni/Mo_2C-NC^{HER}	1.66[c]	1 M KOH	117
$Ni_3Fe_{0.75}V_{0.25}$/$Ni_3Fe_{0.75}V_{0.25}N$	1.66	1 M KOH	129
Ni_3S_2-MoS_2	1.67	1 M KOH	65
Ce@NiCo LDH	1.68	1 M KOH	55
Co-Mn-CO_3-OH	1.68	1 M KOH	48
MoO_2/Co	1.683	1 M KOH	30
Ni-$FePS_3$	1.71	1 M KOH	71
$Co_2N_{0.67}$/$CoMoO_4$	1.71[d]	1 M KOH	20
Fe_2P/Co@NPC	1.73	1 M KOH	6e
e-FeCoNiCu-P	1.738[e]	1 M KOH	89
CoNiP	~1.76[f]	1 M KOH	84
Zn-Fe/Mn@Mn-FeP	1.79[g]	1 M KOH	28
^{nb}NiFe LDH^{OER}//Ni_2P^{HER}	~1.8[h]	1 M KOH	82
Ni/MoO_2@CN	1.83[i]	1 M KOH	15
Co-Ni_3S_2	1.87[j]	1 M NaOH	58

[a] nb: non-bifunctional electrocatalyst; N-CNFs: N-doped carbon nanofibers; LDH: layered double hydroxide; e-FeCoNiCu-P: electrochemically etched FeCoNiCu-P; LSC/LSCO: $La_{0.5}Sr_{0.5}CoO_{3-\delta}$; N-GQDs: N-doped graphene quantum dots; hea-d48h: it is a high-entropy alloy (hea), which is de-alloyed for 48 h, where the $Ni_{30}Co_{30}Cr_{10}Fe_{10}Al_{18}W_2$ high-entropy alloy comprises FCC and ordered aluminum-enriched BCC phases, while three dimensional porous architecture is constructed by de-alloying (selective etching of the BCC phase) the high-entropy alloy for 48 h; SAE_{HER}-ECT-NiSi: NiSi is subjected to ECT followed by SAE_{HER}, where ECT is an electrochemical tuning process comprising lithiation and rapid delithiation of NiSi, while SAE_{HER} is a self-adaptive evolution that involves conducting multiple linear sweep voltammetry on ECT-NiSi under HER conditions; SAE_{OER}-ECT-NiSi: NiSi is subjected to ECT followed by SAE_{OER}, where ECT is an electrochemical tuning process comprising lithiation and rapid delithiation of NiSi, while SAE_{OER} is a self-adaptive evolution that involves conducting multiple linear sweep voltammetry on ECT-NiSi under OER conditions; act-Ni-CoP/Co_2P@NC: activated Ni-CoP/Co_2P@NC. [b] 1.63 V at 100 mA cm^{-2}. [c] 1.66 V at 100 mA cm^{-2}. [d] 1.71 V at 100 mA cm^{-2}. [e] 1.738 V at 100 mA cm^{-2}. [f] ~1.76 V at 20 mA cm^{-2}. [g] 1.79 V at 50 mA cm^{-2}. [h] ~1.8 V at 250 mA cm^{-2}. [i] 1.83 V at 200 mA cm^{-2}. [j] 1.87 V at 20 mA cm^{-2}.

reported noble-metal-free electrocatalysts for the OER in alkaline electrolytes. Tables 11 and 12 provide the potential to achieve 10 mA cm^{-2} for overall water splitting of different kinds of reported noble-metal-free bifunctional electrocatalysts in alkaline electrolytes. Tables 13 and 14 provide the long-term stability of various reported noble-metal-free electrocatalysts for overall water splitting in alkaline electrolytes. Table 15 provides the overpotential to achieve −1000 mA cm^{-2} for the HER of various reported noble-metal-free electrocatalysts in alkaline electrolytes. Table 16 provides the overpotential to achieve 1000 mA cm^{-2} for the OER of various reported noble-metal-free electrocatalysts in alkaline electrolytes. Table 17 provides the potential to achieve 1000 mA cm^{-2} for overall water splitting of different kinds of reported noble-metal-free bifunctional electrocatalysts in alkaline electrolytes.

3 Summary and outlook

One of the promising approaches for generating hydrogen is electrochemical water splitting. At the same time, efficient water-splitting can be achieved by developing noble metal-free electrocatalysts for the oxygen evolution reaction (OER) and hydrogen evolution reaction (HER). The activity, stability, and durability of several kinds of recently reported noble

Table 13 Long-term stability (Part 1: 50 h to 500 h of duration) of various reported noble metal-free electrocatalysts for overall water splitting in 1 M KOH alkaline electrolyte[a]

Bifunctional electrocatalysts for the HER and OER	Chr amp	Chr pot	Dur (h)	Remark after the stability test	Ref.
^{nb}OR-NiOOH^{OER}//HR-NiMoO@Ni^{HER}	NA	Yes	500	Reasonable stability at a CD of 1000 A m^{-2}	38
NiFeLa LDH/v-MXene	NA	Yes	400	Negligible decay at a CD of 100 mA cm^{-2}	57
^{nb}act-Ni-CoP/Co_2P@NC^{OER}//Ni-CoP/Co_2P@NC^{HER}	Yes	NA	400	Negligible decay at a potential of 1.6 V	97
Ni/MoO_2@CN	NA	Yes	300	Negligible decay at a CD of 1000 mA cm^{-2}	15
Cu_3P-Cu_2O/NPC	Yes	NA	168	98.19% retention at a potential of 1.7 V	100
Ni_xS_y@MnO_xH_y	NA	Yes	100	Negligible decay at a CD of 100 mA cm^{-2}	68
c-NiFe/a-NiFeOOH@NiMo	NA	Yes	100	95.86% retention at a CD of 100 mA cm^{-2}	11
^{nb}Fe-VSB/NiPO-500^{OER}//VSB/NiPO^{HER}	NA	Yes	100	96.44% retention at a CD of 100 mA cm^{-2}	105
MH-TMO	NA	Yes	100	Negligible decay at a CD of 10 mA cm^{-2}	1g
Hea-d48h	Yes	NA	100	99.13% retention	125
Ni/CeO_2@N-CNFs	Yes	NA	100	Negligible decay	42
WCoSe/WCo_3O_4	NA	Yes	100	Reasonable stability at a CD of 100 mA cm^{-2}	78
^{nb}act-modified-ZIF-67^{OER}//M-Co-CN^{HER}	NA	Yes	100	93.7% retention at a CD of 20 mA cm^{-2}	114
Fe,Ce-Ni_xS_y	NA	Yes	90	Reasonable stability at a CD of 20 mA cm^{-2}	61
^{nb}c-CoFeP/a-CoFe LDH^{OER}//c-CoMnP/a-CoMn LDH^{HER}	NA	Yes	85	29.1 mV decay at a CD of 100 mA cm^{-2}	56
Zn-Fe/Mn@Mn-FeP	NA	Yes	80	Reasonable stability at a CD of 50 mA cm^{-2}	28
P-$CoMoO_4$	NA	Yes	72	Negligible decay at a CD of 50 mA cm^{-2}	40
Sn-Ni_3S_2	Yes	NA	~70	Negligible decay at a potential of 2.26 V	14
Gr-CNTs-Sn_4P_3	Yes	NA	65	96% retention at a potential of 1.482 V	12
Fe_2P/Co@NPC	NA	Yes	60	Reasonable stability at a CD of 10 mA cm^{-2}	6e
^{nb}SAE_{OER}-ECT-NiSi^{OER}//SAE_{HER}-ECT-NiSi^{HER}	Yes	NA	55	Negligible decay at a potential of 1.75 V	132
NiS/MoS_2	Yes	NA	50	99.2% retention	64
NiP_2/NbP@CNTs	Yes	NA	50	Negligible decay	96
$Co_2N_{0.67}$/$CoMoO_4$	NA	Yes	50	Reasonable stability at a CD of 500 mA cm^{-2}	20
$Mn_1Ni_1Co_1$-P	Yes	NA	50	96% retention at a potential of 1.48 V	10
Ni_3S_2/$FeNi_2S_4$	Yes	NA	50	Negligible decay at a potential of 2 V	66
Fe-CoP	NA	Yes	50	Negligible decay at a CD of 10 mA cm^{-2}	85

[a] Ref.: references; Dur: duration of the stability test; Chr pot: chronopotentiometry; Chr amp: chronoamperometry; NA: not applicable; CD: current density; c-NiFe/a-NiFeOOH@NiMo: crystalline-NiFe/amorphous-NiFeOOH@NiMo; CNTs: carbon nanotubes; LDH: layered double hydroxide; c-CoMnP/a-CoMn LDH: crystalline CoMnP decorated amorphous CoMn LDH; c-CoFeP/a-CoFe LDH: crystalline CoFeP decorated amorphous CoFe LDH; VSB/NiPO: nickel phosphate microprism, where the microprism is mainly composed of Versailles-Santa Barbara-5, which is a kind of nickel phosphate molecular sieve having the chemical formula of $Ni_{20}[(OH)_{12}(H_2O)_6][(HPO_4)_8(PO_4)_4]\cdot 12H_2O$; MH-TMO: mesoporous and heterostructured transition metal oxides; hea-d48h: it is a high-entropy alloy (hea), which is de-alloyed for 48 h, where the $Ni_{30}Co_{30}Cr_{10}Fe_{10}Al_{18}W_2$ high-entropy alloy comprises FCC and ordered aluminum-enriched BCC phases, while three dimensional porous architecture is constructed by de-alloying (selective etching of the BCC phase) the high-entropy alloy for 48 h; SAE_{HER}-ECT-NiSi: NiSi is subjected to ECT followed by SAE_{HER}, where ECT is an electrochemical tuning process comprising lithiation and rapid delithiation of NiSi, while SAE_{HER} is a self-adaptive evolution that involves conducting multiple linear sweep voltammetry on ECT-NiSi under HER conditions; SAE_{OER}-ECT-NiSi: NiSi is subjected to ECT followed by SAE_{OER}, where ECT is an electrochemical tuning process comprising lithiation and rapid delithiation of NiSi, while SAE_{OER} is a self-adaptive evolution that involves conducting multiple linear sweep voltammetry on ECT-NiSi under OER conditions; N-CNFs: N-doped carbon nanofibers; act-Ni-CoP/Co_2P@NC: activated Ni-CoP/Co_2P@NC; M-Co-CN: it was synthesized by the heat treatment of modified-ZIF-67 followed by acid treatment, where ZIF-67 represents the Co-based zeolitic imidazolate framework; act-modified-ZIF-67: activated modified Co-based zeolitic imidazolate framework; Gr: graphene; nb: non-bifunctional electrocatalyst.

metal-free electrocatalysts such as oxides/hydroxides/(oxy) hydroxides/layered double hydroxides, sulfides, selenides, phosphides/phosphates, nitrides, carbon-based electrocatalysts, and alloy/B/V/F/Si based electrocatalysts for the HER and OER in an alkaline environment have been reviewed in this paper. In addition, this paper reviews the strategies used to achieve high activity and stability/durability, including at a high current density of ≥1000 mA cm^{-2} of noble metal-free electrocatalysts for the HER and OER in an alkaline environment.

The following several promising strategies have been used for the noble metal-free electrocatalysts to attain enhanced performance for the HER and/or OER in alkaline environments (Fig. 9):

(a) Fabricating oxide based noble metal-free electrocatalysts enhanced the performance for the HER and OER, while various strategies including preparing ultrathin/nanostructures, creating oxygen vacancies, creating heterojunctions, doping of metals/non-metals, preparing transition bimetallic oxide based catalysts, facet engineering, creating high valence ions,

Table 14 Long-term stability (Part 1: 12 h to 48 h of duration) of various reported noble metal-free electrocatalysts for overall water splitting in 1 M KOH alkaline electrolyte, where the electrolyte other than 1 M KOH is indicated on the electrocatalyst[a]

Bifunctional electrocatalysts for the HER and OER	Chr amp	Chr pot	Dur (h)	Remark after the stability test	Ref.
1T Co-WS_2/$NiTe_2$/Ni	Yes	NA	48	94% retention	73
$^{nb}CuNCo_3{}^{OER}$//$CoN_{0.73}Co_3{}^{HER}$	Yes	NA	48	90% retention	107
Co/Mo_2C@C	Yes	NA	48	90.2% retention at a potential of 1.59 V	118
$Ni_3Fe_{0.75}V_{0.25}$/$Ni_3Fe_{0.75}V_{0.25}N$	Yes	NA	40	Reasonable stability at a potential of 2 V	129
CoP-NC@NiFeP	NA	Yes	40	Reasonable stability at a CD of 50 mA cm^{-2}	98
Fe_2P-CoP/CeO_2	NA	Yes	40	Reasonable stability at a CD of 500 mA cm^{-2}	101
Ni_2P-Fe_2P	NA	Yes	>40	Reasonable stability at a CD of 500 mA cm^{-2}	19
FeP/Ni_2P	NA	Yes	>40	Negligible decay at a CD of 500 mA cm^{-2}	18
Ce@NiCo LDH	Yes	NA	36	Reasonable stability at a potential of 1.68 V	55
Co_2P/Mo_2C@NC	Yes	NA	30	Negligible decay	121
Fe@Co/Se_2	NA	Yes	30	Negligible decay at a CD of 10 mA cm^{-2}	77
Co-Ni_3S_2	Yes	NA	30	Negligible decay at a potential of 1.58 V	59
Mn_6-CoO	NA	Yes	28	Reasonable stability at a CD of 10 mA cm^{-2}	31
CoN@NC	NA	Yes	25	Reasonable stability at a CD of 10 mA cm^{-2}	106
Mo_2C-CoO@NC	Yes	NA	>25	Reasonable stability at a potential of 1.9 V	120
NiCoFe-P/C	Yes	NA	24	Reasonable stability	93
e-FeCoNiCu-P	NA	Yes	24	Negligible decay at a CD of 100 mA cm^{-2}	89
LSC-N-GQDs-$MoSe_2$	NA	Yes	24	Negligible decay at a CD of 500 mA cm^{-2}	80
^{nb}S-NiFeP-10^{OER}//S-NiFeP-20^{HER}	Yes	NA	24	Reasonable stability at a potential of 1.5 V	91
Co-$Ni_3S_2{}^{1\ M\ NaOH}$	NA	Yes	24	Negligible decay	58
^{nb}Fe/Mo_2C-NC^{OER}//Ni/Mo_2C-NC^{HER}	Yes	NA	24	Reasonable stability at a potential of 1.66 V	117
$Co_{0.21}Fe_{0.28}$(OH)F	NA	Yes	20	Negligible decay at a CD of 20 mA cm^{-2}	130
NiMoB hollow foam	NA	Yes	20	Reasonable stability at a CD of 5000 mA cm^{-2}	8
^{nb}NiFe LDH^{OER}//Ni_2P^{HER}	Yes	NA	>15	Reasonable stability at a potential of 2.1 V	82
NiCoP	Yes	NA	12	98% retention	83
Fe-NiS-NiS_2	Yes	NA	12	Reasonable stability at a potential of 1.59 V	62
Co-Mn-CO_3-OH	NA	Yes	>12	Negligible decay at a CD of 10 mA cm^{-2}	48

[a] nb: non-bifunctional electrocatalyst; Ref.: references; Dur: duration of the stability test; Chr pot: chronopotentiometry; Chr amp: chronoamperometry; NA: not applicable; CD: current density; LDH: layered double hydroxide; e-FeCoNiCu-P: electrochemically etched FeCoNiCu-P; LSC/LSCO: $La_{0.5}Sr_{0.5}CoO_{3-\delta}$; N-GQDs: N-doped graphene quantum dots.

Table 15 Overpotential (η) to achieve −1000 mA cm^{-2} for the hydrogen evolution reaction (HER) of various reported noble metal-free electrocatalysts in an alkaline electrolyte[a]

HER electrocatalysts	η at −1000 mA cm^{-2} (mV)	Electrolyte	Ref.
MoS_2/Mo_2C	−220	1 M KOH	21
C-$Ni_{1-x}O$/3D printed Ni	−245	1 M KOH	16
Fe-Co-CO_3-OH	−256	1 M KOH	17
Ni/MoO_2@CN	−267	1 M KOH	15
FeP/Ni_2P	∼−270	1 M KOH	18
$Ni_{2(1-x)}Mo_{2x}P$	−294	1 M KOH	86
Ni_2P	−306	1 M KOH	82
HR-NiMoO@Ni	−308	1 M KOH	38
Mo_5N_6-MoS_2-HCNRs	−315	1 M KOH	108
$Co_2N_{0.67}$/$CoMoO_4$	−315	1 M KOH	20
Ni_2P-Fe_2P	−333	1 M KOH	19
NiP_2-FeP_2@Cu nanoarray	−357	1 M KOH	13
NiMoB hollow foam	∼−420	1 M KOH	8
Sn-Ni_3S_2	−570	1 M KOH	14
Co-Ni_3S_2	−850	1 M KOH	59

[a] HCNRs: hollow carbon nanoribbons.

integrating with carbon, designing the facile synthesis route, and utilization of waste enhanced the performance.[1g,15-16,27,29-42]

(b) Fabricating hydroxide based noble metal-free electrocatalysts enhanced the performance for the HER and OER, while various strategies including preparing nanostructures, preparing transition bimetallic carbonate hydroxides, increasing the conductivity and electrochemical surface area, creating abundant oxygen vacancies, doping of metals, and developing facile synthesis routes at ambient temperature enhanced the performance.[17,26,43–48]

(c) Fabricating (oxy)hydroxide based noble metal-free electrocatalysts enhanced the performance for the HER and OER, while various strategies including creating abundant defects, generating multiple vacancies, doping of elements, developing NiFe based catalysts, and developing facile synthesis routes enhanced the performance.[6a,11,24,49-50]

(d) Fabricating layered double hydroxide based noble metal-free electrocatalysts enhanced the performance for the HER and OER, while various strategies including electrochemical activation, doping of metals, preparing heterostructures, integrating with MXene/metal nanoparticles and developing facile synthesis routes enhanced the performance.[25,51–57]

Table 16 Overpotential (η) to achieve 1000 mA cm^{-2} for the oxygen evolution reaction (OER) of various reported noble metal-free electrocatalysts in an alkaline electrolyte (η to achieve greater than 1000 mA cm^{-2} is mentioned on the η, which is described in the footnote of this table)[a]

OER electrocatalysts	η at 1000 mA cm^{-2} (mV)	Electrolyte	Ref.
FeP/Ni_2P	293	1 M KOH	18
Fe-Co-CO_3-OH	308	1 M KOH	17
Ni_2P-Fe_2P	337	1 M KOH	19
OR-NiOOH	358	1 M KOH	38
KT-Ni(0)@Ni(II)-TPA	380[b]	1 M KOH	112
Ni/MoO_2@CN	420	1 M KOH	15
C-$Ni_{1-x}O$/3D printed Ni	425	1 M KOH	16
Fe-CoP	428	1 M KOH	85
NiMoB hollow foam	~460	1 M KOH	8
Co-Mn-CO_3-OH	462	1 M KOH	48
(Ni-Fe)S_x/NiFe(OH)$_y$	~510	1 M KOH	69
CuS-Ni_3S_2/CuNi	510	1 M KOH	22
Sn-Ni_3S_2	580	1 M KOH	14
Co-Ni_3S_2	750	1 M KOH	59
Ce-NiFe	~770	1 M KOH	47

[a] η: overpotential; KT-Ni(0)@Ni(II)-TPA: a terephthalic acid (TPA)-regulated etching strategy is used for the preparation of a karst topography (KT) featured electrode containing core–shell structured Ni(0)@Ni(II)-TPA. [b] 380 mV at 1500 mA cm^{-2}.

Table 17 Potential to achieve 1000 mA cm^{-2} for overall water splitting of different kinds of reported non-noble metal bifunctional electrocatalysts in alkaline electrolyte[a]

Bifunctional electrocatalysts for the HER and OER	Overall water splitting (V at 1000 mA cm^{-2})	Electrolyte	Ref.
FeP/Ni_2P	~1.78	1 M KOH	18
Ni_2P-Fe_2P	~1.98	1 M KOH	19
$Co_2N_{0.67}$/$CoMoO_4$	1.98	1 M KOH	20
Ni/MoO_2@CN	2.02	1 M KOH	15
^{nb}NiFe LDH^{OER}//Ni_2P^{HER}	~2.05	1 M KOH	82
Sn-Ni_3S_2	~2.65	1 M KOH	14
NiMoB hollow foam	~3.8	1 M KOH	8

[a] nb: non-bifunctional electrocatalyst.

(e) Fabricating sulfide based noble metal-free electrocatalysts enhanced the performance for the HER and OER, while various strategies including preparing ultrathin/nanostructures, preparing amorphous sulfide based catalysts, doping of metals, preparing heterojunctions/heterostructures, creating super-aerophobic surfaces, creating high valence state sites, creating abundant bridging S_2^{2-} sites, and developing facile synthesis routes enhanced the performance.[14,22,58–75]

(f) Fabricating selenide based noble metal-free electrocatalysts enhanced the performance for the HER and OER, while various strategies including preparing nanostructures, creating heterostructures, doping of metals, and activation of the inert basal plane enhanced the performance.[9,76–81]

(g) Fabricating phosphide/phosphate based noble metal-free electrocatalysts enhanced the performance for the HER and OER, while various strategies including preparing nanostructures/nanoporous, creating heterostructures/core–shell structures, integrating with carbon, preparing bimetallic/trimetallic, increasing the conductivity and electrochemical surface area, creating superaerophobic surfaces, and developing facile and scalable synthesis routes enhanced the performance.[6e,10,13,18-19,28,82-93,95-105]

(h) Fabricating nitride based noble metal-free electrocatalysts enhanced the performance for the HER and OER, while various strategies including preparing nanostructures/porous structures, doping of elements, and preparing heterojunctions/heterostructures enhanced the performance.[20,106–110]

(i) Fabricating carbon based noble metal-free electrocatalysts enhanced the performance for the HER and OER, while various strategies including creating nanostructures/porous structures/heterostructures/core–shell structures, creating superaerophobic surfaces, doping of elements, and creating abundant low-coordinate Co–N sites enhanced the performance.[21,111–121]

(j) Fabricating alloy/B/V/F/Si based noble metal-free electrocatalysts enhanced the performance for the HER and OER, while various strategies including preparing nanostructures/heterostructures/heterojunctions/hollow structures/ultrathin structures/porous structures/creating high valence sites, electrochemical activation, and designing facile synthesis routes enhanced the performance.[8,122–132]

The stage has been developed for the noble metal-free electrocatalysts for the HER and OER to afford superior performance in practical applications. Hence, the vital factors governing the performance of noble metal-free electrocatalysts should be considered in future research: (1) recently, some green chemistry approaches, including ambient temperature synthesis,[24–26] utilization of waste as a source,[27] and using relatively low-cost metals,[28] have been used for the fabrication of noble metal-free electrocatalysts for electrochemical water splitting. However, efficient green chemistry approaches for fabricating efficient noble metal-free electrocatalysts for the HER and OER are considerably limited. Hence, more progress is needed to construct efficient noble metal-free electrocatalysts for the HER and OER using various green chemistry approaches.

(2) Noble metal-free bifunctional electrocatalysts for overall water splitting exhibit low cell voltage at much higher current densities with high stability, which are substantially minimal. Therefore, additional progress is obviously needed to fulfill the requirement of industrial water electrolysis.

Strategies used to enhance the performance for HER and/or OER of noble-metal-free electrocatalysts

1. Oxide based electrocatalysts:
Preparing ultrathin/nanostructure, creating oxygen vacancies, creating heterojunction, doping of metal/non-metal, preparing transition bimetal based, facet engineering, creating high valance ions, integrating with carbon, designing the facile synthesis route, and utilization of waste.

2. Hydroxide based electrocatalysts:
Preparing nanostructure, preparing transition bimetallic carbonate hydroxides, increasing conductivity and electrochemical surface area, creating abundant oxygen vacancies, doping of metal, and developing facile synthesis route at ambient temperature.

3. (Oxy)hydroxide based electrocatalysts:
Creating abundant defects, generating multiple vacancies, doping of elements, developing NiFe based catalysts, and developing facile synthesis route.

4. Layered double hydroxide based electrocatalysts:
Electrochemical activation, doping of metal, preparing heterostructure, integrating with MXene/metal nanoparticles and developing facile synthesis route.

5. Sulfide based electrocatalysts:
Preparing ultrathin/nanostructure, preparing amorphous, doping of metal, preparing heterojunctions/heterostructure, creating super-aerophobic surface, creating high valence state sites, creating abundant bridging S_2^{2-} sites, and developing facile synthesis route.

6. Selenide based electrocatalysts:
Preparing nanostructure, creating heterostructure, doping of metals, and activation of the inert basal plane.

7. Phosphide/phosphate based electrocatalysts:
Preparing nanostructure/nanoporous, creating heterostructure/core-shell structure, integrating with carbon, preparing bimetallic/trimetallic, increasing conductivity and electrochemical surface area, creating superaerophobic surface, and developing facile and scalable synthesis route.

8. Nitride based electrocatalysts:
Preparing nanostructure/porous structure, doping of elements, and preparing heterojunction/heterostructure.

9. Carbon based electrocatalysts:
Creating nanostructure/porous structure/heterostructure/core-shell structure, creating superaerophobic surface, doping of elements, and creating abundant low-coordinate Co–N sites.

10. Alloy/B/V/F/Si based electrocatalysts:
Preparing nanostructure/heterostructure/heterojunction/hollow structure/ultrathin structure/porous structure/ creating high valence sites, electrochemical activation, and designing facile synthesis route.

Fig. 9 Strategies used to enhance the performance for the HER and/or OER of noble metal-free electrocatalysts.

Conflicts of interest

The authors declare that they have no known competing financial interests or personal relationships that could have appeared to influence the work reported in this paper.

Acknowledgements

The authors acknowledge financial support from the Research Grants Council of Hong Kong (Grant nos. CityU 21203518 and F-CityU106/18), Innovation and Technology Commission (Grant no. MHP/104/21), Shenzhen Science Technology and

Innovation Commission (Grant nos. JCYJ20210324125612035, R-IND12303, and R-IND12304), City University of Hong Kong (Grant no. 7005289, 7005580, 7005720, 9667213, 9667229, 9680331 and 9678291). The author M. I. J. thanks Dr Luo Yang, Dr Huang Chao, and Dr Wang Bin from the City University of Hong Kong. The author M.I.J. thanks Prof. Penghui Li, Shenzhen Institutes of Advanced Technology. DQH is thankful for the financial support from the Hong Kong SAR Government for the Postdoctoral Hub Program of the Innovation and Technology Fund (Project No. 9446002) under the STEM Professorship scheme.

References

1 (*a*) H.-Y. Wang, M.-L. Sun, J.-T. Ren and Z.-Y. Yuan, *Adv. Energy Mater.*, 2023, **13**, 2203568; (*b*) I. Roger, M. A. Shipman and M. D. Symes, *Nat. Rev. Chem*, 2017, **1**, 0003; (*c*) J. Guo, Y. Zheng, Z. Hu, C. Zheng, J. Mao, K. Du, M. Jaroniec, S.-Z. Qiao and T. Ling, *Nat. Energy*, 2023, **8**, 264–272; (*d*) W. Tong, M. Forster, F. Dionigi, S. Dresp, R. Sadeghi Erami, P. Strasser, A. J. Cowan and P. Farràs, *Nat. Energy*, 2020, **5**, 367–377; (*e*) Y. Tang, C. H. Mak, J. Zhang, G. Jia, K.-C. Cheng, H. Song, M. Yuan, S. Zhao, J.-J. Kai, J. C. Colmenares and H.-Y. Hsu, *Adv. Mater.*, 2023, **35**, 2207835; (*f*) Y. Tang, C. H. Mak, R. Liu, Z. Wang, L. Ji, H. Song, C. Tan, F. Barrière and H.-Y. Hsu, *Adv. Funct. Mater.*, 2020, **30**, 2006919; (*g*) F. Hu, D. Yu, M. Ye, H. Wang, Y. Hao, L. Wang, L. Li, X. Han and S. Peng, *Adv. Energy Mater.*, 2022, **12**, 2200067; (*h*) L. Yuan, C. Han, M.-Q. Yang and Y.-J. Xu, *Int. Rev. Phys. Chem.*, 2016, **35**, 1–36.

2 (*a*) J. A. Turner, *Science*, 2004, **305**, 972–974; (*b*) M. I. Jamesh, *J. Power Sources*, 2016, **333**, 213–236; (*c*) M.-I. Jamesh and X. Sun, *J. Power Sources*, 2018, **400**, 31–68; (*d*) J. Luo, J.-H. Im, M. T. Mayer, M. Schreier, M. K. Nazeeruddin, N.-G. Park, S. D. Tilley, H. J. Fan and M. Grätzel, *Science*, 2014, **345**, 1593–1596.

3 C. C. L. McCrory, S. Jung, I. M. Ferrer, S. M. Chatman, J. C. Peters and T. F. Jaramillo, *J. Am. Chem. Soc.*, 2015, **137**, 4347–4357.

4 L. C. Seitz, C. F. Dickens, K. Nishio, Y. Hikita, J. Montoya, A. Doyle, C. Kirk, A. Vojvodic, H. Y. Hwang, J. K. Norskov and T. F. Jaramillo, *Science*, 2016, **353**, 1011–1014.

5 M. I. Jamesh and M. Harb, *J. Energy Chem.*, 2021, **56**, 299–342.

6 (*a*) Z. Wei, M. Guo and Q. Zhang, *Appl. Catal., B*, 2023, **322**, 122101; (*b*) J. Sun, Z. Zhang and X. Meng, *Appl. Catal., B*, 2023, **331**, 122703; (*c*) X. Kang, F. Yang, Z. Zhang, H. Liu, S. Ge, S. Hu, S. Li, Y. Luo, Q. Yu, Z. Liu, Q. Wang, W. Ren, C. Sun, H.-M. Cheng and B. Liu, *Nat. Commun.*, 2023, **14**, 3607; (*d*) C. Huang, Q. Zhou, L. Yu, D. Duan, T. Cao, S. Qiu, Z. Wang, J. Guo, Y. Xie, L. Li and Y. Yu, *Adv. Energy Mater.*, 2023, **13**, 2301475; (*e*) Y. Bai, Y. Wang, Z. Qiao, Y. Yang, L. Deng, C. Li, X. Chen, S. Wang, Y. Huang, X. Zhang and D. Cao, *J. Mater. Chem. A*, 2022, **10**, 16037–16045.

7 (*a*) M.-I. Jamesh and M. Harb, *Mater. Sci. Energy Technol.*, 2020, **3**, 780–807; (*b*) M. I. Jamesh, *J. Power Sources*, 2020, **448**, 227375; (*c*) M.-I. Jamesh and X. Sun, *J. Energy Chem.*, 2019, **34**, 111–160; (*d*) M.-I. Jamesh, Y. Kuang and X. Sun, *ChemCatChem*, 2019, **11**, 1550–1575; (*e*) T. T. T. Toan, D. M. Nguyen, A. Q. Dao, V. T. Le and Y. Vasseghian, *Mol. Catal.*, 2023, **538**, 113001; (*f*) S.-H. Li, M.-Y. Qi, Z.-R. Tang and Y.-J. Xu, *Chem. Soc. Rev.*, 2021, **50**, 7539–7586; (*g*) K. Mensah-Darkwa, D. N. Ampong, E. A. Tsiwah, A. Kumar, M. A. Nartey, P. Aggrey, F. O. Agyemang and R. K. Gupta, *Mol. Catal.*, 2023, **547**, 113375; (*h*) R. Khosa, E. Pervaiz, U. Abdullah, M. Ali, U. Sohail and A. Shakoor, *Mol. Catal.*, 2022, **528**, 112514; (*i*) Y. Chen, J. Xu, M. Jiang, L. Wang, R. Ma, Y. Chen, Z.-H. Xie, P. Munroe, F. Hu, L. Li and S. Peng, *Adv. Energy Mater.*, 2024, **14**, 2303450; (*j*) Y. Ye, J. Xu, X. Li, Y. Jian, F. Xie, J. Chen, Y. Jin, X. Yu, M.-H. Lee, N. Wang, S. Sun and H. Meng, *Adv. Mater.*, 2024, 2312618; (*k*) H. Li, G. Yan, H. Zhao, P. C. Howlett, X. Wang and J. Fang, *Adv. Mater.*, 2024, 2311272; (*l*) G. Y. Jang, S. Kim, J. Choi, J. Park, S. An, J. Baek, Y. Li, T.-K. Liu, E. Kim, J. H. Lee, H. Wang, M. Kim, H.-S. Cho, X. Zheng, J. S. Yoo, K. Seo and J. H. Park, *Adv. Energy Mater.*, 2024, 2303924; (*m*) H. He, Q. Zhang, Z. Wang, S. Pan, Y. Zhao and X. Zhang, *Adv. Energy Mater.*, 2024, 2303713; (*n*) F. M. Yap, J. Y. Loh, S.-F. Ng and W.-J. Ong, *Adv. Energy Mater.*, 2024, 2303614; (*o*) H. Sun, B. Yao, Y. Han, L. Yang, Y. Zhao, S. Wang, C. Zhong, J. Chen, C.-P. Li and M. Du, *Adv. Energy Mater.*, 2024, 2303563; (*p*) J. Huang, N. Hales, A. H. Clark, N. S. Yüzbasi, C. N. Borca, T. Huthwelker, T. J. Schmidt and E. Fabbri, *Adv. Energy Mater.*, 2024, 2303529; (*q*) F. T. Haase, E. Ortega, S. Saddeler, F.-P. Schmidt, D. Cruz, F. Scholten, M. Rüscher, A. Martini, H. S. Jeon, A. Herzog, U. Hejral, E. M. Davis, J. Timoshenko, A. Knop-Gericke, T. Lunkenbein, S. Schulz, A. Bergmann and B. Roldan Cuenya, *Energy Environ. Sci.*, 2024, **17**, 2046–2058; (*r*) Y.-N. Zhou, F.-T. Li, B. Dong and Y.-M. Chai, *Energy Environ. Sci.*, 2024, **17**, 1468–1481; (*s*) C. Feng, Y. Zhou, M. Chen, L. Zou, X. Li, X. An, Q. Zhao, P. Xiaokaiti, A. Abudula, K. Yan and G. Guan, *Appl. Catal. B: Environ. Energy*, 2024, **349**, 123875; (*t*) X. Xiao, Y. Wei, S. Song, B. McElhenny, F. Zhang, X. Jiang, Y. Zhang, S. Chen, M. Wang, Y. Shen and Z. Ren, *Appl. Catal. B: Environ. Energy*, 2024, **349**, 123871; (*u*) F. Wang, X. Zhao, Y. Li, L. Liang, K. Sasaki, Q. Hao, W. Yuan, S. Li and H. Liu, *Appl. Catal. B: Environ. Energy*, 2024, **348**, 123830; (*v*) J.-T. Ren, L. Chen, H.-Y. Wang, W.-W. Tian, S.-X. Zhai, Y. Feng and Z.-Y. Yuan, *Appl. Catal. B: Environ. Energy*, 2024, **347**, 123817; (*w*) Z. Zhao, Z. Li, Z. Zhang and X. Meng, *Appl. Catal. B: Environ. Energy*, 2024, **347**, 123805; (*x*) Z. Zang, Y. Ren, C. Fan, Y. Cheng, L. Li, X. Yu, X. Yang, Z. Lu, X. Zhang and H. Liu, *Appl. Catal. B: Environ. Energy*, 2024, 123912.

8 H. Liu, X. Li, L. Chen, X. Zhu, P. Dong, M. O. L. Chee, M. Ye, Y. Guo and J. Shen, *Adv. Funct. Mater.*, 2022, **32**, 2107308.

9 S.-W. Kim, J.-K. Kim, H. J. Kim, C. T. Cao, N. Khen Oh, Y. Yang, H.-C. Song, M. Shim, H. S. Park and J. M. Baik, *Nano Energy*, 2022, **95**, 107023.
10 K. E. Salem, A. A. Saleh, G. E. Khedr, B. S. Shaheen and N. K. Allam, *Energy Environ. Mater.*, 2023, **6**, e12324.
11 Q. lv, B. Yao, W. Zhang, L. She, W. Ren, L. Hou, Y. Fautrelle, X. Lu, X. Yu and X. Li, *Chem. Eng. J.*, 2022, **446**, 137420.
12 S. Riyajuddin, M. Pahuja, P. K. Sachdeva, K. Azmi, S. Kumar, M. Afshan, F. Ali, J. Sultana, T. Maruyama, C. Bera and K. Ghosh, *ACS Nano*, 2022, **16**, 4861–4875.
13 A. Kumar, V. Q. Bui, J. Lee, A. R. Jadhav, Y. Hwang, M. G. Kim, Y. Kawazoe and H. Lee, *ACS Energy Lett.*, 2021, **6**, 354–363.
14 J. Jian, L. Yuan, H. Qi, X. Sun, L. Zhang, H. Li, H. Yuan and S. Feng, *ACS Appl. Mater. Interfaces*, 2018, **10**, 40568–40576.
15 G. Qian, J. Chen, T. Yu, J. Liu, L. Luo and S. Yin, *Nano-Micro Lett.*, 2022, **14**, 20.
16 T. Kou, S. Wang, R. Shi, T. Zhang, S. Chiovoloni, J. Q. Lu, W. Chen, M. A. Worsley, B. C. Wood, S. E. Baker, E. B. Duoss, R. Wu, C. Zhu and Y. Li, *Adv. Energy Mater.*, 2020, **10**, 2002955.
17 L. Hui, Y. Xue, D. Jia, H. Yu, C. Zhang and Y. Li, *Adv. Energy Mater.*, 2018, **8**, 1800175.
18 F. Yu, H. Zhou, Y. Huang, J. Sun, F. Qin, J. Bao, W. A. Goddard, S. Chen and Z. Ren, *Nat. Commun.*, 2018, **9**, 2551.
19 L. Wu, L. Yu, F. Zhang, B. McElhenny, D. Luo, A. Karim, S. Chen and Z. Ren, *Adv. Funct. Mater.*, 2021, **31**, 2006484.
20 Y. Hu, Z. Luo, M. Guo, J. Dong, P. Yan, C. Hu, T. T. Isimjan and X. Yang, *Chem. Eng. J.*, 2022, **435**, 134795.
21 Y. Luo, L. Tang, U. Khan, Q. Yu, H.-M. Cheng, X. Zou and B. Liu, *Nat. Commun.*, 2019, **10**, 269.
22 N. Zhang, Y. Gao, Y. Mei, J. Liu, W. Song and Y. Yu, *Inorg. Chem. Front.*, 2019, **6**, 293–302.
23 M.-I. Jamesh, A. Akila, D. Sudha, K. Gnana Priya, V. Sivaprakash and A. Revathi, *Sustainability*, 2022, **14**, 16359.
24 X. Chen, Q. Wang, Y. Cheng, H. Xing, J. Li, X. Zhu, L. Ma, Y. Li and D. Liu, *Adv. Funct. Mater.*, 2022, **32**, 2112674.
25 W. Zhao, H. Xu, H. Luan, N. Chen, P. Gong, K. Yao, Y. Shen and Y. Shao, *Adv. Energy Mater.*, 2022, **12**, 2102372.
26 S. Liu, G. Han, J. Zhang, H. Wang and X. Huang, *Chem. Eng. J.*, 2022, **428**, 130688.
27 K. Lu, Z. Wang, Y. Wu, X. Zhai, C. Wang, J. Li, Z. Wang, X. Li, Y. He, T. An, K. Yang, D. Yang, F. Yu and B. Dai, *Chem. Eng. J.*, 2023, **451**, 138590.
28 L. Huang, R. Yao, X. Wang, S. Sun, X. Zhu, X. Liu, M. G. Kim, J. Lian, F. Liu, Y. Li, H. Zong, S. Han and X. Ding, *Energy Environ. Sci.*, 2022, **15**, 2425–2434.
29 C. Chen, Z. Zhou, J. Liu, B. Zhu, H. Hu, Y. Yang, G. Chen, M. Gao and J. Zhang, *Appl. Catal., B*, 2022, **307**, 121209.
30 Y. Guo, X. Liu, Y. Zang, Y. Wu, Q. Zhang, Z. Wang, Y. Liu, Z. Zheng, H. Cheng, B. Huang, Y. Dai and P. Wang, *J. Mater. Chem. A*, 2022, **10**, 17297–17306.
31 H. Xue, A. Meng, T. Yang, Z. Li and C. Chen, *J. Energy Chem.*, 2022, **71**, 639–651.
32 B. J. Rani, A. Sivanantham, T. S. Shridharan, T. Runfa and I. S. Cho, *J. Mater. Chem. A*, 2022, **10**, 17710–17720.
33 Z. Wu, J. Mei, Q. Liu, S. Wang, W. Li, S. Xing, J. Bai, J. Yang, W. Luo, O. Guselnikova, A. P. O'Mullane, Y. Gu, Y. Yamauchi, T. Liao and Z. Sun, *J. Mater. Chem. A*, 2022, **10**, 808–817.
34 A. Malek, Y. Xue and X. Lu, *Angew. Chem., Int. Ed.*, 2023, **62**, e202309854.
35 X. Yu, C. Hu, P. Ji, Y. Ren, H. Zhao, G. Liu, R. Xu, X. Zhu, Z. Li, Y. Ma and L. Ma, *Appl. Catal., B*, 2022, **310**, 121301.
36 Y.-C. Zhang, C. Han, J. Gao, J. Wu, X.-D. Zhu and J.-J. Zou, *Chem. Eng. J.*, 2022, **446**, 137036.
37 K. R. Nandanapalli, D. Mudusu, R. Karuppannan, Y.-B. Hahn and S. Lee, *Chem. Eng. J.*, 2022, **429**, 132360.
38 J. Liu, W. Qiao, Z. Zhu, J. Hu and X. Xu, *Small*, 2022, **18**, 2202434.
39 H. Peng, K. Zhou, Y. Jin, Q. Zhang, J. Liu and H. Wang, *Chem. Eng. J.*, 2022, **429**, 132477.
40 J. Wang, J. Hu, C. Liang, L. Chang, Y. Du, X. Han, J. Sun and P. Xu, *Chem. Eng. J.*, 2022, **446**, 137094.
41 L. Wang, Y. Pan, D. Wu, X. Liu, L. Cao, W. Zhang, H. Chen, T. Liu, D. Liu, T. Chen, T. Ding, Y. Wang, C. Ding, C. Kang, C. Li, J. He and T. Yao, *J. Mater. Chem. A*, 2022, **10**, 20011–20017.
42 T. Li, J. Yin, D. Sun, M. Zhang, H. Pang, L. Xu, Y. Zhang, J. Yang, Y. Tang and J. Xue, *Small*, 2022, **18**, 2106592.
43 S. Tao, Q. Wen, W. Jaegermann and B. Kaiser, *ACS Catal.*, 2022, **12**, 1508–1519.
44 Z. Yin, R. He, Y. Zhang, L. Feng, X. Wu, T. Wågberg and G. Hu, *J. Energy Chem.*, 2022, **69**, 585–592.
45 Y. Zhuo, D. Liu, L. Qiao, S. Chen, J. Lu, W. F. IP, H. Pan and Z. Wang, *Adv. Energy Mater.*, 2023, **13**, 2301921.
46 X. Li, M. Hou, X. Qu, Y. Zhang and M. Li, *Small*, 2022, **18**, 2104863.
47 J. Liu, Y. Liu, X. Mu, H. Jang, Z. Lei, S. Jiao, P. Yan, M. G. Kim and R. Cao, *Adv. Funct. Mater.*, 2022, **32**, 2204086.
48 T. Tang, W.-J. Jiang, S. Niu, N. Liu, H. Luo, Y.-Y. Chen, S.-F. Jin, F. Gao, L.-J. Wan and J.-S. Hu, *J. Am. Chem. Soc.*, 2017, **139**, 8320–8328.
49 Y. Hu, J. Zhou, L. Li, Z. Hu, T. Yuan, C. Jing, R. Liu, S. Xi, H. Jiang, J.-Q. Wang and L. Zhang, *J. Mater. Chem. A*, 2022, **10**, 602–610.
50 S. Hou, L. Xu, X. Ding, R. M. Kluge, T. K. Sarpey, R. W. Haid, B. Garlyyev, S. Mukherjee, J. Warnan, M. Koch, S. Zhang, W. Li, A. S. Bandarenka and R. A. Fischer, *Angew. Chem., Int. Ed.*, 2022, **61**, e202201610.
51 I. B. Pehlivan, N. A. Saguì, J. Oscarsson, Z. Qiu, W. Zwaygardt, M. Lee, M. Mueller, S. Haas, L. Stolt, M. Edoff and T. Edvinsson, *J. Mater. Chem. A*, 2022, **10**, 12079–12091.
52 N. An, H. Tian, Y. Zhou, Y. Zou, H. Xiu, Y. Cao, Y. Wang, J. Li, D. Liu and Y. Kuang, *J. Energy Chem.*, 2022, **66**, 657–665.
53 Y. Li, Y. Wu, M. Yuan, H. Hao, Z. Lv, L. Xu and B. Wei, *Appl. Catal., B*, 2022, **318**, 121825.
54 L. Wu, J. Zhang, S. Wang, Q. Jiang, R. Feng, S. Ju, W. Zhang and F. Song, *Chem. Eng. J.*, 2022, **442**, 136168.

55 H. N. Dhandapani, D. Mahendiran, A. Karmakar, P. Devi, S. Nagappan, R. Madhu, K. Bera, P. Murugan, B. R. Babu and S. Kundu, *J. Mater. Chem. A*, 2022, **10**, 17488–17500.
56 K. Zheng, J. Ren, X. Li, G. Li, L. Jiao and C. Xu, *Chem. Eng. J.*, 2022, **441**, 136031.
57 M. Yu, J. Zheng and M. Guo, *J. Energy Chem.*, 2022, **70**, 472–479.
58 Y. Li, Y. Duan, K. Zhang and W. Yu, *Chem. Eng. J.*, 2022, **433**, 134472.
59 J. Jian, L. Yuan, H. Li, H. Liu, X. Zhang, X. Sun, H. Yuan and S. Feng, *Chem. Res. Chin. Univ.*, 2019, **35**, 179–185.
60 X. Mao, Y. Liu, Z. Chen, Y. Fan and P. Shen, *Chem. Eng. J.*, 2022, **427**, 130742.
61 X. Zhang, Y. Qiu, Q. Li, X. Ji and J. Liu, *J. Power Sources*, 2022, **522**, 231004.
62 S. Huang, Q. Zhang, P. Xin, J. Zhang, Q. Chen, J. Fu, Z. Jin, Q. Wang and Z. Hu, *Small*, 2022, **18**, 2106841.
63 S. L. Fereja, P. Li, Z. Zhang, J. Guo, Z. Fang, Z. Li, S. He and W. Chen, *Chem. Eng. J.*, 2022, **432**, 134274.
64 C. Gu, G. Zhou, J. Yang, H. Pang, M. Zhang, Q. Zhao, X. Gu, S. Tian, J. Zhang, L. Xu and Y. Tang, *Chem. Eng. J.*, 2022, **443**, 136321.
65 S. Yang, Y. Guo, Y. Zhao, L. Zhang, H. Shen, J. Wang, J. Li, C. Wu, W. Wang, Y. Cao, S. Zhuo, Q. Zhang and H. Zhang, *Small*, 2022, **18**, 2201306.
66 Y. Wu, Y. Li, M. Yuan, H. Hao, X. San, Z. Lv, L. Xu and B. Wei, *Chem. Eng. J.*, 2022, **427**, 131944.
67 M. Luo, S. Liu, W. Zhu, G. Ye, J. Wang and Z. He, *Chem. Eng. J.*, 2022, **428**, 131055.
68 P. Wang, Y. Luo, G. Zhang, Z. Chen, H. Ranganathan, S. Sun and Z. Shi, *Nano-Micro Lett.*, 2022, **14**, 120.
69 Q. Che, Q. Li, Y. Tan, X. Chen, X. Xu and Y. Chen, *Appl. Catal., B*, 2019, **246**, 337–348.
70 M. Lu, L. An, J. Yin, J. Jin, R. Yang, B. Huang, Y. Hu, Y.-Q. Zhao and P. Xi, *J. Mater. Chem. A*, 2022, **10**, 19757–19768.
71 C. Tang, D. He, N. Zhang, X. Song, S. Jia, Z. Ke, J. Liu, J. Wang, C. Jiang, Z. Wang, X. Huang and X. Xiao, *Energy Environ. Mater.*, 2022, **5**, 899–905.
72 H. Yang, P. Guo, R. Wang, Z. Chen, H. Xu, H. Pan, D. Sun, F. Fang and R. Wu, *Adv. Mater.*, 2022, **34**, 2107548.
73 D. R. Paudel, U. N. Pan, R. B. Ghising, P. P. Dhakal, V. A. Dinh, H. Wang, N. H. Kim and J. H. Lee, *Nano Energy*, 2022, **102**, 107712.
74 S. Li, Y. Liu, K. Feng, C. Li, J. Xu, C. Lu, H. Lin, Y. Feng, D. Ma and J. Zhong, *Angew. Chem., Int. Ed.*, 2023, **62**, e202308670.
75 S. Chandrasekaran, T. Ma, Z. Hu, Q. Liu, C. Zhan, Y. Li, C. Bowen, H. Lu and Y. Liu, *Appl. Catal., B*, 2023, **338**, 123007.
76 A. Majumdar, P. Dutta, A. Sikdar, H. Lee, D. Ghosh, S. N. Jha, S. Tripathi, Y. Oh and U. N. Maiti, *Small*, 2022, **18**, 2200622.
77 S. Ibraheem, G. Yasin, A. Kumar, M. A. Mushtaq, S. Ibrahim, R. Iqbal, M. Tabish, S. Ali and A. Saad, *Appl. Catal., B*, 2022, **304**, 120987.
78 R. Balaji, T. T. Nguyen, K. Harish, N. H. Kim and J. H. Lee, *J. Mater. Chem. A*, 2022, **10**, 3782–3792.
79 M. H. Han, Y.-J. Ko, S. Y. Lee, C. Lim, W. H. Lee, M. W. Pin, J. H. Koh, J. Kim, W. Kim, B. K. Min and H.-S. Oh, *J. Power Sources*, 2022, **521**, 230953.
80 C. T. Cao, S.-W. Kim, H. J. Kim, R. Purbia, S. H. Kim, D. Kim, K. J. Choi, H. Park and J. M. Baik, *Nano Energy*, 2022, **96**, 107117.
81 L. Huang, G. Wei, J. Wang, D. Li, S. Jia, S. Wu, T. Jiang, Y. Guo, Y. Liu and F. Ren, *Adv. Energy Mater.*, 2023, **13**, 2300651.
82 X. Yu, Z.-Y. Yu, X.-L. Zhang, Y.-R. Zheng, Y. Duan, Q. Gao, R. Wu, B. Sun, M.-R. Gao, G. Wang and S.-H. Yu, *J. Am. Chem. Soc.*, 2019, **141**, 7537–7543.
83 L. Zhao, M. Wen, Y. Tian, Q. Wu and Y. Fu, *J. Energy Chem.*, 2022, **74**, 203–211.
84 Y. Song, W. Xie, Y. Song, H. Li, S. Li, S. Jiang, J. Y. Lee and M. Shao, *Appl. Catal., B*, 2022, **312**, 121400.
85 L.-M. Cao, Y.-W. Hu, S.-F. Tang, A. Iljin, J.-W. Wang, Z.-M. Zhang and T.-B. Lu, *Advanced Science*, 2018, **5**, 1800949.
86 L. Yu, I. K. Mishra, Y. Xie, H. Zhou, J. Sun, J. Zhou, Y. Ni, D. Luo, F. Yu, Y. Yu, S. Chen and Z. Ren, *Nano Energy*, 2018, **53**, 492–500.
87 W. Yuan, T. Jiang, X. Fang, Y. Fan, S. Qian, Y. Gao, N. Cheng, H. Xue and J. Tian, *Chem. Eng. J.*, 2022, **439**, 135743.
88 B. K. Kim, M. J. Kim and J. J. Kim, *Appl. Catal., B*, 2022, **308**, 121226.
89 R. Feng, Z. Ye, Q. Jiang, C. Li, J. Gu and F. Song, *J. Power Sources*, 2022, **542**, 231774.
90 Y. Li, Y. Wu, H. Hao, M. Yuan, Z. Lv, L. Xu and B. Wei, *Appl. Catal., B*, 2022, **305**, 121033.
91 S. Li, L. Wang, H. Su, A. N. Hong, Y. Wang, H. Yang, L. Ge, W. Song, J. Liu, T. Ma, X. Bu and P. Feng, *Adv. Funct. Mater.*, 2022, **32**, 2200733.
92 X. Zhang, G. Ma, L. Shui, G. Zhou and X. Wang, *J. Energy Chem.*, 2022, **72**, 88–96.
93 R. Liu, X.-R. Shi, Y. Wen, X. Shao, C. Su, J. Hu and S. Xu, *J. Energy Chem.*, 2022, **74**, 149–158.
94 M.-I. Jamesh, *Lubricants*, 2022, **10**, 255.
95 H. Xiang, W. Chen, T. Li, J. Huang, G. Chen, T. Gong and K. Ken Ostrikov, *Chem. Eng. J.*, 2022, **446**, 137419.
96 S. Singh, D. C. Nguyen, N. H. Kim and J. H. Lee, *Chem. Eng. J.*, 2022, **442**, 136120.
97 H. Chu, P. Feng, B. Jin, G. Ye, S. Cui, M. Zheng, G.-X. Zhang and M. Yang, *Chem. Eng. J.*, 2022, **433**, 133523.
98 E. Vijayakumar, S. Ramakrishnan, C. Sathiskumar, D. J. Yoo, J. Balamurugan, H. S. Noh, D. Kwon, Y. H. Kim and H. Lee, *Chem. Eng. J.*, 2022, **428**, 131115.
99 H. Liu, S. Yang, J. Ma, M. Dou and F. Wang, *Nano Energy*, 2022, **98**, 107315.
100 J. Zhu, E. Jiang, X. Wang, Z. Pan, X. Xu, S. Ma, P. Kang Shen, L. Pan, M. Eguchi, A. K. Nanjundan, J. Shapter and Y. Yamauchi, *Chem. Eng. J.*, 2022, **427**, 130946.
101 X. Ding, J. Yu, W. Huang, D. Chen, W. Lin and Z. Xie, *Chem. Eng. J.*, 2023, **451**, 138550.

102 Q. Peng, Q. He, Y. Hu, T. T. Isimjan, R. Hou and X. Yang, *J. Energy Chem.*, 2022, **65**, 574–582.
103 M. Chen, H. Li, C. Wu, Y. Liang, J. Qi, J. Li, E. Shangguan, W. Zhang and R. Cao, *Adv. Funct. Mater.*, 2022, **32**, 2206407.
104 J. Cheng, B. Shen, Y. Song, J. Liu, Q. Ye, M. Mao and Y. Cheng, *Chem. Eng. J.*, 2022, **428**, 131130.
105 J. Zhao, Y. Zhang, H. Guo, H. Zhang, J. Ren and R. Song, *Small*, 2022, **18**, 2200832.
106 J. Song, D. Yu, X. Wu, D. Xie, Y. Sun, P. Vishniakov, F. Hu, L. Li, C. Li, M. Yu. Maximov, K. M. El-Khatib and S. Peng, *Chem. Eng. J.*, 2022, **437**, 135281.
107 L. Zhu, C. Li, H. Li, H. Li, Z. Wu, Y. Huang, X. Zhu and Y. Sun, *J. Mater. Chem. A*, 2022, **10**, 15520–15527.
108 C. Pi, X. Li, X. Zhang, H. Song, Y. Zheng, B. Gao, A. Kızılaslan, P. K. Chu and K. Huo, *Small*, 2022, **18**, 2201137.
109 P. Zhai, C. Wang, Y. Zhao, Y. Zhang, J. Gao, L. Sun and J. Hou, *Nat. Commun.*, 2023, **14**, 1873.
110 S.-P. Zeng, H. Shi, T.-Y. Dai, Y. Liu, Z. Wen, G.-F. Han, T.-H. Wang, W. Zhang, X.-Y. Lang, W.-T. Zheng and Q. Jiang, *Nat. Commun.*, 2023, **14**, 1811.
111 Y. Zhu, J. Zhang, Q. Qian, Y. Li, Z. Li, Y. Liu, C. Xiao, G. Zhang and Y. Xie, *Angew. Chem., Int. Ed.*, 2022, **61**, e202113082.
112 Q. Hu, Z. Wang, X. Huang, Y. Qin, H. Yang, X. Ren, Q. Zhang, J. Liu, M. Shao and C. He, *Appl. Catal., B*, 2021, **286**, 119920.
113 Y. Xin, F. Wang, L. Chen, Y. Li and K. Shen, *Green Chem.*, 2022, **24**, 6544–6555.
114 Z. Lei, X. Jin, J. Li, Y. Liu, J. Liu, S. Jiao and R. Cao, *J. Energy Chem.*, 2022, **65**, 505–513.
115 R. Ding, Y. Chen, X. Li, Z. Rui, K. Hua, Y. Wu, X. Duan, X. Wang, J. Li and J. Liu, *Small*, 2022, **18**, 2105335.
116 W. Liu, X. Wang, J. Qu, X. Liu, Z. Zhang, Y. Guo, H. Yin and D. Wang, *Appl. Catal., B*, 2022, **307**, 121201.
117 Y. Xu, J. Yang, T. Liao, R. Ge, Y. Liu, J. Zhang, Y. Li, M. Zhu, S. Li and W. Li, *Chem. Eng. J.*, 2022, **431**, 134126.
118 S. Yuan, M. Xia, Z. Liu, K. Wang, L. Xiang, G. Huang, J. Zhang and N. Li, *Chem. Eng. J.*, 2022, **430**, 132697.
119 J. Li, R. Ge, P. Lan, J. Yang, J. Feng, Y. Li, S. Li, B. Liu and W. Li, *J. Mater. Chem. A*, 2022, **10**, 10493–10502.
120 T. Gong, J. Zhang, Y. Liu, L. Hou, J. Deng and C. Yuan, *Chem. Eng. J.*, 2023, **451**, 139025.
121 P. Sun, Y. Zhou, H. Li, H. Zhang, L. Feng, Q. Cao, S. Liu, T. Wågberg and G. Hu, *Appl. Catal., B*, 2022, **310**, 121354.
122 X. Liu, P. Zou, L. Song, B. Zang, B. Yao, W. Xu, F. Li, J. Schroers, J. Huo and J.-Q. Wang, *ACS Catal.*, 2022, **12**, 3789–3796.
123 H. Park, J. W. Bae, T. H. Lee, I. J. Park, C. Kim, M. G. Lee, S. A. Lee, J. W. Yang, M.-J. Choi, S. H. Hong, S. Y. Kim, S. H. Ahn, J. Y. Kim, H. S. Kim and H. W. Jang, *Small*, 2022, **18**, 2105611.
124 S. Wang, W. Huo, F. Fang, Z. Xie, J. K. Shang and J. Jiang, *Chem. Eng. J.*, 2022, **429**, 132410.
125 X. Han, Q. Chen, Q. Chen, Q. Wu, Z. Xu, T. Zheng, W. Li, D. Cui, Z. Duan, J. Zhang, J. Li, H. Li, Z. Wang, J. Wang and Z. Xia, *J. Mater. Chem. A*, 2022, **10**, 11110–11120.
126 H. Liao, G. Ni, P. Tan, Y. Liu, K. Chen, G. Wang, M. Liu and J. Pan, *Appl. Catal., B*, 2022, **317**, 121713.
127 B. Zhang, Z. Wu, W. Shao, Y. Gao, W. Wang, T. Ma, L. Ma, S. Li, C. Cheng and C. Zhao, *Angew. Chem., Int. Ed.*, 2022, **61**, e202115331.
128 W. Shao, M. Xiao, C. Yang, M. Cheng, S. Cao, C. He, M. Zhou, T. Ma, C. Cheng and S. Li, *Small*, 2022, **18**, 2105763.
129 M. Lu, S. Kong, S. Yan, P. Zhou, T. Yu and Z. Zou, *J. Mater. Chem. A*, 2022, **10**, 12391–12399.
130 Y. Li, X. Zhai, C. Fan, X. Chen, Y. Liu, J. Yang, L. Chen, G. Ge and J. Zhang, *J. Mater. Chem. A*, 2022, **10**, 11774–11783.
131 M. Li, S. Wang, X. Wang, X. Tian, X. Wu, Y. Zhou, G. Hu and L. Feng, *Chem. Eng. J.*, 2022, **442**, 136165.
132 W. J. Chang, E. S. Sim, J. Kwon, S. Jang, D. Y. Jeong, T. Song, N. Oh, H. W. Jang, Y.-C. Chung and W. I. Park, *Chem. Eng. J.*, 2022, **434**, 134668.